

---

# Combining experimental volcanology, petrology and geophysical monitoring techniques: A case study on Mt. Yasur

Simon Bastian Kremers

---



München 2012



---

# **Combining experimental volcanology, petrology and geophysical monitoring techniques: A case study on Mt. Yasur**

**Simon Bastian Kremers**

---

Dissertation  
an der Fakultät für Geowissenschaften  
der Ludwig-Maximilians-Universität  
München

vorgelegt von  
Simon Bastian Kremers  
aus Tübingen

München, den 30.03.2012

Erstgutachter: Prof. Heiner Igel

Zweitgutachter: Prof. Donald B. Dingwell

Tag der mündlichen Prüfung: 19.07.2012

May not subterraneous fire be considered as the great plough which Nature makes use of to turn up the bowels of the earth?

*Sir William Hamilton*  
*Observations on Mount Vesuvius,*  
*Mount Etna, and other Volcanoes*  
*(1774)*



## Summary

In general, an understanding of the complex processes acting before and during volcanic eruptions is approached from various different sides, e.g. laboratory experiments on fragmentation and/or bubble burst eruption mechanisms, petrological analysis of the eruptive products and various geophysical monitoring and source localization techniques. Each of these techniques can deliver valuable insights by adding pieces of information about the physical processes that drive the volcanic activity. However, often studies are focussing on a single aspect of the process, without setting the results in a more general context. Often, this strategy is absolutely valid, when the focus is laid on a single piece in the complex chain of processes taking place in volcanic eruptions. This must fail when the results aim to suggest a valid model for the combined observations at volcanoes using the above described techniques. The resulting models of volcanic source mechanisms and eruptive features can therefore lead to biased assumptions. This study aims to close this gap between laboratory experiments, petro-chemical analysis and modern geophysical monitoring and source localization techniques in a case study of Mt. Yasur (Vanuatu) volcano.

The presented laboratory experiments on explosive volcanic eruptions upon rapid decompression show that decompression rate is the defining parameter in the experiments and that a scaling to large-scale processes is valid. Furthermore, a model is presented that correlates measured particle velocities to decompression rate and initial gas-overpressure. This model is used to estimate source volumes and overpressures at Volcán de Colima (Mexico) and Mt. Yasur (Vanuatu).

A petrographically and geochemically characterization of Mt. Yasurs eruptive products suggests a shallow magma-mingling process at both of Mt. Yasurs active craters, perhaps due to rejuvenation of material slumped from the crater walls into an open conduit system. A study on the time-reversal imaging technique and its ability to detect the details of finite rupture (or time-variant) processes shows that the limitations of TR imaging start where the source stops being point-localised with respect to the used wavelength. Inversion of the source mechanisms of Strombolian explosions at Mt. Yasur are performed using a multi-parameter dataset consisting of seismic, acoustic and Doppler-radar data. Time-reversal imaging and moment tensor inversion are used to invert the source location of the seismic long-period ( $f < 1Hz$ ) signals, which is supposed to reflect fluid movement at depth. The source is located in the north-east of the crater region in a depth of several hundred meters. Furthermore, the source volume of the radiated infrasound signals is

estimated from fundamental resonance frequencies. The results showed that the maximum particle velocity measured with the Doppler radar correlates nicely with the estimated source volumes lengths. The inverted seismic moment does not show any correlation with the estimated slug sizes, i.e. the slug size does not map in seismic moment. This is an important information, as it states that a larger source volume does not necessarily produces a larger seismic moment.

From these combined results, a common feeder system for all active craters at Mt. Yasur is proposed. The differences in event recurrence rate at the three active craters are believed to be controlled by either the conduit geometry or variations in degassing or cooling rate. Strombolian-type eruptions at Mt. Yasur are suggested to be due to the burst of gas slugs with lengths and overpressures comparable to volcanoes showing similar eruptive patterns. The results illustrate the importance of combined studies that overcome the limitations of single disciplines. In this way, a more comprehensive view of volcanic eruptions and the associated observations is possible. Such a multi-disciplinary approach will contribute to a better understanding of volcanic processes and the associated hazards.

# Contents

<b>Preamble</b>	<b>xi</b>
<b>1 Introduction</b>	<b>1</b>
1.1 Mt. Yasur, Tanna, Vanuatu . . . . .	3
1.2 Structure of the Thesis . . . . .	5
<b>2 Decompression controlled fragmentation</b>	<b>9</b>
2.1 Abstract . . . . .	9
2.2 Introduction . . . . .	10
2.3 Sample description . . . . .	11
2.4 Fragmentation experiments . . . . .	12
2.5 Results . . . . .	15
2.6 Discussion . . . . .	19
2.7 Implications . . . . .	23
<b>3 Scaling experiments</b>	<b>25</b>
3.1 Abstract . . . . .	25
3.2 Introduction . . . . .	26
3.3 Methodology . . . . .	27
3.4 Samples . . . . .	28
3.5 Results . . . . .	30
3.6 Decompression rate . . . . .	36
3.7 Energy budget model . . . . .	38
3.8 Conclusions . . . . .	41
3.9 Appendix . . . . .	43
<b>4 Petrological analysis</b>	<b>47</b>
4.1 Abstract . . . . .	47
4.2 Introduction . . . . .	48
4.3 Strombolian activity at Yasur volcano . . . . .	49
4.4 Strombolian products . . . . .	50
4.5 Shallow magma mixing . . . . .	54

---

4.6	Conclusion . . . . .	56
4.7	Methods . . . . .	56
4.8	Appendix . . . . .	57
<b>5</b>	<b>Time Reversal</b>	<b>63</b>
5.1	Abstract . . . . .	63
5.2	Introduction . . . . .	64
5.3	Numerical method . . . . .	66
5.4	Synthetic points source simulations . . . . .	68
5.5	Synthetic finite source simulations . . . . .	71
5.6	Time-reverse imaging of the Tottori earthquake source . . . . .	76
5.7	Discussion . . . . .	79
5.8	Conclusions . . . . .	80
<b>6</b>	<b>Source localization</b>	<b>83</b>
6.1	Abstract . . . . .	83
6.2	Introduction . . . . .	84
6.3	Data . . . . .	87
6.4	Results . . . . .	98
6.5	Discussion . . . . .	114
<b>7</b>	<b>Conclusions</b>	<b>119</b>
7.1	Model for Strombolian activity at Mt. Yasur . . . . .	122
	<b>Bibliography</b>	<b>125</b>
	<b>Acknowledgements</b>	<b>145</b>

## Preamble

The contents of this thesis have been presented in scientific journals in a slightly modified form or are in the process of reviewing:

Kremers, S., Scheu, B., Cordonnier, B., Spieler, O., Dingwell, D.B. (2010): Influence of decompression rate on fragmentation processes: An experimental study. *Journal of Volcanology and Geothermal Research* **193**, p.182-188, doi: 10.1016/j.jvolgeores.2010.01.015

Kremers, S., Fichtner, A., Brietzke, G.B., Igel, H., Larmat, C., Huang, L., Käser, M. (2011): Exploring the potentials and limitations of the time-reversal imaging of finite seismic sources. *Solid Earth* **2**, p.95-105, doi: 10.5194/se-2-95-2011

Kremers, S., Hanson, J., Lavallée, Y., Hess, K.-U., Chevrel, O., Wassermann, J., Dingwell, D.B.: Shallow magma-mingling-driven Strombolian eruptions at Yasur volcano, Vanuatu. *submitted to Geophysical Research Letters* (July 2012)

Kremers, S., Barsu, S., Scheu, B., Dingwell, D.B.: Decompression rate controls on explosive volcanic eruptions. *submitted to Bulletin of Volcanology* (July 2012)

Kremers, S., Wassermann, J., Meier, K., Pelties, C., van Driel, M., Vasseur, J., Hort, M.: Inverting the Source Mechanism of Strombolian Explosions at Mt. Yasur, Vanuatu, using a Multi-Parameter Dataset. *submitted to Journal of Volcanology and Geothermal Research* (July 2012)

Parts of the experimental study on the influence of decompression rate on the fragmentation process have been performed in the context of the diploma thesis "Influence of increased shear friction on fragmentation processes: An experimental study", by S. Kremers, LMU München, 2007.



## 1

# Introduction

Volcanoes have always been a fascinating and threatening phenomenon for mankind. Even in ancient times people were aware of the fire accumulating and eventually breaking free from below their feet. While the understanding of volcanic processes was obviously small in these times, the benefits provided by the fertile volcanic soil were very well appreciated. This led to an accumulation of population in volcanic areas, thereby drastically increasing the risk of human fatalities in case of a volcanic eruption. Among the hazards to people and infrastructure in the vicinity of active volcanoes are (1) various types of pyroclastic density currents (pyroclastic flows (e.g., Montserrat, UK; [Kokelaar, 2002](#); [Sparks and Young, 2002](#)), block- and ash-flows (e.g., Mt. Merapi, Indonesia; [Schwarzkopf et al., 2005](#)), surges (e.g., Bezymianny, Russia; [Belousov, 1996](#))); (2) gas avalanches (e.g., Lake Nyos and Lake Monoun, Cameroon; [Kling et al., 2005](#)); (3) tephra fallout (e.g., Mt. St. Helens, USA; [Horwell and Baxter, 2006](#)); (4) lava flows (e.g., Mt. Etna, [Behncke and Neri, 2003](#)). However, not only people living in the direct proximity are a subject to volcanic hazard, but also those affected by secondary hazards such as tsunamis (Krakatau, Indonesia, [Begét, 2000](#); Stromboli, Italy, [Tinti et al., 2006](#)), and landslides (e.g., Tenerife, Spain; [Hürlimann et al., 1999](#)), lahars (e.g., Nevado del Ruiz, Columbia, [Voight, 1990](#); Mt. Merapi, Indonesia, [Lavigne et al., 2000](#)). Additionally, large scale eruptions can significantly decrease the global temperature and thereby cause poor harvest and dearth (e.g., Tambora 1815 "the year without summer", [Sigurdsson, 2000](#)). This illustrates the importance of a proper understanding of volcanic processes and the associated hazards.

In general, this is tackled with a plethora of approaches. Laboratory experiments of processes causing explosive eruptions by rapid decompression have been performed on analogue (e.g., [Ichihara et al., 2002](#); [Mourtada-Bonnefoi and Mader, 2004](#); [Namiki and](#)

Manga, 2005, 2006; Kameda *et al.*, 2008) and natural material (e.g., Alidibirov and Dingwell, 1996b; Spieler *et al.*, 2003, 2004; Kennedy *et al.*, 2005; Kueppers *et al.*, 2006; Scheu *et al.*, 2008; Mueller *et al.*, 2008; Alatorre-Ibargüengoitia *et al.*, 2010) at temperatures up to 850 °C. Parameters controlling explosive eruptions that can be determined in this way are fragmentation threshold (i.e., a critical pressure value that defines the resistance of a material to rapid decompression, Spieler *et al.*, 2004), fragmentation speed (i.e., the speed of the fragmentation front travelling through a material, Scheu *et al.* (e.g. 2006)) and gas permeability (e.g., Mueller *et al.*, 2005). Other experiments are focussing on the ascent and burst of gas slugs in the conduit (e.g., Vergnolle and Jaupart, 1990; James *et al.*, 2004, 2006). Amongst others, these studies enhanced our view on the source dynamics of Strombolian-type eruptions and the resulting acoustic signals generated upon burst at the free surface. All laboratory studies share the advantage that the experimental conditions are generally well defined and that experiments are repeatable.

Information on the explosive dynamics can not only be determined by controlled experiments, but also through the petrological analysis of the eruptive products (e.g., Dingwell *et al.*, 1996; Dingwell, 1998; Giordano *et al.*, 2004; Llewellyn and Manga, 2005; Lautze and Houghton, 2006; Lavallée *et al.*, 2007). The analyzed samples of Strombolian eruptions often show strongly heterogeneous patterns. Lautze and Houghton (2005) suggested in a study on Stromboli volcano (Italy) a physical magma mingling in the shallow conduit (300 m below the surface), based on thin section, bubble size distribution and the chemical analyses. Contrastingly, Schipper *et al.* (2011) in a recent microanalytical study proposed the idea of incipient melt segregation due to filter-pressing driven by fluidization of interstitial melt taking place at shallow levels.

Furthermore, the various geophysical parameters that are associated with volcanic activity allow insights into volcanic source mechanisms. This includes the interpretation and inversion of recorded seismic (e.g., Neuberg *et al.*, 1994; Chouet, 1996; Wassermann, 1997; Ripepe and Gordeev, 1999; Chouet *et al.*, 2003; Aster *et al.*, 2009), acoustic (e.g., Ripepe *et al.*, 1996; Harris and Ripepe, 2007; Matoza *et al.*, 2009) and other geophysical data sets (e.g., microgravity and GPS, Jentzsch *et al.*, 2001; thermal satellite images, Dehn *et al.*, 2002; infrared imagery, Harris *et al.*, 2005; Doppler radar, Gerst *et al.*, 2008). Seismic signals at volcanoes often show highly emergent onsets due to the complex nature of the propagation medium and, in most cases, also complex topography. Conventional approaches that are based on the determination of arrival times can not be applied for the location of these signals. To date, amongst others the following techniques have been used to localize the source of seismic events: (1) beam-forming on diffraction hyperboloids (Wassermann, 1997); (2) a waveform semblance method (Kawakatsu *et al.*, 2000); (3) moment tensor inversion (e.g., Chouet *et al.*, 2003; O'Brien and Bean, 2008; Bean *et al.*, 2008); (4) time reversal (O'Brien *et al.*, 2011). Of these, moment tensor inversion is the most common technique to infer source mechanism and location of VLP ( $f < 0.1$  Hz, Chouet *et al.*, 2003) and LP ( $f < 2$  Hz, Neuberg *et al.*, 1994) events at active volcanoes. These seismic signals are believed to be generated by fluid mass transport (Chouet, 1994; Ripepe and

Gordeev, 1999; Konstantinou, 2002; O'Brien and Bean, 2008). Alternatively, Aster *et al.* (2003) demonstrated the excitation of a resonator as source of VLP events at Mt. Erebus (Antarctica).

Each of these techniques can deliver valuable insights by adding pieces of information about the physical processes that drive the activity (McNutt *et al.*, 2000; Harris and Ripepe, 2007). However, individual studies are often focussing on a single aspect only, without putting the results in a more general context. This is absolutely valid, if the focus is laid on a single piece in the complex chain of processes taking place in volcanic eruptions. This must fail when the results aim to suggest a valid model for the combined observations at volcanoes using the above described techniques. The resulting models of volcanic source mechanisms and eruptive features can therefore lead to biased assumptions and/or interpretations. This study aims to enhance the link between laboratory experiments, petrological analyses and modern geophysical monitoring (and source localization) techniques in a case study of Mt. Yasur volcano (Vanuatu).

## 1.1 Mt. Yasur, Tanna, Vanuatu

---

The complex volcanic history of Tanna island (Fig. 1.1) can be traced back as far as the late Pliocene undergoing a series of major volcanic episodes (Carney and Macfarlane, 1979; Chen *et al.*, 1995). The most recent episode formed the Siwi Group in the easternmost part of the island (Fig. 1.2) which is characterized by deposits that are predominantly basaltic to basaltic-andesites in composition (Robin *et al.*, 1994; Bani and Lardy, 2007). Since at least 300 years the activity in the Siwi Group is taking place at the Yasur cinder cone (Simkin *et al.*, 1981), which commonly shows Strombolian to Vulcanian activity (Carney and Macfarlane, 1979; Oppenheimer *et al.*, 2006; Bani and Lardy, 2007). Mt. Yasur rises 361 m above sea level having three small active craters (denoted as A, B and C from south to north, Fig. 1.3) that are excavated within a larger 400-m-diameter crater (Oppenheimer *et al.*, 2006). Despite the very persistent eruptive activity and the extremely easy access to the crater region, it has only recently attracted increased attention by scientists from various fields (e.g., Oppenheimer *et al.*, 2006; Pichon *et al.*, 2006; Métrich *et al.*, 2011; Perrier *et al.*, 2011; Bani *et al.*, 2011).

At the time of a geophysical monitoring and sample collection field campaign in August-September 2008, all three craters showed very different styles of activity. Crater A, the most active vent, had an eruption recurrence periodicity of less than one minute. Crater B showed very irregular ash venting, with variable periodicity ranging between minutes and days, while crater C produced the strongest eruptions on a longer recurrence timescale of approximately ten minutes. To record a large variety of geophysical parameters we installed four seismic arrays at site, each consisting of one broadband seismometer and two to four short period sensors. Additionally, we deployed four short period infrasonic arrays and one broadband infrasound receiver to record the acoustic pressure. The velocity of ejecta exiting

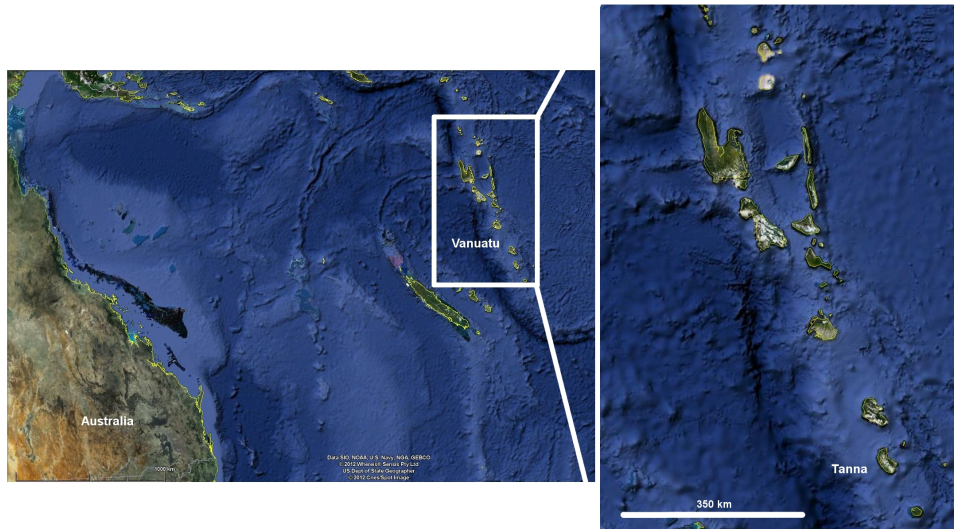


Figure 1.1: The location of the Vanuatu island chain about 1000 km north-east of Australia. The close-up shows Tanna island in the south. Figure courtesy GoogleEarth.

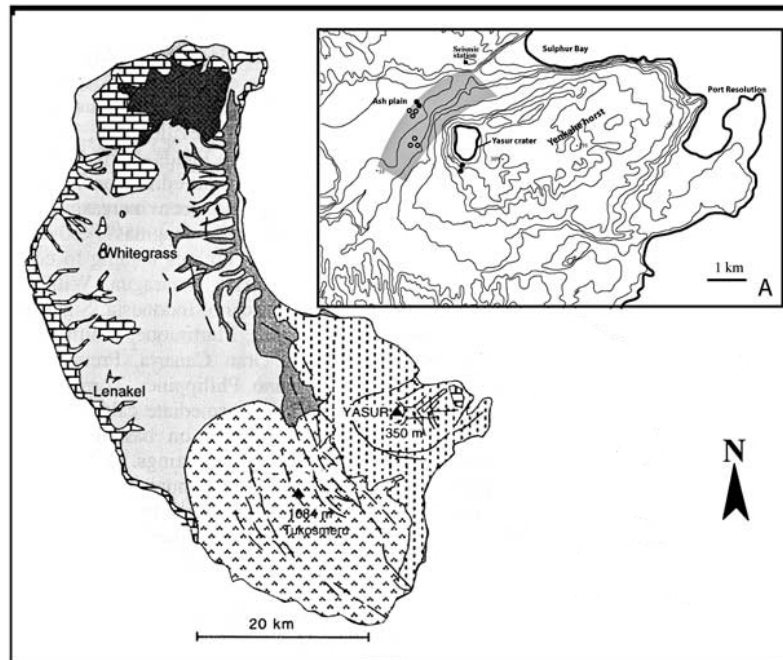


Figure 1.2: Geological map of Tanna Island modified after [Bani and Lardy \(2007\)](#). The zoom in the upper right shows the Siwi Group with the Mt. Yasur crater area.

crater A and the corresponding temperatures were measured using two Doppler radars and an infrared camera (Meier *et al.*, 2009). Additionally, the erupted products of crater A and C were sampled for a complete petrological characterization in the laboratory.

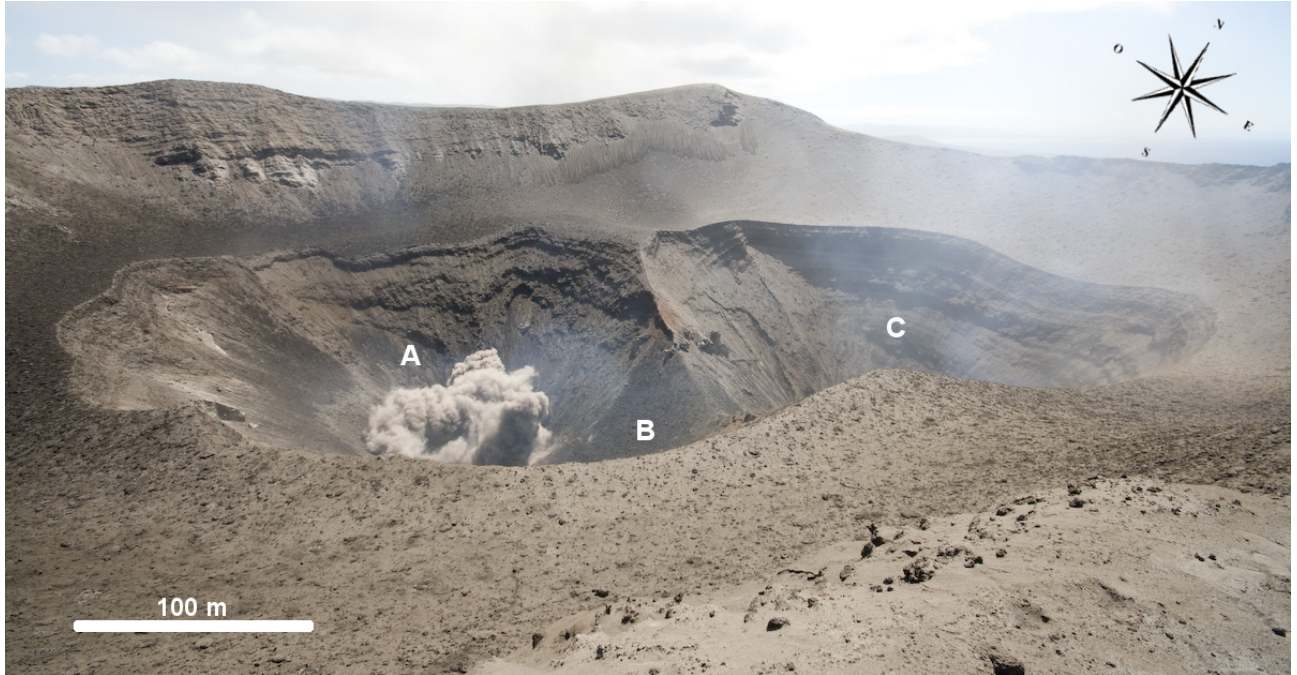


Figure 1.3: The Mt. Yasur crater area. 'A', 'B' and 'C' denote the three active craters.

## 1.2 Structure of the Thesis

---

**Chapter 1** gives an introduction in active volcanoes and the techniques applied to study the various parameters that control explosive eruptions and associated primary and secondary hazards. Furthermore, an introduction on Mt. Yasur, Vanuatu is given, followed by this presentation of the structure of the thesis.

**Chapter 2** and **Chapter 3** present the results of laboratory studies on explosive volcanic eruptions by rapid decompression. In the first chapter, the focus is laid on the study and validation of previously determined parameters such as fragmentation threshold, fragmentation speed and energy density. Furthermore, a 2D fragmentation mechanism is presented based on the observation of post-fragmentation fracture patterns. In the second chapter, the influence of decompression rate on the fragmentation process is quantified

and the link between the fragmentation mechanism and particle ejection speed is verified. Additionally, an energy budget model is introduced that provides a link between particle speed, applied overpressure and decompression rate. In a case study this model is applied to Volcán de Colima and Mt. Yasur. The two chapters present the studies of [Kremers \*et al.\* \(2010\)](#) and [Kremers \*et al.\* \(2012a\)](#) in a slightly modified form.

**Chapter 4** presents the results of a complete rheological investigation of the eruptive products of Mt. Yasur. The results of bubble size distribution, microprobe and differential scanning calorimetry suggest a shallow mingling of magmas with contrasting oxidation states. The observed textures in thin sections are believed to be partly driven by rejuvenation of material slumped from the crater walls into an open conduit system. This chapter presents the study of [Kremers \*et al.\* \(2012b\)](#) in a slightly modified form.

**Chapter 5** presents the first part on the geophysical side of the thesis. Time reversal is a recently widely used technique for source localization, however so far only for effective point sources. In an attempt to extend this technique to the study of finite rupture processes a series of synthetic and real-data experiments is presented. This chapter presents the study of [Kremers \*et al.\* \(2011\)](#) in a slightly modified form.

**Chapter 6** presents the second geophysical part including a description of a field campaign carried out 2008 at Mt. Yasur. A combination between seismic and Doppler radar data is used to correlate the size of gas slugs with the velocity of the erupted particles. Furthermore, time reversal and moment tensor inversion are used to invert for source location and mechanism. This chapter presents the study of [Kremers \*et al.\* \(2012c\)](#) in a slightly modified form.

**Chapter 7** presents the overall conclusions and summarizes the thesis.

## Motivation for Following Chapters

Recently it became clear that magmatic fragmentation of the multi-phase flow composed of melt, crystals and bubbles in volcanic conduits provides one of the key scenarios causing explosive volcanic eruptions (e.g., Mader, 1998; Alidibirov and Dingwell, 1996b; Cashman *et al.*, 2000). Various laboratory studies have studied the fragmentation process using analogue (e.g., Phillips *et al.*, 1995; Ichihara *et al.*, 2002; Mourtada-Bonnefoi and Mader, 2004) and natural materials (e.g., Alidibirov and Dingwell, 1996a; Spieler, 2004; Taddeucci *et al.*, 2004; Kueppers *et al.*, 2006; Kennedy *et al.*, 2005; Koyaguchi *et al.*, 2008; Scheu *et al.*, 2008). However, all of them share the disadvantage of working on relatively small sample sizes (up to 25 mm in diameter) that are obviously several orders of magnitude smaller compared to natural volcanic processes. Additionally, all of them represent perfect (laboratory) conditions that neglect friction, bottle-necks in the conduit shape and the influence of varying decompression rates on the fragmentation process. Chapter 2 "Influence of decompression rate on fragmentation processes: An experimental study" (after Kremers *et al.*, 2010), deals with the influence of sample/conduit sizes on the fragmentation process, compares the results to various recent studies and discusses the influence of varying decompression rates. Following this, chapter 3 (after Kremers *et al.*, 2012a) quantifies the the role of changing decompression rates, shows experimental and numerical results for particle velocities and provides an energy budget model that allows for a correlation of decompression rate, particle speed and initial overpressure.



## 2

## Decompression controlled fragmentation

## Influence of decompression rate on fragmentation processes: An experimental study

*S. Kremers<sup>1</sup>, B. Scheu<sup>1</sup>, B. Cordonnier<sup>1,2</sup>, O. Spieler<sup>1</sup>, D.B. Dingwell<sup>1</sup>*

<sup>1</sup> Department of Earth and Environmental Sciences, Ludwig-Maximilians-University, Theresienstr. 41/III, 80333 Munich, Germany

<sup>2</sup> now at ETH Zurich, Zurich, Switzerland

published 2010 in *Journal of Volcanology and Geothermal Research*:  
doi:10.1016/j.jvolgeores.2010.01.015

## 2.1 Abstract

---

A key for an effective early warning (or even a forecasting) system for volcanic eruptions, lies in the understanding of volcanic processes and the correct interpretation of monitoring data. Here, we investigate the processes occurring in the upper conduit, at the phase transition between melt and the surrounding rock, characterizing the fragmentation threshold and speed. Fragmentation experiments using a shock tube were performed, to address the following questions: (1) how does sample/conduit size affect fragmentation processes? (2) what is

the impact of different decompression rates and differing stress distributions in the sample on fragmentation threshold and speed? The observed fragmentation behaviour is analyzed in terms of energy density and compared with recent related studies. A 2D fragmentation mechanism is presented, based on the arrangement of cracks in fragmented samples. A numerical model for the estimation of the first principle stress distribution before the magma failure is provided.

## 2.2 Introduction

---

Recently, it became clear that a vital component enhancing the understanding of volcanic processes is laboratory experiments (Alidibirov and Dingwell, 1996a,b; Spieler *et al.*, 2004). Not only are laboratory experiments of fundamental importance in the validation of numerical models, but also to supply these models with realistic physical and chemical parameters (e.g. Melnik, 2000). Additionally, they can be used as a tool to explore novel phenomena, to provide systematic observation of processes, to determine the value of key parameters and to test hypotheses and theoretical models (Mader *et al.*, 2004). To date, brittle fragmentation experiments have been performed using both (1) analogue (Phillips *et al.*, 1995; Ichihara *et al.*, 2002; Mourtada-Bonnefoi and Mader, 2004) and (2) natural (Alidibirov and Dingwell, 1996a; Spieler *et al.*, 2004; Taddeucci *et al.*, 2004; Kueppers *et al.*, 2006; Kennedy *et al.*, 2005; Scheu *et al.*, 2008) materials. Fragmentation experiments using natural materials were first performed by Alidibirov and Dingwell (1996b,a). More recently, variables such as sample size, sample chemistry, porosity and experimental setup have been investigated in more detail (Spieler *et al.*, 2003, 2004; Scheu *et al.*, 2008). Previous fragmentation experiments on natural material have been restricted to samples of a diameter of 17 mm (Alidibirov and Dingwell, 1996a; Spieler, 2001) or, more recently, 25 mm (Kueppers *et al.*, 2006; Scheu *et al.*, 2006). To our knowledge all fragmentation experiments conducted on natural materials so far resemble quasi 1D fragmentation processes. However, in nature, conduit sizes can range from meters to tens of meters in diameter. Furthermore, the diameter of the conduit can also vary over its length (see Fig. 2.1). From this, the following important questions arise: (1) how does sample size influence the fragmentation process (i.e. energy density, fragmentation threshold and speed)?; (2) is the distribution of stress within the sample influenced by changes of the conduit diameter? (3) how is the fragmentation process influenced by a constriction at the top of the autoclave, resembling a bottle-neck shaped volcanic conduit in nature (Fig. 2.1)? For this purpose a new experimental setup was designed. It contains reduction rings that were mounted in the top of autoclave to achieve the desired restriction and is capable of fragmenting samples with a diameter of 60 mm, more than twice the diameter of samples used in previous experiments. Certainly, this is still far from natural dimensions, but it should permit us to identify important trends in the influence of sample and conduit size on the fragmentation process.

## 2.3 Sample description

The samples analyzed during this study were collected from Lipari (Italy), Krakatau and Kelut (Indonesia), Mount St. Helens (USA) and Santorini (Greece), as well as few samples from Bezymianny (Russia). Cylindrical samples of each rock type were drilled to a diameter of 60 mm, cut to a length of 60 mm and carefully ground flat and parallel. During sample preparation, any flow alignments observed in the sample were taken into consideration in order to accurately reproduce the original flow orientation.

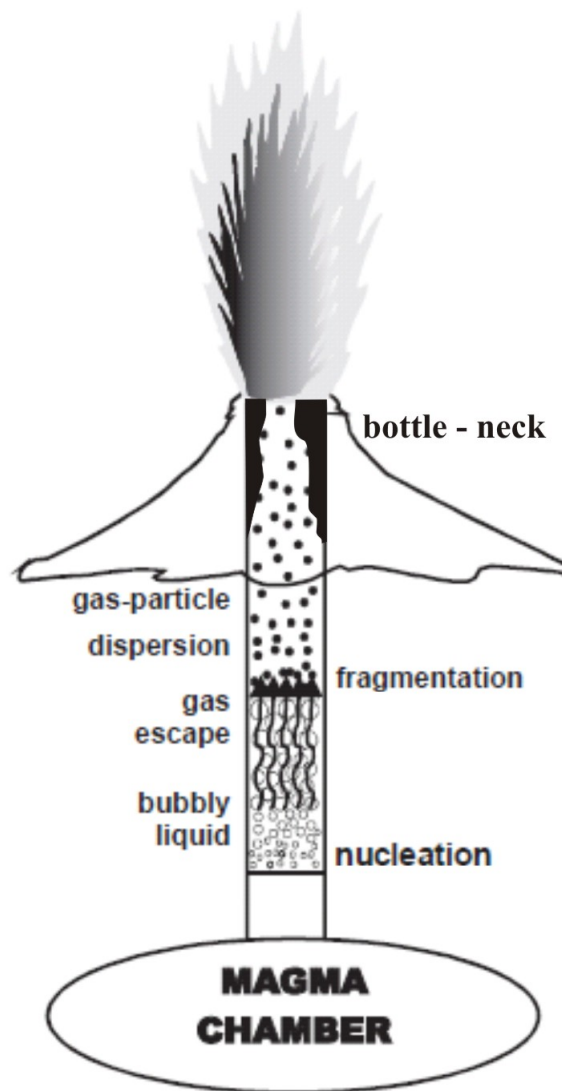


Figure 2.1: Sketch of a volcanic system showing the bottle-neck in the upper conduit part, modified after [Melnik et al. \(2005\)](#).

Density and porosity values were determined for each sample by using a helium pycnometer (Accupyc 1330, Micromeritics). Samples from Lipari, Krakatau and Kelut show a range in open porosity from 16 – 46% (LIP), 51 – 74% (KRA) and 42 – 75% (KEL), respectively. Samples from Mount St.Helens, Santorini and Bezymianni are more homogeneous and have open porosities of 40.3% (MTSH), 74.9 – 78.2% (SANT) and 65.7% (BEZ) respectively (see Fig. 2.2).

sample	density [g/cm <sup>3</sup> ]	open porosity [%]	fragm. Pressure [MPa]	energy density [J/cm <sup>3</sup> ]	fragmentation speed [m/s]	reduction ring size [mm]	correction factor*
LIP A1	2,07	24,35	9,5	2,31	23,2	30	1,153
LIP B1	2,16	40,3	4,7	1,89	11,1	30	1,103
LIP B2	2,16	41,93	6,7	2,81	13,7	30	1,122
LIP B3	2,16	41,7	6,1	2,56	40,1	45	0,699
LIP C1	2,21	32,7	6,5	2,11	25,8	45	0,700
LIP C2	2,21	32,7	8,6	2,82	23,2	30	1,147
LIP D	1,73	46,05	6,5	2,98	21,8	30	1,190
LIP E	2,33	40,15	5,4	2,16	31,5	45	0,692
LIP F	1,83	16	9,6	1,54	30,4	45	0,732
LIP H	2,2	46,8	6	2,82	58,8	45	0,699
KRA P6-2	1,16	51,96	4,12	2,14	30,6	30	1,100
KRA P5	1,58	65,3	4,08	2,66	35	30	1,098
KRA P9	2,31	74,5	5,37	4	50,8	30	1,110
KRA P6-1	1,16	51,96	4,17	2,17	58,8	45	0,676
KRA P10	1,41	71,9	3,88	2,79	68,2	45	0,669
KRA P3	1,55	60,15	3,96	2,38	78,9	45	0,666
KEL C15-3	2,31	42,69	11,1	4,74	47,8	30	1,176
KEL R2	2,39	75,77	7,54	5,71	67,7	30	1,130
KEL C15-4	2,21	49,55	8,64	4,28	68,2	45	0,722
KEL C15-2	2,31	57,6	8,54	4,92	81,4	45	0,726
MTSH 5	2,47	40,5	9,11	3,69	18,6	30	1,152
MTSH 2	2,41	40,6	6,81	2,765	58,9	45	0,705
SANT 4	1,81	78,2	5,3	4,15	71,7	30	1,100
SANT 3	1,89	77,3	4,32	3,34	93,7	45	0,673
BEZ D2-1	2,72	65,7	6,1	4,01	103	45	0,695
BEZ D2-2	2,72	65,7	5,8	3,81	62,1	30	1,105

Figure 2.2: Measured and experimental produced data for the sample sets from Lipari (LIP), Krakatau (KRA), Kelut (KEL), Mt. St. Helens (MTSH), Santorini (SANT) and Bezymianny (BEZ). \* Correction factor determined by empirical fit.

## 2.4 Fragmentation experiments

Rapid decompression experiments using an apparatus based on the shock tube principle were performed to realistically simulate volcanic fragmentation processes (Alidibirov and Dingwell, 1996b,a; Spieler *et al.*, 2004). The apparatus, shown in Figure 2.3 consists of two main parts (1) a high-pressure autoclave and (2) a low-pressure tank. The autoclave is made of stainless

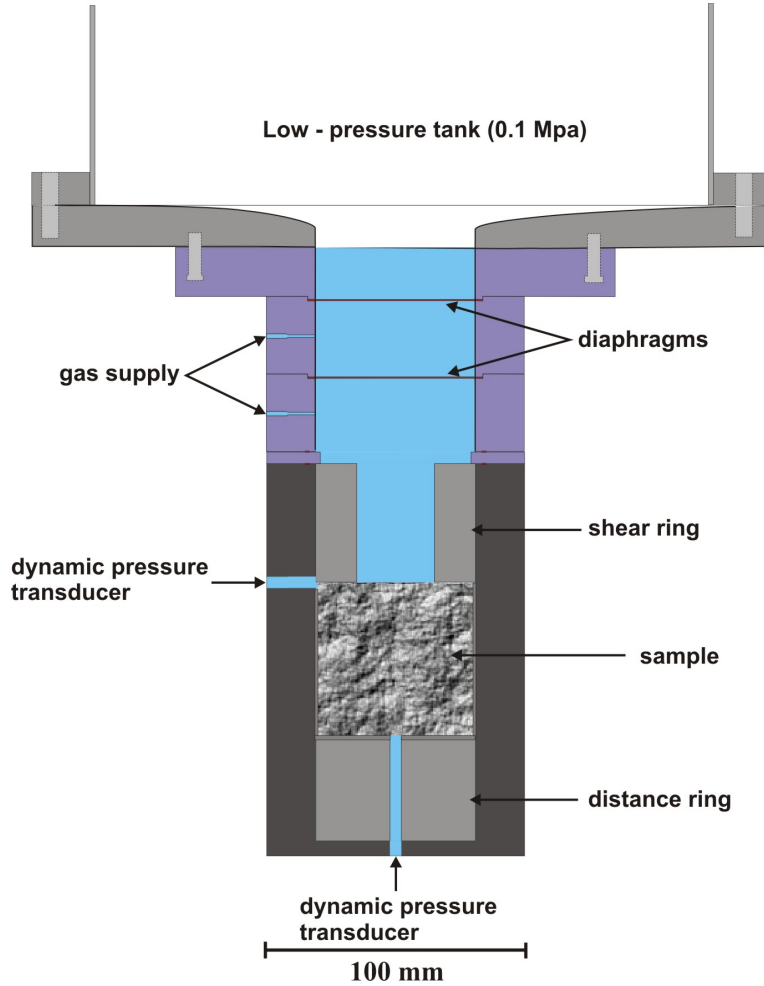


Figure 2.3: The high pressure autoclave in a schematic image in scale with a sample placed in it as used in the experiments. The two pressure transducers are used to monitor pressurization, the diaphragms separate the system from the overlying low-pressure tank.

steel and can be operated to a pressure of up to 50 MPa using argon gas and a membrane compressor. During experimentation, two pressure transducers were used to monitor the autoclave pressurization (Fig. 2.3). The low-pressure tank, a 3 m high and 0.4 m diameter steel tube at normal atmospheric conditions, is used to collect the fragmented particles. Two diaphragms were used to separate the high- from the low-pressure components of the fragmentation apparatus; to enable creation of the pressure difference ( $\Delta P$ ) between autoclave and tank (Fig. 2.3) and to define precisely the opening pressure. Samples were glued into a specially designed stainless-steel sample holder, of the same dimensions as the sample, using a mounting adhesive (Crystalbond 509). This sample holder was then mounted into the autoclave. Fragmentation of a sample was activated by failure of the upper diaphragm, causing the second diaphragm to burst open almost immediately, resulting in the rapid decompression of the high-pressure autoclave. The expulsion of gas from the autoclave creates a shock wave that travels into the low pressure tank, and a rarefaction wave that propagates down

into the autoclave. When the wave reaches the sample, a pressure gradient is generated in the sample. The steepness of the pressure gradient is defined by the applied pressure and the permeability of the sample (Mueller *et al.*, 2008). Once a certain critical pressure gradient has been reached in the sample (i.e. the fragmentation threshold), it starts to fragment. It has been observed that the predominant fragmentation mechanism is a layer-by-layer fragmentation due to vesicle bursting (Alidibirov and Dingwell, 2000; Scheu *et al.*, 2006; Fowler *et al.*, 2009). In this case, brittle failure of the upper layer will occur, if the tensile strength of the magma is overcome. Fragments are expelled and pressure gradient continues to build up from the newly created free surface. At the depth the tensile strength of the magma is overcome again, the next layer fragments, and so on. The propagation speed of this continually repeating process through the sample is denoted as the fragmentation speed. If the fragmentation threshold is not reached, fragmentation does not occur and the pressure drops slowly by gas filtration.

Three pressure transducers continuously monitored the entire pressure history during experimentation. First, a static pressure transducer fixed to the gas supply under the lower diaphragm tracks the entire pressure evolution in the autoclave. Two dynamic pressure transducers were situated above and below the sample and recorded the pressure drop following the rapid decompression of the autoclave and the fragmentation of the sample, respectively. The time delay between the pressure drop within the two transducers was measured and, together with the known distance between the pressure transducers, the speed of fragmentation through the sample was calculated.

Reduction rings (see Fig. 2.3) with two different internal diameters (30 and 45 mm) were used in the autoclave to restrain the sample. Use of reduction rings of different diameter resulted in a changes in the stress distribution and decompression rate, as the cross-sectional area of the exit flow and the volume of the compressed gas varies with reduction ring size. Due to the complicated two phase flow fluid dynamics caused by the reduction rings no calculation of decompression rates was possible. Therefore, decompression rates were measured in experiments performed with empty sample holder.

Of particular interest to this study was the influence of the reduction ring on the fragmentation threshold values (the pressure at which first full fragmentation occurs), as well as its influence on the pressure gradient and the stress distribution in the sample, fragmentation speed and energy density. The energy density is primarily dependent on the open porosity, as this constraint defines the volume of pressurized gas that can be stored in the sample. Therefore, all experiments carried out in this study were performed at or slightly above the fragmentation threshold values as defined by Spieler *et al.* (2004). Experiments were performed in a pressure range from 2 to 11 MPa.

## 2.5 Results

### 2.5.1 Experimental results

The analyzed samples cover a large range in porosity from 16 to 78% and should comprise a sufficient data set to allow general statements. The obtained data were analyzed in terms of reduction ring size and porosity values. The fragmentation speed values were calculated using the time difference in pressure drops recorded by the dynamic transducers. Fig. 2.4 shows the fragmentation speed versus the applied fragmentation pressure for the Lipari sample set. A clear dependence of fragmentation speed on the reduction ring size and thus on decompression rate can be observed. Samples comparable in fragmentation pressure result in significantly lower fragmentation speeds if they are held back using the 30 mm ring (blue symbols). To introduce the influence of porosity on the fragmentation process, the fragmentation speed was plotted against the energy density (i.e., energy available for fragmentation per unit volume) in Fig. 2.5. This plot confirms the trend observed in Fig. 2.4. In both figures samples were sorted according to porosity and reduction ring size to eliminate the influence of differing porosity and thereby differing available energy. This allows a more direct view of the influence of decompression rate on fragmentation speed. It can be clearly seen that samples comparable in porosity and applied pressure but with different reduction ring sizes show strong variations in fragmentation speed (red and blue symbols in Fig. 2.5). Even samples fragmented at lower pressures using the 45 mm reduction ring show higher fragmentation speeds than their porosity-analogues using the 30 mm reduction ring (red marks in Fig. 2.4). These plots have been generated for all sample sets and deliver comparable results.

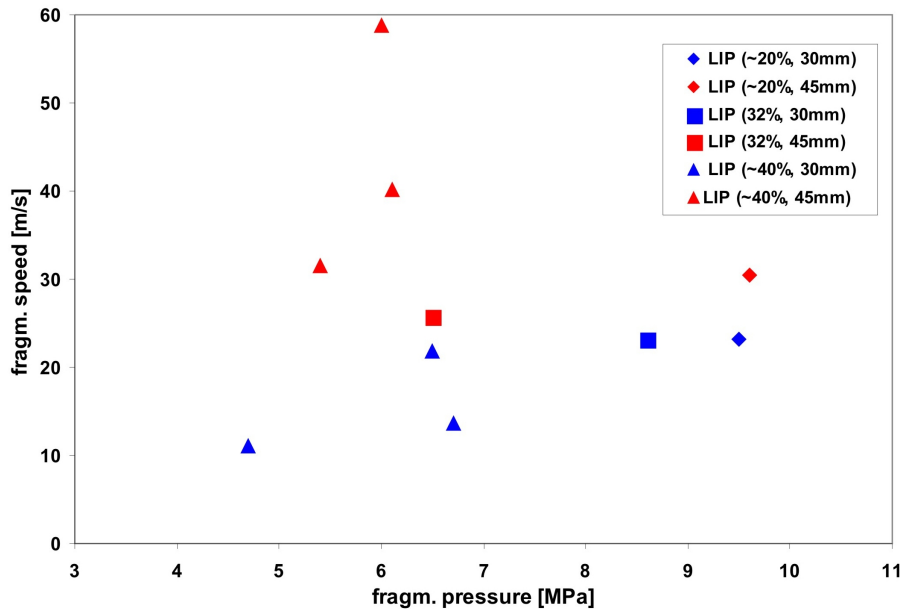


Figure 2.4: Fragmentation pressure versus fragmentation speed, ordered by porosity and reduction ring size for the Lipari sample set.

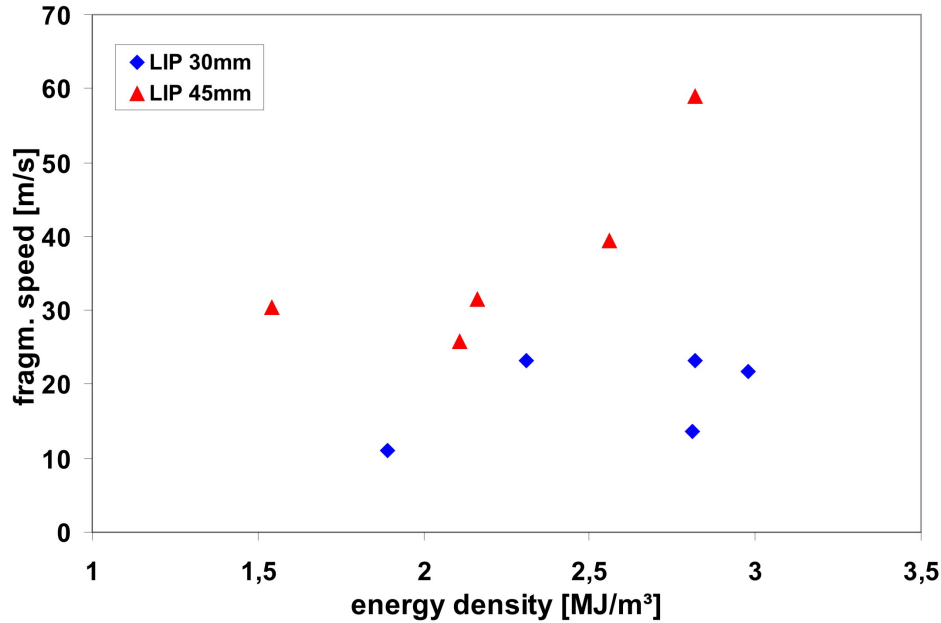


Figure 2.5: Energy density versus fragmentation speed for all analyzed samples from Lipari, separated after reduction ring size.

## 2.5.2 Fracture patterns

The used reduction rings influence the stress distribution in the sample. The compressional stress under the reduction ring is considered to be increased and orientated parallel to the reduced orifice (see Fig. 2.8). As no direct observation of the fragmentation process was possible, the sample remnants were analysed. Investigation of the expelled pyroclasts is not feasible, because of the low percentage of large particles and the additional fracturing processes caused by the reduced orifice. Thus, the focus here is on remnants stuck to the wall of the sample holder during experiments, where full ejection of all pieces did not occur. These remnants show a variety of fractures created by the fragmentation process as the unloading wave propagates through in the sample. Fig. 2.6 shows an example thereof; the sample holder with the remnants was impregnated with epoxy and then sectioned. In this way, the alignment of fractures and rupture zones can be clearly observed. A part of the sample is completely removed, whereas other remnants remain stuck to the sample holder. This may be caused by non-uniform adhesion by the glue or (more probably) the irregular opening of the diaphragm. The white lines show the typical bowl shaped fracture patterns generated by the fragmentation wave, i.e. opening cracks formed by tensile failure. The dotted red lines presumably mark shear fractures, pointing at a downward angle of about  $30-45^\circ$  (V-shaped) from the centre to the rim of the sample holder.

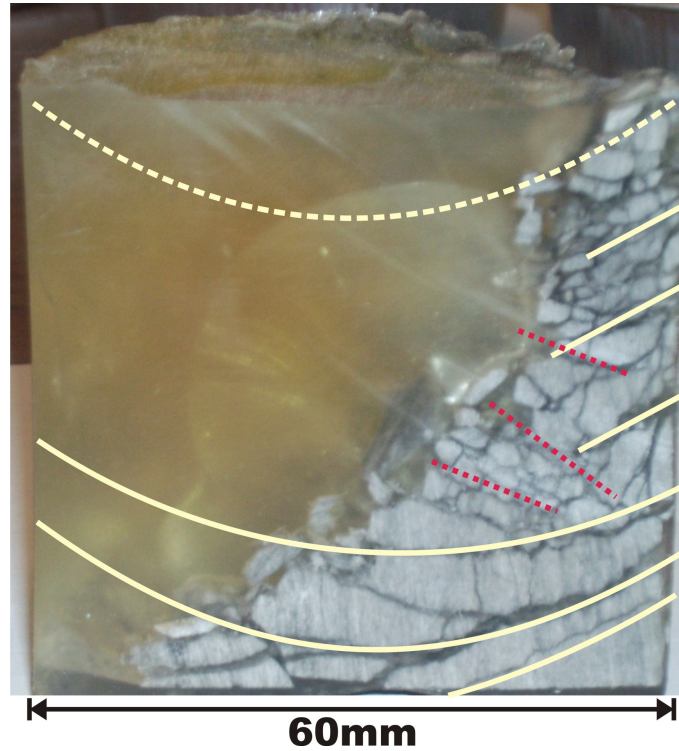


Figure 2.6: Sample LIP C2 after fragmentation, impegated with epoxy and cut open. White lines show primary fractures and the typical bowl-shaped structure caused by the fragmentation wave. The left side of the sample is completely removed. Dotted lines show presumed shear fractures.

These fractures are similar to the shear bands and fracture surfaces observed in the kinkbanded tube pumices described by [Marti \*et al.\* \(1999\)](#). Other, secondary fractures (tensile as well as shear fractures) are generated during the removal of parts of the sample. Overall the fractures resemble a complex pattern with superposition of tensile and shear failure mechanisms. However, the dominant mechanism seems to be the tensile failure forming opening cracks. It is assumed that in this type of fragmentation experiment the sample was broken internally due to the presence of reduction rings, whereas in previous experiments fragmentation is likely to be influenced by the way of sample mounting and the yield strength of the used glue.

Fig. 2.7 sketches the process believed to be occurring during a rapid decompression event with reduction ring. Starting with the mounting of the sample (a) and its slow pressurization (b), to the initiation of the rapid decompression event (c). As the unloading wave travels into the sample a pressure gradient builds up leading to the fragmentation of the sample and ejection of the particles. Due to the reduced diameter of the reduction ring compared to the sample, the unloading wave, arriving almost parallel at the sample surface, travels with a diffracted front into the sample (d).

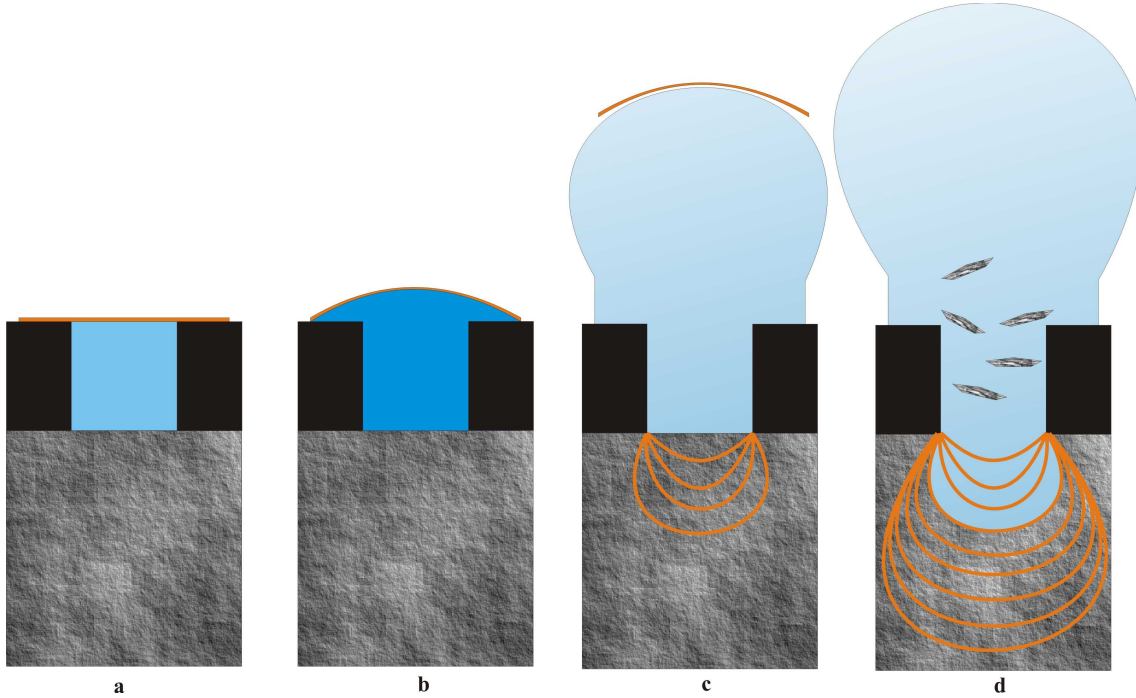


Figure 2.7: The fragmentation process as occurring in an experiments with the 30 mm reduction ring. The sample is installed into the setup, the overlying diaphragm closes the autoclave to the low-pressure tank (a). Pressurization starts, the diaphragm begins to bulge (b). After the bursting of the diaphragm, an unloading wave travels down in the autoclave and a pressure gradient is initiated in the sample (c). The sample starts to fragment as the unloading wave travels further in the sample (d).

### 2.5.3 Numerical model

In order to better estimate the stress within the sample, an axi-symmetric elastic finite element model driven by surface unloading was developed. The numerical simulation neglects the porosity and approximates the rock as an homogeneous and continuous media. This study focuses on the first principle stress. Here, the first principle stress ( $\sigma_{1,1}$ ) is normalized to the unloading stress, which offers the tensile stress distribution. As mentioned above tensile failure is believed to be prominent failure mechanism. Boundary conditions are set up to no displacements (shear and normal) and the following parameters are assumed for stress recalculation:  $E$  (Young's modulus) =  $2 \cdot 10^{11}$  Pa,  $\nu$  (poisson ratio) = 0.33 and  $\rho$  (density) =  $1.25 \cdot 10^6 \frac{g}{m^3}$ . In Fig. 2.8, the first principal stress, normalized to the unloading force, is mapped. The contour lines develop a bowl-shaped pattern. They resemble high tensile stresses at the top surface that define an aera highly prone to fragment. Out of this aera they quickly decrease to nearly 0, forcing to reach an unloading stress higher than the critical

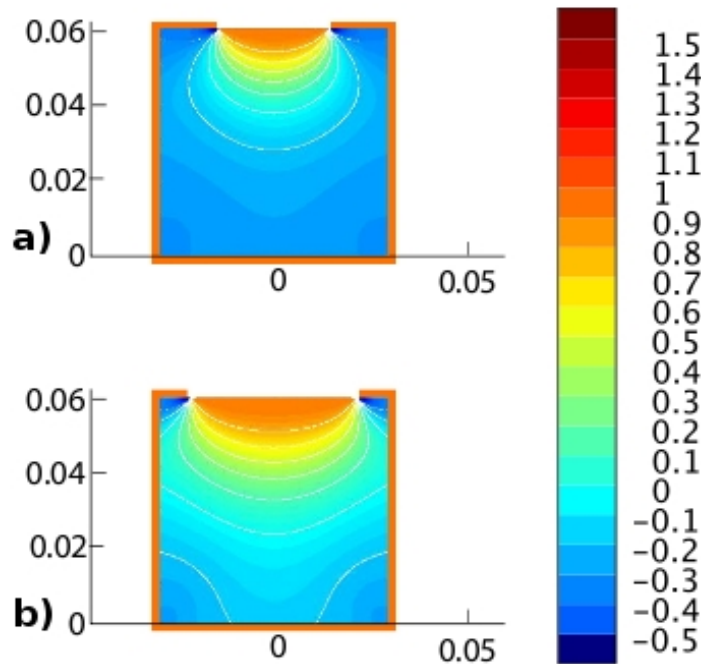


Figure 2.8: The first principle stress normalized to the unloading/decompression stress before the failure of the sample for the 2 different reduction rings: a) 30 mm; b) 45 mm.

value to fragment the full sample. This behaviour is more prominent for the 30 mm ring ( a) in Fig. 2.8), where the tensile stress shows up about half way down the sample and dropping to almost 0 at the bottom. Using the 45 mm ring ( b) in Fig. 2.8) results in higher tensile stresses over the full sample height. It implies that with this ring size the possibility of fracturing the full sample is markedly increased compared to the 30 mm ring.

The observed fracture pattern (see Fig. 2.6) is successfully validated by the model, showing that the prevailing tensile failure mechanism will produce a bowl-shaped fracture pattern for ring-size/crucible diameter below 0.5, the first principle stress distribution is bowl-like rather than layer-like.

## 2.6 Discussion

Up to now, variations in decompression rate as an influence on fragmentation processes have been tested on analogue material (Ichihara *et al.*, 2002; Namiki and Manga, 2005; Kameda *et al.*, 2005), but not taken into account in experiments on natural samples. In nature the conduit margin is a physical transition zone from the ductile to the brittle regime. Here, the acting strains cause shear stress in the melt or vice versa. In the experiments the stresses were reproduced by using reduction rings of differing size. The impact of the inserted reduction rings in the experiments could be clearly demonstrated, and it is of particular interest

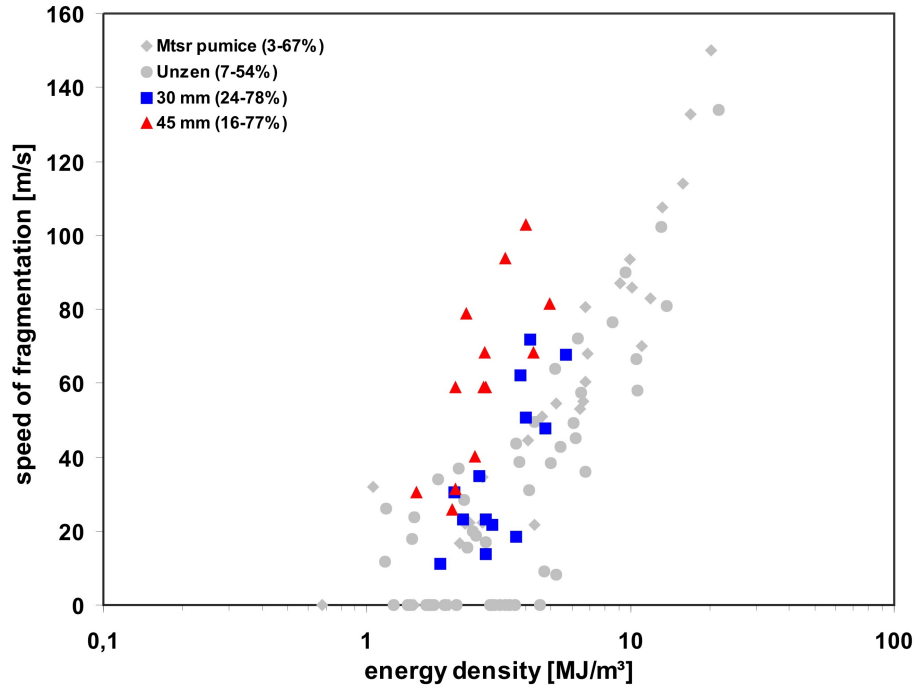


Figure 2.9: Energy density versus fragmentation speed for all the investigated experiments (squares and triangles) in comparison to the experiments performed and published by Scheu (2005) (grey marks).

to examine how these results differed from recent experimental data.

During the past few years a vast quantity of fragmentation experiments have been performed using samples of 17 mm and 25 mm in diameter (Scheu, 2005; Kennedy *et al.*, 2005; Scheu *et al.*, 2006, 2008). A comparison of these data to the one gained during this study revealed differences in energy density, fragmentation threshold and fragmentation speed (Fig. 2.9 and Fig. 2.11). The grey marks in Fig. 2.9 show the experimental data as published by Scheu (2005), whereas the colored marks represent results gained in this study. It can be observed that the data of experiments performed using the 30 mm reduction ring (blue symbols) matches the data of (Scheu, 2005) quite well, while those using the 45 mm reduction ring (red symbols) show a clear shift towards higher fragmentations speeds or lower energy densities. A possible reason for this shift is the change in decompression rate caused by the experimental setup. It has to be mentioned in this context that the older experiments could be treated as quasi 1D, allowing to calculate the decompression using the approach of Kieffer and Sturtevant (1984). Here, the reduction rings modify the setup to a 2D axisymmetric one. Unfortunately, decompression rates can now no longer be calculated using this relatively simple approach. To allow for a real comparison of the old and new experimental data a correction for the influence of the changed decompression rates due to the modified experimental setup had to be introduced. Therefore, we used the measured decompression rates of the experiments with empty sample holder for the old (25 mm) and the new (60 mm) setup (see Tab. 2.12) and fitted them empirically. From these fits we retrieve a correction

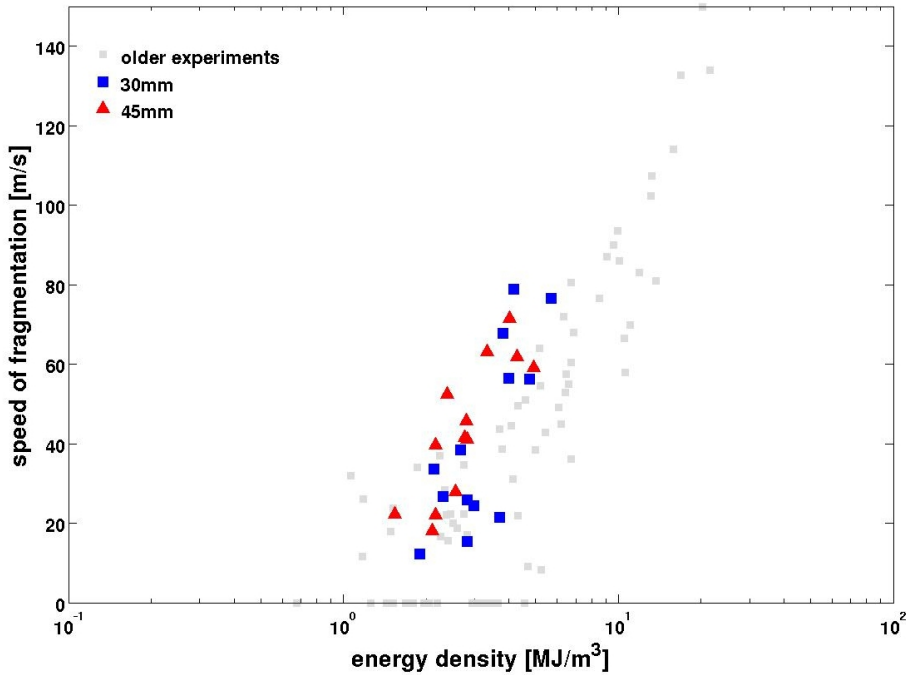


Figure 2.10: Energy density vs fragmentation speed, corrected for the influence of increased/decreased decompression rate.

factor (see Table 2.2) for each experimentally used fragmentation pressure, which allows to estimate the influence of decompression rate on fragmentation speed caused by the modified experimental setup. This is possible as the speed of fragmentation depends linearly on the decompression rate. Fig. 2.10 shows the corrected data with respect to the experiments using 25 mm in diameter samples. It is clearly observed that after the removal of the influence of increased decompression rate on fragmentation speed, the results of the reduction ring experiments are in better agreement with the older experiments. The remaining discrepancies can be explained by the decreased rock strength due to the increased sample size compared to the 25 mm samples. In that way the sample breaks easier and more energy for the propagation of the fragmentation wave is available, which results in a higher fragmentation speed. The decreased rock strength might originate from micro cracks and inhomogeneities (porous areas, large phenocrysts) and is more likely to be found in larger samples. This is a common feature in rock mechanic tests in silicic magmas (Scheu *et al.*, 2008).

In Fig. 2.11 the results of this study are included in the threshold graph of various older data. Due to the changed stress gradient in the samples caused by the reduction rings and the increased decompression rates these results might not be directly comparable. The large sample size required for these experiments precluded a sufficient number of experiments being performed in order to accurately constrain the fragmentation threshold. Here, the pressure causing full fragmentation is given instead of the actual threshold, which denotes the pressure at which the sample first starts fragmenting. An estimation for the maximum deviation in terms of applied pressure (2 MPa) is shown by the error bars. In spite of these restrictions,

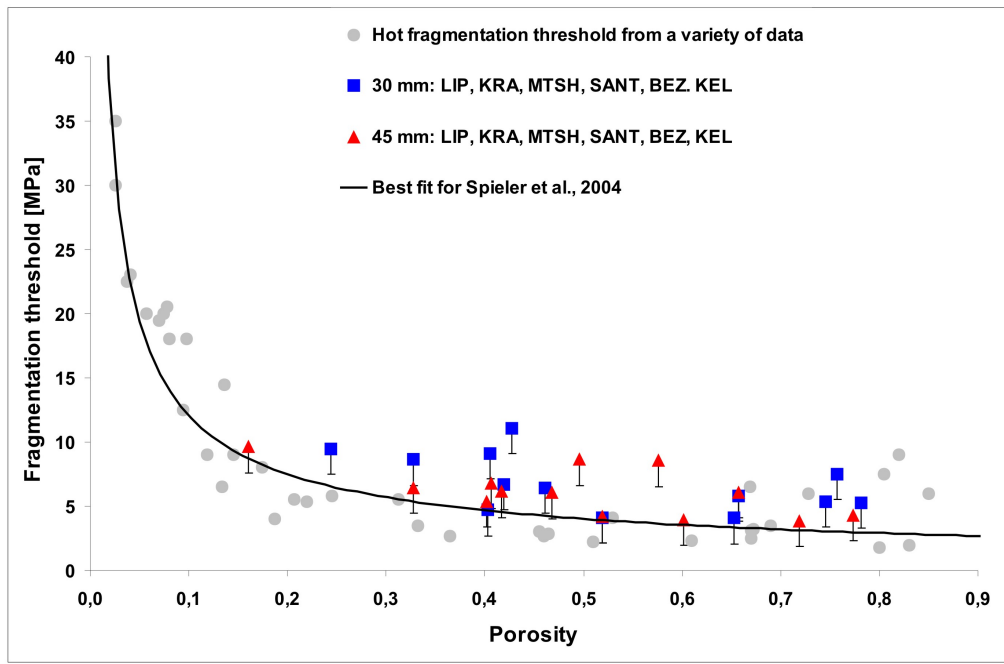


Figure 2.11: Porosity vs fragmentation threshold data as published by [Spieler et al. \(2004\)](#) in comparison to data gained in this study.

the results are in good agreement with the best-fit estimation for threshold values by [Spieler \*et al.\* \(2004\)](#), showing that the modified stress distribution has only a minor influence on the fragmentation threshold.

experiment	autoclave diameter [mm]	reduction ring size [mm]	fragm. Pressure [MPa]	measured decompression time [s]	decompression rate [Gpa/s]
E1	60,00	30	2,08	0,00213	0,977
E2	60,00	30	5,05	0,00187	2,701
E3	60,00	30	9,55	0,00188	5,080
E4	60,00	45	3,55	0,00118	3,008
E5	60,00	45	9,59	0,00116	8,267
BE1	25,00	-	10,00	0,00155	6,452
BE2	25,00	-	20,00	0,00135	14,870
BE3	25,00	-	30,00	0,00117	25,750

Figure 2.12: Measured decompression rates of experiments performed with empty autoclave for the 30 mm and 45 mm reduction ring and for samples of smaller diameter.

## 2.7 Implications

The results of this study agree with the previously observed dependence of fragmentation speed on applied pressure and energy density. As energy density is a function of porosity and applied pressure, higher energy density values thus result in higher fragmentation speeds. Here, the influence of modified stress distribution and decompression rate on the fragmentation experiments was tested by inserting reduction rings with differing diameters in the setup. The usage of these rings resulted in a shift towards lower energy densities or higher fragmentation speeds, with the 45 mm reduction ring producing the biggest shift. This shift could be mostly removed by correcting for the increased decompression rates compared to previous experiments. It has to be mentioned that the influence of changed stress distribution and decompression rate could not be measured independently, but as the shift could be mostly removed by correcting for decompression rate, the influence of the changed stress gradient is believed to be of second order.

Due to the restrictions caused by the limited amount of sample material, the increased decompression rates and the changed stress distribution in the sample, no direct comparison can be made about the influence of decompression rate on fragmentation threshold. But the data of this study strongly suggest that the threshold value decreases with increasing reduction ring size (30  $\rightarrow$  45 mm) again as a result of a higher decompression rate. Furthermore, the results are in good agreement with the best-fit estimation for threshold values by [Spieler \*et al.\* \(2004\)](#).

In this type of experiment the propagating fractures will interact less with the sample holder boundary and the glue, but fragmenting the sample itself instead. Therefore, the results of this study yield insight on the impact of this boundary effect in previous experiments. After correcting for the changed decompression rates the results of this study match those of previous studies reasonably good. This suggests that this boundary effect is not of first order significance for our fragmentation experiments. A model for the distribution of the first principle stress within the sample before its failure is shown. The model supports the theory of the rarefaction wave, creating so-called “bowl-shaped” structures. In contrast to previous experiments this model can be no longer treated in a quasi 1D fashion, as the used reduction rings produce a spherical and not a flat wavefront. Therefore, the prevailing mechanism of fragmentation is rather a bowl-by-bowl than a layer-by-layer fragmentation, a conclusion supported by the shape of the cracks in the sample.

The 2D axisymmetric model introduces another important step towards more realistic experimental conditions. The fragmentation through a reduction ring resembles a volcanic conduit with a bottle-neck shape and thereby simulates stress distributions and decompression rates in the conduit (Fig. 2.1). It could be shown that this results in higher fragmentation speeds or lower energy densities, respectively.

Overall, the results of various older studies are validated, especially in showing that threshold and fragmentation speed results lie in the same trend and are not influenced by variations in the stress distribution. Future investigations should attempt, if possible, a further increase of the sample diameter size, as well as such experiments at high temperature in order to validate the observed trends and provide further knowledge about eruptive processes associated with explosive fragmentation. This resulting refinement of models may well lead to improvements in risk and hazard assessment.

# 3

## Scaling experiments

### Decompression rate vs. fragmentation speed in volcanic explosions

*S. Kremers<sup>1</sup>, S. Barsu<sup>2</sup>, B. Scheu<sup>1</sup>, D.B. Dingwell<sup>1</sup>*

<sup>1</sup> Department of Earth and Environmental Sciences, Ludwig-Maximilians-University, Theresienstr. 41/III, 80333 Munich, Germany

<sup>2</sup> Department de Physique ENS Lyon, 46 alle d'Italie, 69364 Lyon, France

submitted to *Bulletin of Volcanology*

#### **3.1 Abstract**

---

Explosive volcanic eruptions are manifold and scale from rather small Strombolian to devastating Plinian type. Decompression of pressurized volcanic systems on very short time scales is a key scenario that causes violent explosive eruptions. During a decompression event, a multi-phase system composed of melt, bubbles and crystals in the conduit, is exposed to a rapidly evolving pressure gradient. This system is critically dependant on material properties such as vesicularity, crystallinity, chemical composition, overpressure and temperature. The rate of decompression controls if and when the structural relaxation time of the mixture is

overcome. This leads to brittle fragmentation of the material which is eventually explosively erupted.

Various laboratory studies have investigated fragmentation via rapid decompression of natural volcanic materials. These were confined to relatively small sample sizes, thereby introducing an upper limit to bubble and phenocryst sizes that show a wide range in magmatic rocks. We developed a setup to investigate the fragmentation behavior of large samples (60 mm), broadening the range of natural samples suitable for the experiments. Additionally, we are able to verify previously observed trends and evaluate major and minor influences on the fragmentation process caused by the experimental setup. In detail, the goal of this study is to (1) determine the fragmentation behavior of large samples; (2) quantify the effect of decompression rate on the fragmentation process and (3) verify the link between the fragmentation mechanism and the particle ejection velocity.

In this study, we performed experiments on samples from Lipari (Italy), Mt. Merapi (Indonesia) and Mt. Yasur (Vanuatu) that cover a large range in connected porosity, namely 18 - 78 %. All rapid decompression experiments were conducted at room temperature in a pressure range from 2 - 9 MPa. In a first series of experiments we analyzed the fragmentation threshold, in a second series we determined the fragmentation speed for each experiment. Additionally, we were able to estimate the velocity of the particles ejected after fragmentation using a high-speed camera. The results are discussed in the light of data from recent studies using smaller sample diameters. Further, we evaluate the influence of varying decompression rates on the experiments. Finally, we introduce an energy budget model that provides a link between particle speed, applied overpressure and decompression rate and apply this in a case study to Volcán de Colima and Mt. Yasur.

## 3.2 Introduction

---

Rapid decompression of pressurized volcanic systems is one of the key factors causing explosive eruptions (Alidibirov and Dingwell, 2000; Ichihara *et al.*, 2002). During eruption, the mixture of melt, crystals and bubbles comprising the magma in the conduit is exposed to high strain rates. If the strain rate approaches the structural relaxation time of the melt, brittle fragmentation will occur (Spieler *et al.*, 2004; Papale, 1999). The rate of decompression controls the strain rate and thereby determines whether an explosive event is triggered (Alidibirov and Dingwell, 1996b, 2000). Furthermore, Toramaru (2006) showed that decompression rate also correlates with eruption column heights and thus scales with mass discharge rate.

Several laboratory studies have investigated rapid decompression on analogue material (i.e., Ichihara *et al.*, 2002; Mourtada-Bonnefoi and Mader, 2004; Namiki and Manga, 2005, 2006; Kameda *et al.*, 2008).

Fragmentation experiments on natural volcanic material have first been performed by [Alidibirov and Dingwell \(1996a,b\)](#) followed by various studies that analyzed the influence of experimental setup, sample size, porosity, permeability and sample chemistry on the fragmentation process ([Spieler \*et al.\*, 2003, 2004](#); [Kennedy \*et al.\*, 2005](#); [Scheu \*et al.\*, 2008](#); [Mueller \*et al.\*, 2008](#); [Alatorre-Ibargüengoitia \*et al.\*, 2010](#)). Most recently, [Alatorre-Ibargüengoitia \*et al.\* \(2011\)](#) proposed a model to link fragmentation speed and ejection velocity of the gas-particle mixture in rapid decompression experiments based on the shock-tube principle. [Kremers \*et al.\* \(2010\)](#) showed that varying stress distributions and decompression rates strongly influence the experimentally measured fragmentation speed. However, their setup did not allow to find an analytical solution for decompression rates. Furthermore, the determination of the fragmentation threshold had to be based on a small number of experiments, resulting in a decrease in precision.

We designed a new experimental setup for rapid decompression experiments on samples of 60 mm in diameter to complete the following tasks: (1) determine the fragmentation threshold for large samples (60 x 60 mm); (2) quantify the influence of varying decompression rates; (3) validate and extend a fragmentation speed - particle velocity model introduced by [Alatorre-Ibargüengoitia \*et al.\* \(2011\)](#).

The large sample size allowed us to investigate natural samples containing large crystals and particularly large vesicles, significantly extending the sample variability we are able to analyze. Additionally, we measured the particle velocity of a series of experiments using the technique described in [Alatorre-Ibargüengoitia \*et al.\* \(2011\)](#). The results will enable us to reassess the value of experimental key parameters and those that are of second order importance to the fragmentation process. A comparison to various recent studies will evaluate previously observed trends in terms of the influence of sample size, crystal and vesicle size and decompression rate in the fragmentation experiments. Finally, we introduce an energy budget model that allows for a correlation of decompression rate, particle speed and (experimentally applied) overpressure.

### 3.3 Methodology

---

We performed rapid decompression experiments using a setup based on the shock tube principle. We used a high pressure autoclave for pressurization of the samples that can be operated up to 50 MPa pressure (see Appendix 3.9). The overlying low-pressure tank is separated by a combination of imprinted metal plates (diaphragms) used to precisely define the experimental pressure. In an experiment we recovered the ejected particles from the tank and analyzed their grain-size distribution. The setup resembles largely the one used in [Kremers \*et al.\* \(2010\)](#), with the difference that we are now no longer use reduction rings to restrain the sample. In addition, we increased the vertical dimension of the autoclave allowing a 1D representation of the wavefront as it reaches the sample.

### 3.3.1 Fragmentation threshold

In order to determine the fragmentation threshold (i.e., the pressure at which the sample gets completely fragmented for the first time) we slowly increased the experimental pressure for each sample set until full fragmentation occurred. As a starting pressure we chose a value below the best fit identified by [Spieler \*et al.\* \(2004\)](#) as a function of open porosity.

### 3.3.2 Fragmentation speed

The fragmentation speed is a measure for the velocity of the layer-by-layer fragmentation process propagating through the sample. It is calculated for each experiment based on pressure recordings of two dynamic pressure transducers above and below the sample, using the time difference in pressure drop between the transducers and the known distance in between.

### 3.3.3 Particle velocity

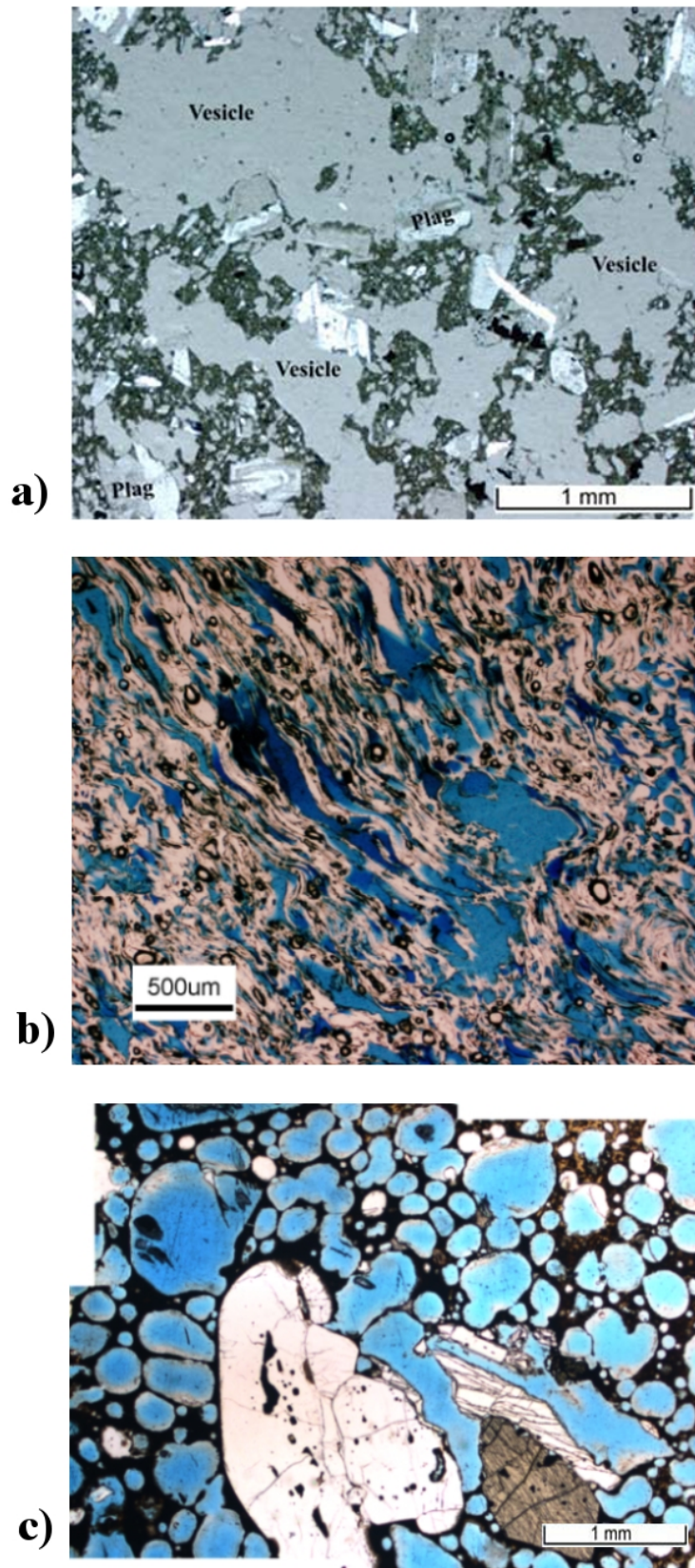
We slightly modified the experimental setup to measure the particle velocity of the fragmented samples. We inserted a plastic cylinder 0.5 m in height between bottom plate and low-pressure tank that allowed high-speed video recording of the experiment. A high-speed camera (Phantom v710) was triggered by a data acquisition system using the pressure drop at the upper dynamic pressure transducer to record the particle movement. We set the frame rate to 15000 fps in all experiments which allows for a record length of approximately 2 s. By tracking single particles with the software ImageJ ([Abràmoff \*et al.\*, 2004](#)) we were able to determine a velocity profile over the duration of the experiment.

## 3.4 Samples

---

In this study we analyzed samples collected from Lipari (Italy), Mt. Merapi (Indonesia) and Mt. Yasur (Vanuatu). Samples were drilled and cut in cylindrical blocks of 60 x 60 mm with careful preservation of any present flow alignment. We determined density and porosity for each sample using a helium pycnometer (AccuPyc 1330, Micromeritics).

After preparation we glued the samples in stainless-steel sample holders using a mounting adhesive (Crystalbond 509). The sample holder was then mounted in the high-pressure autoclave. Part of the experiments were performed in a field campaign with aim to combine laboratory experiments with field monitoring techniques such as Doppler radar or infrasound ([Kueppers \*et al.\*, 2012](#)). For these experiments no grain-size analysis could be conducted.



### 3.4.1 Lipari

The pumiceous material from the Rocche Rosse sequence on Lipari shows a wide range of bubble sizes from 20 up to 3000  $\mu\text{m}$ . Therein, the majority shows elongated shapes (Fig. 3.1 a). The mineral fraction of the analyzed thin sections is below 5 % with alkali feldspars of a maximum size of 3 mm being the main mineral phase. Additionally, smaller sized olivine crystals are abundant (Siegel, 2010). The Lipari samples show open porosities from 39 – 65%.

### 3.4.2 Mt.Merapi

The analyzed samples were collected from the deposits of the 1998 block-and-ash-flow event. These are characterized by open porosities from 18 – 41%. The pore texture shows a irregular, complex network of deformed bubbles with sizes of 20  $\mu\text{m}$  up to 2 mm (Fig. 3.1 b). The solid phase consists of 40-50 % plagioclase and pyroxene phenocrysts (1 – 2 mm) and a microcrystalline phase (Mueller, 2007).

### 3.4.3 Mt.Yasur

Analysis of the Mt.Yasur thin sections reveal bubble sizes ranging from  $10^{-5}$  - 1 mm size. The bubbles show regular spherical shapes up to highly irregular stretched patterns, probably including coalescence and shearing (Fig. 3.1 c). Their size ranges from a few  $\mu\text{m}$  up to several mm. The overall open porosity is 54 – 78%. The crystals range in size up to several mm were found to be mostly plagioclase (labradorite) with some pyroxene (augite; Kremers *et al.*, 2012b).

## 3.5 Results

---

We performed in total 35 experiments on three sample sets shown in Tab. 4.1 with connected porosities from 18 - 78 %. This large range allows us to make statements of a general meaning. Following the points raised in the introduction, we begin by determining the fragmentation threshold for large scale samples. Subsequently, we analyze the data for fragmentation speed and particle velocity.

### 3.5.1 Fragmentation threshold

The results of all fragmentation experiments are plotted as a function of  $\phi$  and  $\Delta P$  (Fig. 3.2). Further, we compare the fragmentation threshold ( $p_{th}$ ) achieved in this study (red marks) to  $p_{th}$  values resulting from earlier studies using a sample diameter of 25 mm (grey marks; Mueller *et al.*, 2008). The pressure steps applied to determine the  $p_{th}$  of a sample are depicted

in Fig. 3.2 by individual symbols: a cross marks experiments where no fragmentation occurred and solid spheres full fragmentation of the sample. All grey marks denote full fragmentation. The black and red curve indicate the fragmentation criterion developed by Koyaguchi *et al.* (2008) for each sample size:

$$p_{th} = \frac{2S_3(1 - \Phi)}{3\Phi\sqrt{\Phi^{-1/3} - 1}} \quad (3.1)$$

where  $p_{th}$  denotes the fragmentation threshold,  $\Phi$  is the porosity and  $S_3$  the effective tensile strength.

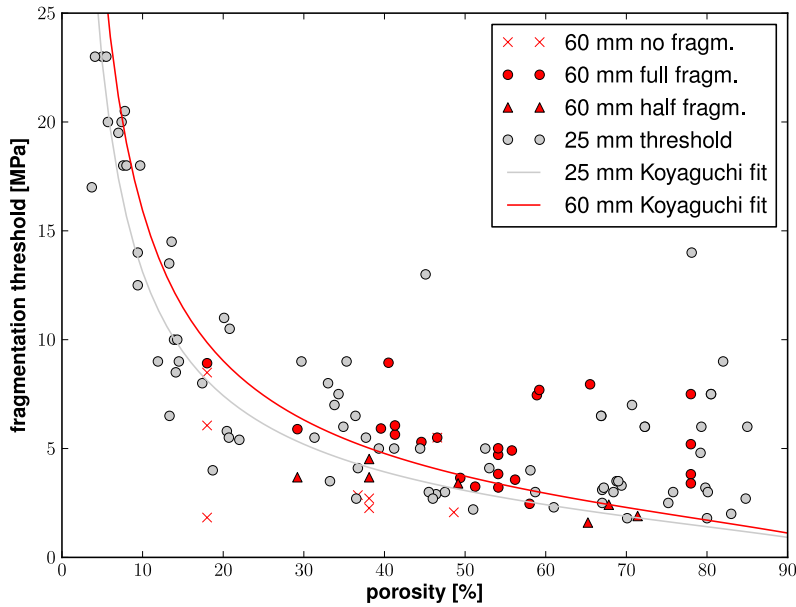


Figure 3.2: Porosity vs fragmentation pressure data as published by Mueller *et al.* (2008) (grey marks) in comparison to data gained in this study (red marks). A 'x' marks experiments where no fragmentation occurred and a '•' full fragmentation of the sample. The black and the red line mark the Koyaguchi fit for the 25 and the 60 mm data, respectively.

The differing curves for the "Koyaguchi criterion" result of the estimation of  $S_3$ . Performing non-linear least-squares analysis on the data delivered  $S_3 = 2.348$  MPa for the 25 mm experiments (black curve) and  $S_3 = 2.853$  MPa for the 60 mm experiments of this study (red curve). A possible explanation for  $S_3(60 \text{ mm}) > S_3(25 \text{ mm})$  is the strain hardening effect (Ramesh, 2008). We will show later that the faster pressure decay in the 60 mm experiments causes a higher decompression rate. This results in an increased effective tensile strength which could be manifested in a higher  $S_3$ . However, our dataset is not sufficient to verify

this effect.

Although we have a lack of data in the very low end of the porosity scale we argue that our fit of the threshold data closely resembles the one of [Mueller \*et al.\* \(2008\)](#). They showed that the deviation of their data in the high-porosity region to higher  $p_{th}$  is caused by high permeability. In similarity, a high permeability is most likely to cause the comparatively high  $p_{th}$  values for some of our investigated samples.

### 3.5.2 Fragmentation speed

A quantity that allows the comparison of fragmentation speed results using samples with highly differing porosities is the energy density  $\rho_E$ . It was introduced by [Scheu \(2005\)](#) and defines the energy available from gas expansion for fragmentation per unit volume. It denotes as:

$$\rho_E = \Delta P \cdot \phi \quad (3.2)$$

where  $\Delta P$  is the applied pressure difference and  $\phi$  is the open porosity. The corresponding SI-unit of  $\rho_E$  is  $\frac{J}{m^3}$ .

The fragmentation speed results from various sites and different studies can now be compared based on a common unit (Fig. 3.3). All experiments performed in this study are marked by red triangles, the black and grey symbols indicate fragmentation speeds obtained for samples from Mt. St. Helens and Mt. Merapi (17 mm; [Spieler \*et al.\*, 2004](#)), Montserrat and Mt. Unzen (25 mm; [Scheu, 2005](#); [Kennedy \*et al.\*, 2005](#); [Scheu \*et al.\*, 2006](#)), respectively. At comparable energy density, we observe a trend towards higher fragmentation speed when performing experiments with the 17 and 60 mm samples, compared to the 25 mm experiments. However, both the 17 and the 60 mm experiments were performed at relatively low energy densities, resulting in an uncertainty of the fragmentation speed behavior in the high energy density regime. The 17 and 60 mm experiments follow a more common trend compared to the 25 mm experiments which is caused by the larger difference in setup aspect ratio. The observed trend towards higher fragmentation speed closely matches the results from [Kremers \*et al.\* \(2010\)](#), which was interpreted as the influence of a variation in decompression rate caused by the differing setups.

### 3.5.3 Particle velocity

In 12 experiments we recorded the ejected particles using a high speed camera. The top of Fig. 3.4 presents a sequence of still-frames taken from the recording of experiment on the sample VANBB 13 (Mt. Yasur) at 7.45 MPa and 59 % open porosity. In agreement with [Alatorre-Ibargüengoitia \*et al.\* \(2011\)](#), we first observe the escaping gas after the burst of the diaphragm. As the particle ejection velocity is slower than the gas velocity a region of relatively low pressure evolves between gas and the following gas-particle mixture. These first particles are moving in a channeled flow at high velocities which is then rapidly decaying as

the pressure drops. We gained the particle velocity by tracking single particles over a distinct time frame (10 frames with  $\Delta t = 67 \mu s$ ). The bottom of Fig.3.4 shows the results of all recorded experiments as a function of time after bursting of the diaphragm. We observe that independent of the porosity and/or energy density all curves decay non-linearly following the equation introduced by Alatorre-Ibargüengoitia *et al.* (2010):

$$v_p = \frac{v_{max}}{1 + \frac{v_{max}}{h} t} \quad (3.3)$$

where  $v_{max}$  is the maximum particle velocity measured at the position of the camera,  $h$  is the distance between the original position of the bottom of the sample before the experiment and the position the particle is observed by the high-speed camera. The results indicate that in the initial stage of the flow the maximum particle velocity scales quasi-linear with applied overpressure which can be attributed to a major release of kinetic energy. Following this, we conclude that equation 3.3 is valid independent of sample aspect ratio or size and furthermore that crystal and vesicle distribution or size has no major influence on particle speed.

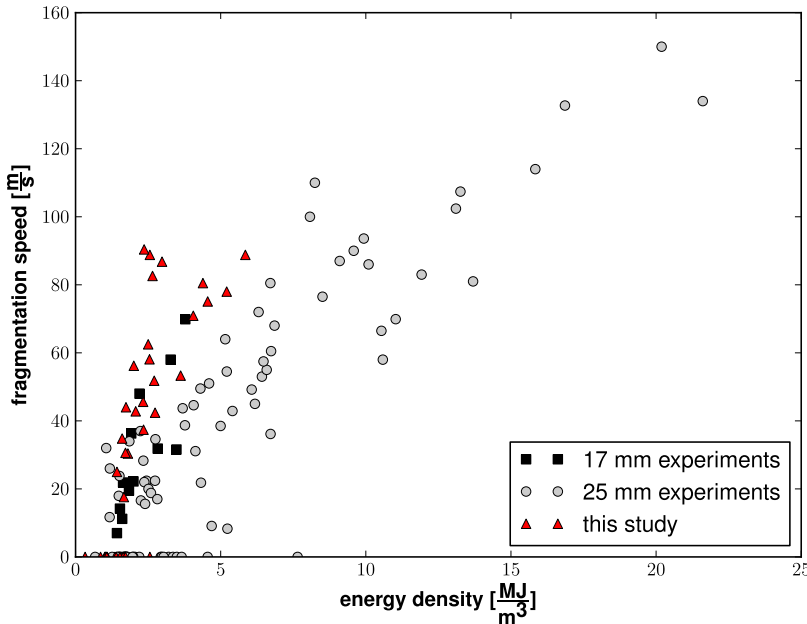


Figure 3.3: Energy density versus fragmentation speed for all analyzed samples (red triangles) compared to recent studies using a sample size of 17 mm (black squares) and 25 mm (grey spheres). The trend of fragmentation speed results varies significantly for the different sample sizes.



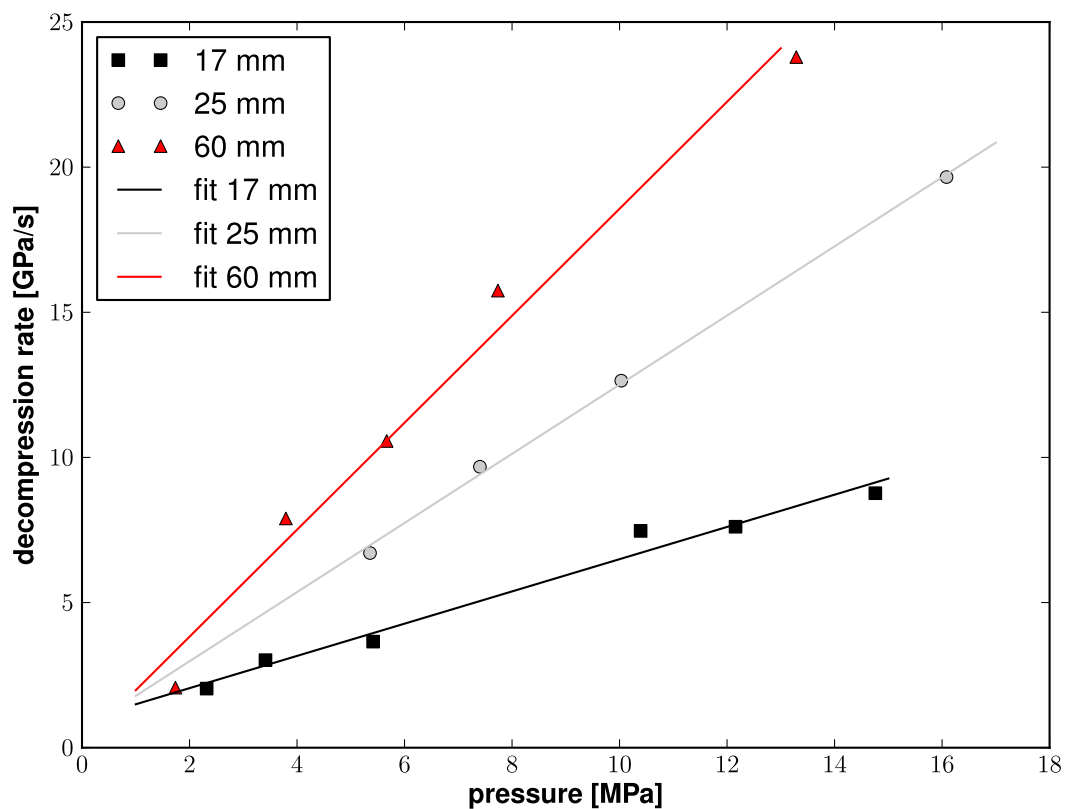


Figure 3.5: Pressure versus experimentally determined decompression rates for the 17 (black squares), 25 (grey spheres) and 60 mm (red triangles) setups. The solid lines show the corresponding linear regression.

## 3.6 Decompression rate

### 3.6.1 Determination of decompression rate

In the last years, various studies have investigated the influence of decompression rate on magma analogues (e.g., Kameda *et al.*, 2008; Ichihara *et al.*, 2002; Mourtada-Bonnefoi and Mader, 2004; Namiki and Manga, 2005). Kremers *et al.* (2010) were the first to study the behavior of natural volcanic material on varying decompression rates in laboratory experiments. They stated that these variations caused by differing experimental setups are believed to have a major influence on the strongly varying results in terms of measured fragmentation speed (see Fig. 3.3). In their study, a correction for this effect was applied to allow a comparison to various recent studies, however, a thorough quantification of the effect was prevented by the setup design. Our new setup now allows for a measurement of the effective decompression rate and by that a quantification of the influence of varying decompression rates.

Initially, fragmentation experiments on natural samples were conducted with 17 mm sample diameter, later changed to 25 mm and recently to 60 mm. For the determination of the setup-specific decompression rates we performed experiments with empty crucibles. Decompression rates were calculated as:

$$\dot{P}_{exp} = \left( \frac{\max(P^{lo} - P^{up})}{\Delta t} \right) \quad (3.4)$$

where  $P^{lo}$  and  $P^{up}$  denote the recorded pressure at the lower and upper pressure transducer, respectively, and  $\Delta t$  the time interval between start of decompression and maximum pressure difference. The measured effective decompression rate increases with applied pressure from the 17 to the 25 and further to the 60 mm setup (Fig. 3.5). This allows us to correlate the initial overpressure with the effective decompression rate for each of used setups or varying aspect ratios.

### 3.6.2 Effect of decompression rate on fragmentation behavior

In order to account for the effect of decompression rate we introduce the normalized energy supply rate  $\dot{\psi}$ , which is the (setup-specific) decompression rate normalized on a unit volume and unit time:

$$\dot{\psi} = \dot{P} \cdot \phi \quad (3.5)$$

where  $\dot{\psi}$  is the normalized energy supply rate,  $\dot{P}$  is the decompression rate and  $\phi$  is the vesicularity of the melt prior to eruption. The corresponding unit denotes as  $\frac{GJ}{m^3s}$ . In addition,  $\dot{\psi}$  can also be calculated using  $\rho_E$  and  $\Delta P$  as:

$$\dot{\psi} = \dot{P} \cdot \frac{\rho E}{\Delta P} \quad (3.6)$$

We retrieve the effective decompression rate for each setup as described in section 3.6.1. In doing so, the introduction of  $\dot{\psi}$ , allows us to plot the dataset presented in Fig. 3.3 as a function of  $\dot{\psi}$  and thereby accounting for any variability in the data that is solely introduced by setup diversity (Fig. 3.6). We observe that our data and those of previous studies now follow a more common trend. This result indicates that wall effects and other boundary conditions such as amount and adhesive strength of the used glue have only minor influence on the experimental results. However, changes in aspect ratio of setup and/or sample can cause strong variations in decompression rate and thus in fragmentation speed results.

The  $p_{th}$  shows only a very minor dependency on  $\dot{P}$  as long as the decompression acts fast enough compared to the permeable gas loss. Consequently, the strength that has to be overcome ( $S_3$  in the Koyaguchi criterion) also depends only minor on  $\dot{P}$ .

Contrastingly to the  $p_{th}$  behavior, the fragmentation speed depends strongly on  $\dot{P}$ . The speed of fragmentation describes how fast the layer-by-layer fragmentation front is propagating through the sample; in other words, the speed of a repeated reaching of the fragmentation criterion. The time interval between two consecutive fragmentation events depends on  $\dot{P}$ , as this defines how fast a critical pressure gradient can be reached. Full fragmentation of the sample requires several layer-by-layer fragmentation events, which is why the time-effect of  $\dot{P}$  is adding up to a strong effect.

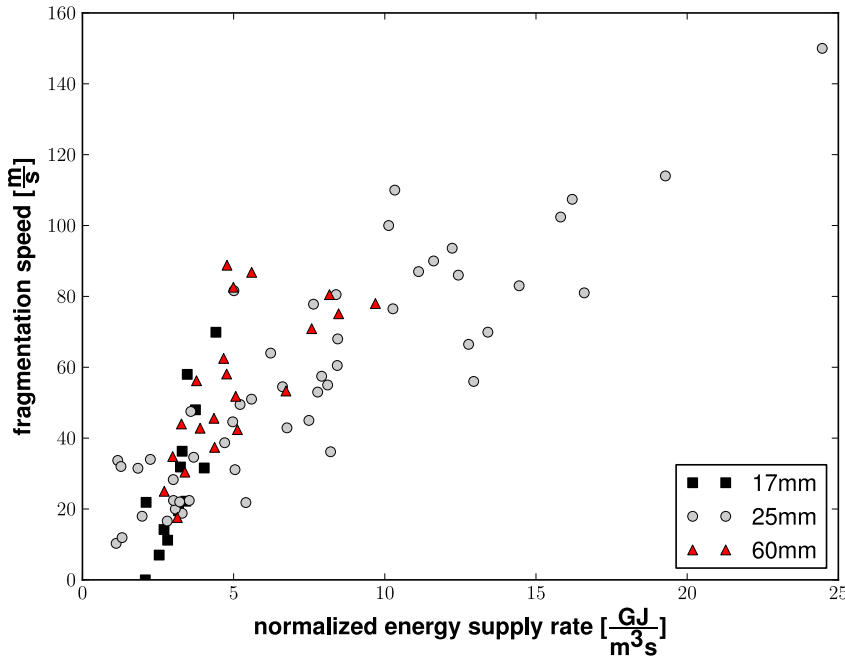


Figure 3.6: Normalized energy supply rate  $\dot{\psi}$  versus fragmentation speed for all analyzed samples (red triangles) compared to recent studies using sample size of 17 mm (black squares) and 25 mm (grey spheres). The fragmentation speed results for the different sample sizes now follow a more common trend.

### 3.7 Energy budget model

Alatorre-Ibargüengoitia *et al.* (2011) presented a model that relates the fragmentation speed  $U$  to the ejection velocity  $v$  of the gas-particle mixture. It denotes as:

$$P_{mix} = P_o \left( \frac{U}{a_o} \right)^{\frac{2\gamma}{\gamma+1}} \quad (3.7)$$

$$v = a_{mix} - U + \frac{2\sqrt{n\gamma RT_o}}{\gamma - 1} \left( \frac{P_{mix}}{P_o} \right)^{\frac{\gamma-1}{2\gamma}} \left( 1 - \frac{P_{fi}}{P_{mix}} \right)^{\frac{\gamma-1}{2\gamma}} \quad (3.8)$$

where the subscripts "o" and "mix" refer to parameters at initial conditions and at the gas-particle mixture region right after the onset of fragmentation, respectively,  $\gamma$  is the specific heat capacity ratio (will be discussed later in detail),  $a$  is the sound speed of the gas-particle mixture,  $T$  is the temperature,  $n$  is the mass fraction of gas,  $R$  is the gas constant and  $P_{fi}$  is the final pressure. For derivation and the required assumptions under which these equations are valid we refer the reader to Alatorre-Ibargüengoitia *et al.* (2011).

The theoretical fragmentation speed can be estimated using a logarithmic expression introduced by Scheu *et al.* (2006):

$$U = k_p \ln \left( \frac{P_o}{P_{th}} \right) \quad (3.9)$$

where  $k_p$  is a constant and  $p_{th}$  is the fragmentation threshold.

Using the equations we were able to calculate the theoretical velocity of the gas-particle mixture at the position of the camera and the theoretical fragmentation speed. For a determination of the experimentally generated velocity of the gas-particle mixture we have to assure that the specific heat capacity ratio  $\gamma$ , considering only the fraction of particles in equilibrium with the gas ( $f$ ), is estimated correctly. This value was determined from the grain-size distribution of the ejected particles, considering only particles smaller than 1 mm. We obtain  $f$  values in the order of  $0.7 \pm 0.2$  %.

In Fig. 3.7 we compare the theoretical and measured particle speed of the Mt. Yasur sample set as a function of  $\dot{\psi}$ . The lines represent the theoretical results obtained by using the code of Alatorre-Ibargüengoitia *et al.* (2011). The solid spheres give the measured particle velocity. Both values are corrected for the setup influence as described in section 3.6.1 and 3.6.2. The theoretical and the measured particle speed for various initial pressures as a function of  $\dot{\psi}$  delivers an overall good fit of experimental and theoretical data (Fig. 3.7). The method allows a correlation of measured particle speed to decompression rate and initial overpressure, meaning that it allows for an estimate of initial overpressure if the speed of the erupted particles, the decompression rate and the vesicularity of the material at the time of the eruption are known.

### 3.7.1 Application to Volcán de Colima (Mexico) and Mt. Yasur (Vanuatu)

In an attempt to invert for decompression rate and initial gas overpressure we apply the presented model to two volcanoes where the necessary parameters (particle velocity and porosity) have been measured recently. The eruption mechanisms at Volcán de Colima and Mt. Yasur and the setup in the lab are shown in a schematic drawing in Fig. 3.8. Generally, decompression rates in explosive volcanic eruptions are estimated as  $10^4 \frac{Pa}{s}$  (Namiki and Manga, 2006) up to  $10^6 - 10^8 \frac{Pa}{s}$  (Toramaru, 2006).

#### Volcán de Colima

Volcán de Colima is a stratovolcano that is characterized by recurrent episodes of dome-growth and Vulcanian eruptions with accompanying lava flows (e.g., Zobin *et al.*, 2002; Varley *et al.*, 2010; Lavallée *et al.*, 2011). Scharff *et al.* (2011) measured mean particle velocities of Vulcanian eruptions at Volcán de Colima using a Doppler Radar. They observe particle velocities ranging from 30 - 60  $\frac{m}{s}$ . The open porosity of erupted material from the same period was measured in a field campaign to vary between 5 - 50 % (Lavallée *et al.*, 2011). As high particle velocities are presumably linked to the fragmentation and ejection of highly vesicular melt, we choose  $\phi = 40$  % which is on the upper end of the porosity scale for our inversion approach. However, this might still be underestimating the pre-eruptive vesicularity in the conduit. For the inversion, we use the range in measured particle velocities by the Doppler-Radar to infer the  $\dot{\psi}$  from the model presented in Fig. 3.7; the open porosity delivers the corresponding estimated decompression rate (see equation (4)). The approach estimates a range of 0.75 - 1.25  $\frac{GPa}{s}$  for the decompression rates at Volcán de Colima. These values are quite high, however still in the range of estimated decompression rates for explosive volcanic eruptions.

#### Mt. Yasur

Volcanic activity at Mt. Yasur (Tanna island, Vanuatu) has been exemplified by regular Strombolian eruptions for the last 300 years (Simkin *et al.*, 1981). Currently, this activity takes place at three vents with highly varying recurrence rates (Oppenheimer *et al.*, 2006). During a six-week field campaign in August-September 2008 we installed four seismic arrays, two Doppler-radars, four infrasound arrays and an infrared camera at Mt. Yasur (Meier *et al.*, 2009; Kremers *et al.*, 2012b). The measurements focussed on a single vent showing very regular explosive events that allowed a direct observation of the vent exit. Meier *et al.* (2009) measured mean particle velocities from 30 - 100  $\frac{m}{s}$ . The porosity of the erupted products ranges from 54 - 78 % (this study). Again, we choose a porosity at the upper end of the scale,  $\phi = 70$  %. The decompression rate and overpressure can be estimated similar

to the results presented in Fig. 3.5, if the slug/conduit geometry is known. We assume a slug diameter of 10 m at depth based on the measurement of the conduit diameter at the surface of 15 m (*K. Meier personal communication*). Meier *et al.* (2009) find frequencies of the resonating cavity (the slug) of 2 Hz from spectral analysis of infrasound records. Vidal *et al.* (2006) showed experimentally that the resonance frequency is directly correlated with the slug geometry, i.e. the length and the diameter of the resonator. The relation for the fundamental wavelength  $\lambda_0$  denotes as:

$$\lambda_0 = 4L' \quad (3.10)$$

with

$$L' = L + \delta L \quad (3.11)$$

$L'$  is called the effective length, which is the real length of the resonator  $L$  plus a correction factor  $\delta L$  that depends on the opening diameter. For the estimation of the slug length we use an atmosphere at 600 – 800°C consisting mainly of water vapor. The sound speed in this medium ranges between 700 and 800  $\frac{m}{s}$  (Kieffer, 1977). Applying the  $\frac{\lambda}{4}$  method we retrieve 80 – 94 m for the slug length.

According to the results of empty experiments presented in Fig. 3.5 that closely resemble the burst of a bubble on top of a cavity, we can state that the ratio of overpressure to decompression rate depends on the ratio diameter divided by length of the decompressed cavity. We use the gained fraction of the estimated source dimensions at Mt. Yasur and performing a linear least squares fit to the laboratory data. This delivers the desired overpressure to decompression rate relation comparable to Fig. 3.5. By applying the energy budget model and using the measured particle velocities at Mt. Yasur this yields a range in decompression rate from 0.43 – 2.43  $\frac{GPa}{s}$ . With the measured sample porosity we retrieve a range of 0.77 – 2.57 MPa for the bubble overpressure. The estimated overpressure and slug sizes prior to bursting at the surface are in good agreement with previous studies at Stromboli (Chouet *et al.*, 2003) and Mt. Erebus (Gerst, 2010).

The estimated values for decompression rates certainly define an upper limit due to the underestimation of pre-eruptive vesicularity. A higher porosity will deliver additional energy to the fragmentation process that will be transferred in particle speed. Therefore,  $\dot{\psi}$  as predicted by the model, depending on the measured particle speed, is also to be seen as an upper limit. It has to be mentioned that these results are only valid if the fragmentation front is located in a shallow part of the volcanic edifice, as mimicked by the laboratory experiments. The calculated values for Mt. Yasur can only be seen as a rough approximation, as the eruptive mechanism can only be partly explained by brittle fragmentation of magma. Nevertheless, we argue that the gained values define an upper bound for the decompression rate also at Mt. Yasur. Generally, the values are in the range of decompression rates described by Toramaru (2006) according to a model in which the bubble nucleation propagates downward as

a rarefaction wave in the conduit. This shows that the presented model is applicable in the field and delivers reasonable results if all required parameters have been measured.

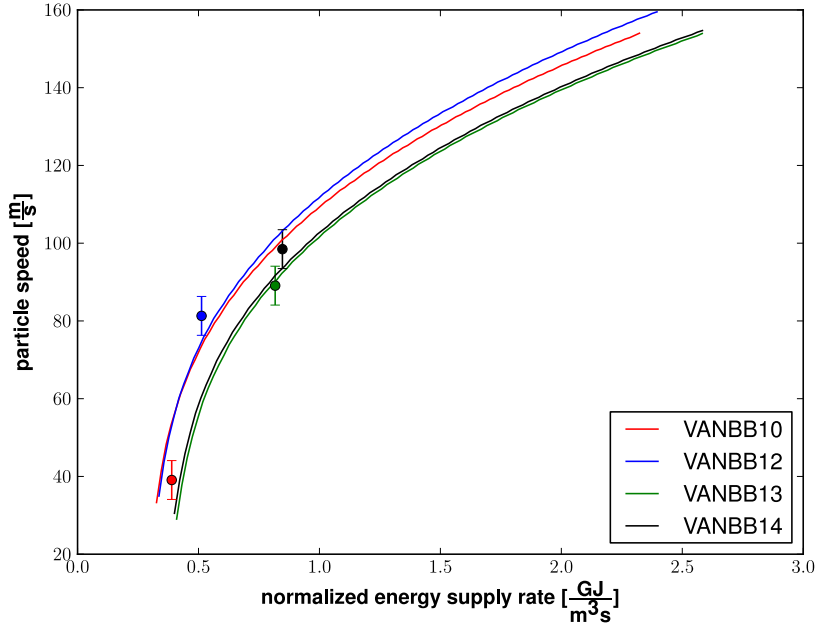


Figure 3.7: Measured particle velocities for several experiments (colored spheres) compared to numerical simulations (colored lines) using the numerical code presented in [Alatorre-Ibargüengoitia \*et al.\* \(2011\)](#). The error bars give the uncertainty in particle speed determination ( $\pm 5 \frac{m}{s}$ ).

## 3.8 Conclusions

We performed rapid decompression experiments using a newly designed setup that increases the sample size to 60 mm. The results were compared to those of various recent studies using smaller sample sizes. Coming back to the questions raised in the introduction we can make the following statements: (1) We determined the fragmentation threshold for large samples and show that it seems to be independent of sample size; (2) The measured decompression rates for the varying setups have a major impact on fragmentation speed results; (3) We introduced the normalized energy supply rate  $\dot{\psi}$  in order to quantitatively compare the results of various sample sizes; (4) The fragmentation speed results of various samples sizes follow a common trend when we use  $\dot{\psi}$ ; (5) The measured particle velocities follow the equation introduced by [Alatorre-Ibargüengoitia \*et al.\* \(2010\)](#); (6) Experimental to theoretical particle ejection velocity data are in good agreement and thus allow a correlation of measured velocities to decompression rate and initial gas-overpressure; (7) The decompression rates deduced from our model for Volcán de Colima and Mt. Yasur are quite high, but still in a range of previously suggested values ([Toramaru, 2006](#)); (8) The slug sizes and overpressure determined in the Mt. Yasur case study are in good agreement with previous

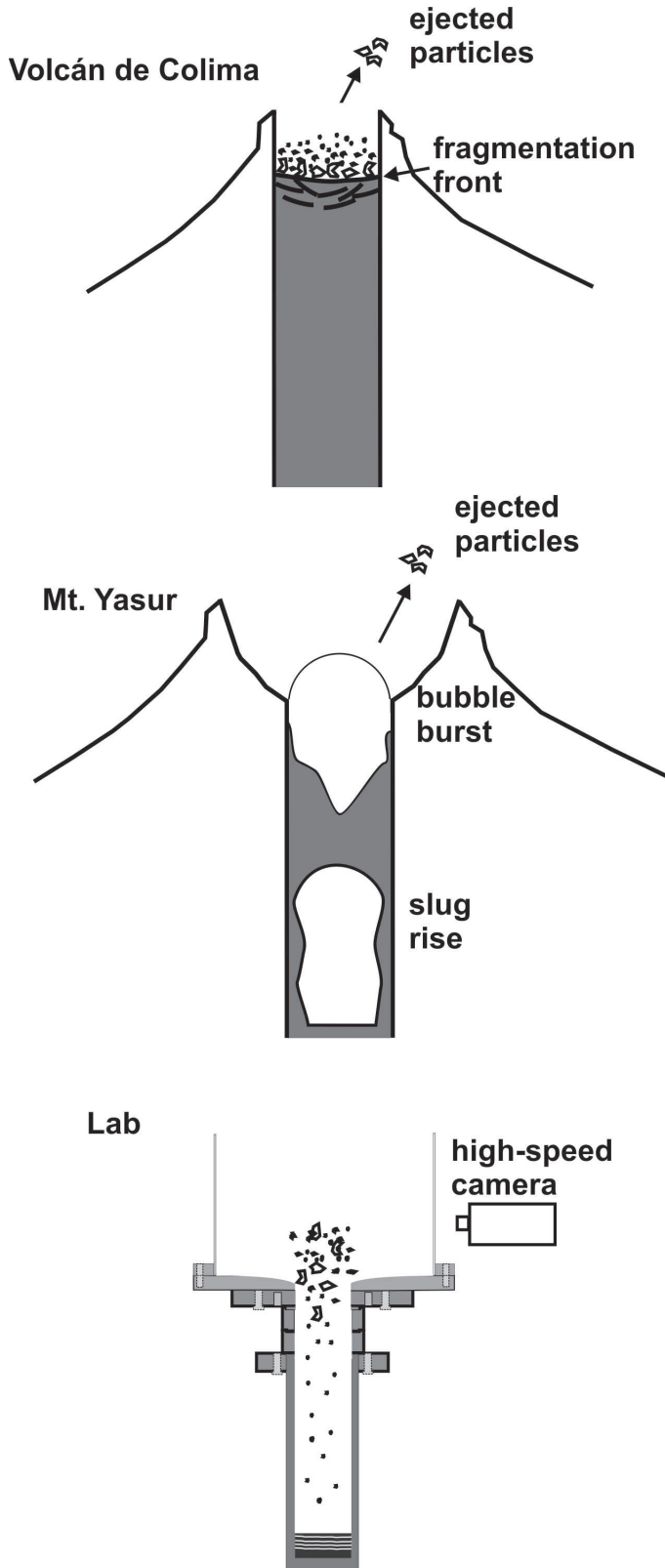


Figure 3.8: Schematic drawing of the analyzed eruption scenarios. *top*: Fragmentation in a shallow conduit induced by rapid decompression at Volcán de Colima; *middle*: Strombolian bubble burst at Mt. Yasur; *bottom*: Measurement of particle ejection velocity in the lab following rapid decompression.

studies at Stromboli (Chouet *et al.*, 2003) and Mt. Erebus (Gerst, 2010). The results show the importance of a thorough determination of the decompression rate in fragmentation experiments. The introduction of  $\dot{\psi}$  allows to remove non-physical variations introduced by setup variations. Furthermore, it provides a powerful tool to correlate decompression rate to particle ejection velocity and initial gas overpressure. This may well lead to a better understanding of fragmentation events in nature and in turn improve hazard assessment.

## 3.9 Appendix

---

### 3.9.1 Fragmentation setup

The used setup for the fragmentation experiments is based on the shock tube principle. The high pressure autoclave is used for pressurization of the samples and can be operated up to 50 MPa pressure (Fig. 3.9). The overlying low-pressure tank is at atmospheric conditions and is used to recover the ejected particles. The experimentally applied pressure is controlled by a combination of imprinted metal plates (diaphragms) and recorded with a set of pressure transducers. From these records the fragmentation threshold and speed can be determined.

### 3.9.2 Experimental overview

An overview over the determined experimental parameters for the three analyzed datasets is given in Tab. 4.1.

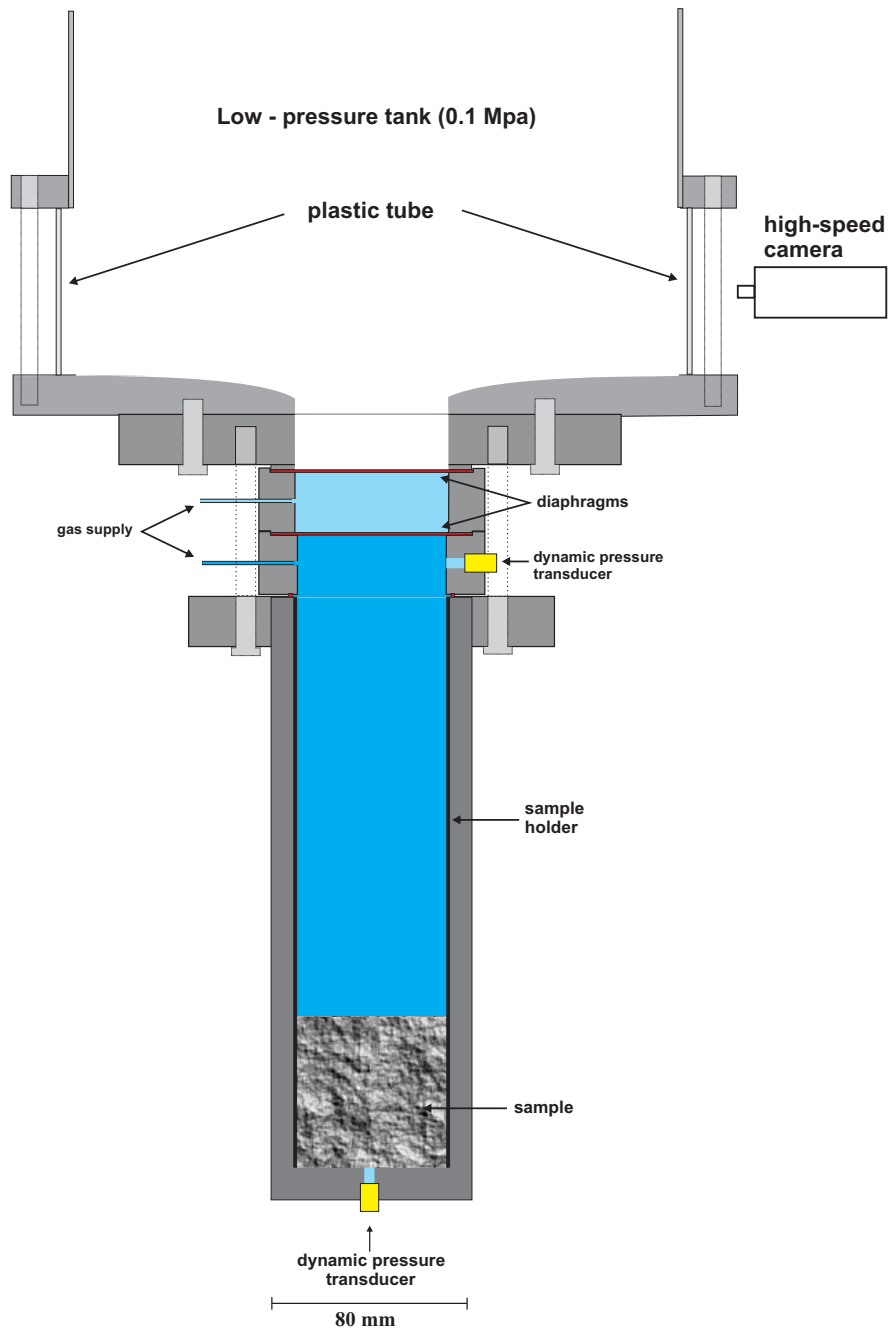


Figure 3.9: The high pressure autoclave in a schematic image in scale with a sample placed in it as used in the experiments. The two dynamic pressure transducers are used to monitor pressurization, the diaphragms separate the system from the overlying low-pressure tank. In between a plastic tube was inserted to allow a recording of the particle-gas mixture with the high-speed camera.

sample	density [ $\frac{g}{cm^3}$ ]	open porosity [%]	fragm. pressure [MPa]	energy density [ $\frac{J}{cm^3}$ ]	fragm. speed [ $\frac{m}{s}$ ]	max. particle velocity [ $\frac{m}{s}$ ]	$\psi$ [ $\frac{GJ}{m^3s}$ ]
LIP 1	2.237	46.56	5.5	2.56	127.7	-	4.78
LIP 2	2.183	46.54	5.5	2.56	88.8	-	4.78
LIP 3	1.847	44.58	5.3	2.36	90.4	-	4.42
LIP 4	1.842	49.39	3.65	1.80	30.4	-	3.39
LIP 5	2.132	49.13	3.4	1.67	0.0	-	-
LIP 7	1.653	51.25	3.25	1.67	17.6	-	3.14
LIP 8	2.324	39.57	5.92	2.34	37.4	57.23	4.37
LIP 9	2.331	48.60	2.07	1.01	0.0	-	-
LIP E	2.013	56.26	3.57	2.01	56.2	-	3.77
LIP F2	2.132	65.54	8.94	3.62	53.5	118.08	9.69
LIP H2	1.736	40.49	7.95	5.21	78.0	75.58	6.73
VANBB 0	2.631	70.51	3.82	2.98	86.8	-	5.60
VANBB 1	2.559	78.06	5.2	4.06	70.9	-	7.58
VANBB 3	2.559	78.06	3.40	2.65	82.6	-	4.99
VANBB 4	2.757	58.73	2.46	1.43	25.0	-	2.71
VANBB 5	2.727	65.23	1.60	1.04	0.0	-	-
VANBB 6	2.70	71.40	1.90	1.36	0.0	-	-
VANBB 7	2.727	67.82	2.42	1.64	0.0	-	-
VANBB 8	2.506	54.12	3.21	1.74	44.0	-	3.27
VANBB 9	2.506	54.12	4.71	2.55	58.1	-	4.77
VANBB 10	2.506	54.12	3.83	2.07	42.8	39.08	3.89
VANBB 11	2.506	54.12	5.01	2.71	51.8	-	5.07
VANBB 12	2.645	55.81	4.91	2.74	42.4	81.30	5.13
VANBB 13	2.698	58.90	7.45	4.39	80.5	89.08	8.17
VANBB 14	2.749	59.17	7.69	4.55	75.1	98.47	8.47
MER 1	2.808	36.65	2.86	1.05	0.0	-	-
MER 3	2.793	38.13	2.26	0.86	0.0	-	-
MER 4	2.793	38.13	4.52	1.72	0.0	-	-
MER 5	2.782	41.27	5.64	2.33	45.6	-	4.35
MER 6	2.782	41.27	6.06	2.50	62.5	-	4.67
G 1	2.772	18.02	8.49	1.53	0.0	-	-
G 2	2.772	18.02	6.06	1.09	0.0	-	-
G 3	2.772	18.02	1.83	0.33	34.8	-	2.99
G 4	2.819	29.16	5.89	1.72	30.6	-	3.21
G 5	2.819	29.16	3.68	1.08	0.0	-	-

Table 3.1: Measured and experimental generated data for the sample sets from Lipari (LIP), Mt. Yasur (VAN) and Mt. Merapi (MER and G). The last column denotes the normalized energy supply rate.

## Motivation for Following Chapter

Strombolian eruptions, as epitomized by Stromboli volcano (Italy), are one of the best-studied explosive volcanic eruptions. The generally agreed-on mechanism has been described as resulting from the ascent of gas slugs - that is, decimeter- to meter-size bubbles - that burst at the free surface of the magma column (e.g., [Walker, 1973](#); [Chouet, 2003](#); [Houghton and Gonnermann, 2008](#)). A feature commonly observed - but not well understood - at Strombolian type volcanoes is simultaneous activity at various vents showing differing explosion sizes and recurrence rates ([Cole \*et al.\*, 2005](#)). The eruption dynamics are generally controlled by the magma rheology ([Dingwell, 2006](#)), that in part reflects external factors such as stress and strain rate (rapid ascent of bubble overpressure) and viscosity (changes in chemical composition, bubble content, crystal content). [Lautze and Houghton \(2005\)](#) present a model for a shallow physical mingling of magmas at different densities in the conduit of Stromboli volcano. The eruptive products show multi-modalities in crystal and bubble size distributions but are of otherwise homogeneous bulk chemistry ([Lautze and Houghton, 2006, 2008](#)). In chapter 4, (after [Kremers \*et al.\*, 2012b](#)) very similar results are shown for the eruptive products of Mt. Yasur (Tanna island, Vanuatu). The products from different eruptive styles are contrasted to reconcile the extent of chemical mixing and rheological homogenization with the recurrence rate and size of explosions.

## 4

## Petrological analysis

## Shallow magma-mingling-driven Strombolian eruptions at Mt. Yasur volcano, Vanuatu

*S. Kremers<sup>1</sup>, J. Hanson<sup>1,2</sup>, Y. Lavallée<sup>1</sup>, K.-U. Hess<sup>1</sup>, O. Chevrel<sup>1</sup>, J. Wassermann<sup>1</sup>, D.B. Dingwell<sup>1</sup>*

<sup>1</sup> Department of Earth and Environmental Sciences, Ludwig-Maximilians-University, Theresienstr. 41/III, 80333 Munich, Germany

<sup>2</sup> now at Department of Earth Sciences, University of Bristol, Queen's Road, Clifton, BS8 1RJ, UK

submitted to *Geophysical Research Letters*

## 4.1 Abstract

---

Mt. Yasur volcano (Vanuatu) has been increasingly recognized for its high-frequency Strombolian eruptions. Strombolian activity, at Stromboli volcano (Italy), is often regarded as a product of the rapid ascent of gas slugs originating from a deep magma, which mingle with a batch of shallow magma upon eruption. The presence of a range in crystallinities as well as bimodal bubble-size distributions, in the eruptive products, generally supports this view. Here, the Strombolian activity at Mt. Yasur is analyzed. A rheological investigation

of the eruptive products indicates that the basaltic-andesitic eruptive products containing an apparently homogeneous glass phase, exhibit evidence of a distinct range of glass transition temperatures with multiple peaks occurring in individual samples. Such anomalous behavior is proposed to result from the mingling of magmas with contrasting oxidation states. The anomalous nature of the measured glass transition behavior leads us to the inference that mingling is located in the shallow parts of the eruptive conduits, partly driven by rejuvenation of material slumped from the crater walls into an open conduit system. The dynamics of this process may expose the periodicity of the eruptions themselves.

## 4.2 Introduction



Figure 4.1: Still frame series of close-ups of Strombolian bubble burst at crater A. Parts of the shell that formed the bubble are still in contact. The series was acquired by a custom Canon camera at 10 fps. Image courtesy Alex Gerst.

Volcanic activity at Mt. Yasur (Tanna island, Vanuatu) has been characterized by regular Strombolian eruptions for the last 300 years (Simkin *et al.*, 1981). Currently, this activity takes place at three vents with highly varying recurrence rates (Oppenheimer *et al.*, 2006). Strombolian activity, as epitomized by Stromboli volcano (Italy), has been described as resulting from the ascent of gas slugs that is, decimeter- to meter-size bubbles that have decoupled from the melt phase that burst at the free surface of the magma column (Fig. 4.1) (Blackburn *et al.*, 1976; Wassermann, 1997; Chouet *et al.*, 2003) due to stresses generating strain rates exceeding the relaxational strain rates of the bubble wall magma (Taddeucci *et al.*, 2006). Except for brief shifts in activity to larger explosions, termed paroxysmal eruptions, the activity at Stromboli appears to recur at regular intervals, suggestive of a continuum process in an open system (Metrich *et al.*, 2009). The surface activity is inferred to reflect the ascent of magma batches at various rates, driven by the relative buoyancy of bubbles with contrasting sizes (Vergnolle, 1996; James *et al.*, 2008). This is a process that presumably leads inevitably to physical mingling in the conduit (Lautze and Houghton, 2005). The mingled eruptive products of Stromboli exhibit homogeneous bulk chemical composition, yet variable crystallinities and bimodal bubble-size distributions (Lautze and Houghton, 2006, 2008). Recent microanalytical studies on volatile concentrations in crystal-rich and crystal-free areas of erupted products have led to the idea that incipient filter-pressing melt segregation, driven by fluidization of interstitial melt due to the incompatibility

of volatiles during crystallization at shallow levels, may take place during fragmentation (Schipper *et al.*, 2011). The common bimodality of the mingled products begs the question of the potential rheological importance of shallow magma mixing in driving Strombolian activity. The rheology of magmas—their ability to flow, to exsolve volatiles, to trap bubbles, to degas and to fragment—is a central control on the eruption dynamics (Dingwell, 2006). The rheology of magmas depends critically on the viscosity of the melt, which in turn depends on chemical composition (e.g., Dingwell, 1991, 1996; Dingwell *et al.*, 1998; Dingwell, 2007; Hui and Zhang, 2007; Giordano *et al.*, 2008), on temperature (e.g., Dingwell, 1996; Hess and Dingwell, 1996), on crystal content (e.g., Caricchi *et al.*, 2007; Cordonnier *et al.*, 2009, 2012; Ishibashi, 2009; Lavallée *et al.*, 2007; Lejeune and Richet, 1995; Sato, 2005), on bubble content (e.g., Bagdassarov *et al.*, 1994; Lejeune *et al.*, 1999; Manga *et al.*, 1998; Llewellyn and Manga, 2005) and to a very minor extent pressure (e.g., Dingwell, 1998; Liebske *et al.*, 2003). Magma viscosities can now be reasonably well approximated using empirical models (Giordano *et al.*, 2008; Hui and Zhang, 2007). In iron-rich magma (such as those involved in Strombolian eruptions), iron may play a dual role depending on the oxidation state; as trivalent or divalent cations as well as occupying multiple coordination states in both valencies (e.g., Mysen *et al.*, 1984; Bouhifd *et al.*, 2004). Previous geochemical analyses of Strombolian products have revealed the general homogeneity of their bulk chemistry (e.g., Lautze and Houghton, 2006, 2008). Yet in scenarios in which magma mingling/mixing takes place at shallow depths, just prior to eruption, the extent of homogenization of subtle differences in oxidation state may influence the bulk viscosity and thus, the eruptive rheology.

Below, we describe the Strombolian activity at Mt. Yasur volcano as well as petrological and rheological analyses of the eruptive products. These observations demonstrate the importance of shallow mingling during such activity. We propose a correlation between chemical mixing and rheological homogenization processes and the recurrence rate and size of explosions.

### 4.3 Strombolian activity at Yasur volcano

---

Volcanic activity at Mt. Yasur can be traced to the late Pliocene from a series of major volcanic episodes (Carney and Macfarlane, 1979; Chen *et al.*, 1995). The most recent episode of activity formed the Siwi Group in the easternmost part of the island, and is characterized by predominantly basaltic to basaltic-andesitic deposits (Robin *et al.*, 1994; Bani and Lardy, 2007). Present activity at the Yasur cinder cone consists of Strombolian to Vulcanian activity (Carney and Macfarlane, 1979; Oppenheimer *et al.*, 2006; Bani and Lardy, 2007), produced from three small active craters (denoted as A, B and C from south to north, respectively) excavated within a larger 400-m diameter crater (Oppenheimer *et al.*, 2006) a feature commonly observed at other Strombolian systems (Cole *et al.*, 2005). At the time of a geophysical monitoring and sample collection field campaign in August–September 2008, all three craters showed very different styles of activity. Crater A, the most active vent, had an eruption recurrence periodicity of less than one minute. Crater B showed very irregular ash venting,

with variable periodicity ranging between minutes and days, while crater C produced the strongest eruptions on a longer recurrence timescale of approximately ten minutes. From our observation site we noted a considerable amount of material recycling from tephra deposited inside the vent, in addition to inward slumping of tephra off the scree slope of the crater wall A.

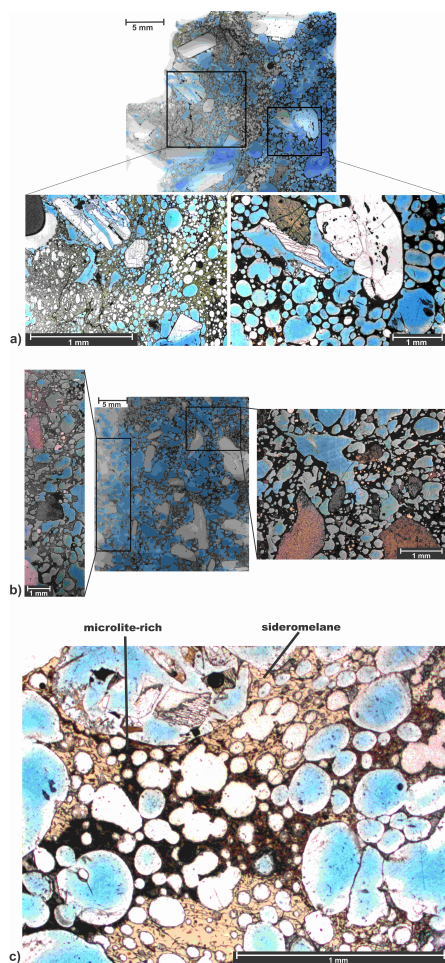


Figure 4.2: A) Scanned (top) and microscope images of thin section from sample Van A1 showing sideromelane (left) and microlite-rich (right) areas. B) Scanned (middle) and microscope thin section images of sample Van C erupted from crater C. left: sideromelane groundmass; right: microlite-rich groundmass. C) Microscope image showing contact between sideromelane and microlite-rich areas.

## 4.4 Strombolian products

For the present study, the eruptive products of craters A and C were sampled. From crater A we collected one juvenile bomb (Van A1), which was torn from the wall of a bursting bubble and impacted the ground in a deformable, viscous state, and one exotic bomb (Van A2), which appears denser, nearly spherical in shape and undeformed by ground impact. From crater C, one juvenile bomb (Van C), representing the wall of a bursting bubble and

impacting the ground in a deformable viscous state was collected (see Appendix A). The bombs Van A1 and Van C are uniformly black with abundant white millimeter-size crystals of plagioclase. The bubble shapes vary from sub-spherical to spherical and the content within a bomb grades strongly from a highly porous core to a denser glassy rim. The bomb Van A2 is light to dark-grey, almost fully crystalline and interpreted as exotic material that fell back from the crater wall into the conduit and was re-expelled during subsequent explosions. The bubbles of Van A2 show highly irregular shapes. Petrographic analysis reveals differences between these samples. First, both juvenile bombs revealed bimodal textures; that is, they contain regions of microlite-free glass (sideromelane, Fig. 4.2 a) and regions of microlite-rich groundmass (Fig. 4.2 b). The contact between each region is often sharp, though occasionally diffused contacts were noted (Fig. 4.2 c). The sideromelane regions show more fluidal structures demonstrated by the deformation and collapse structures of some bubbles than the microlite-rich regions. The edges of these deformed bubbles are commonly oxidized to a dark brown color. The microlites present in the microlite-rich regions (and sometimes in the sideromelane regions near the edge of a transition) often show a spherulitic texture suggesting crystallization of the magma under disequilibrium conditions. Sample Van A1 (from high-recurrence rate eruptive crater A) has abundant sinuous interfaces and appears heavily mingled in contrast to sample Van C (from the Crater C). In exotic sample Van A2, almost no regions of sideromelane are observed; instead, the sample is nearly entirely crystallized.

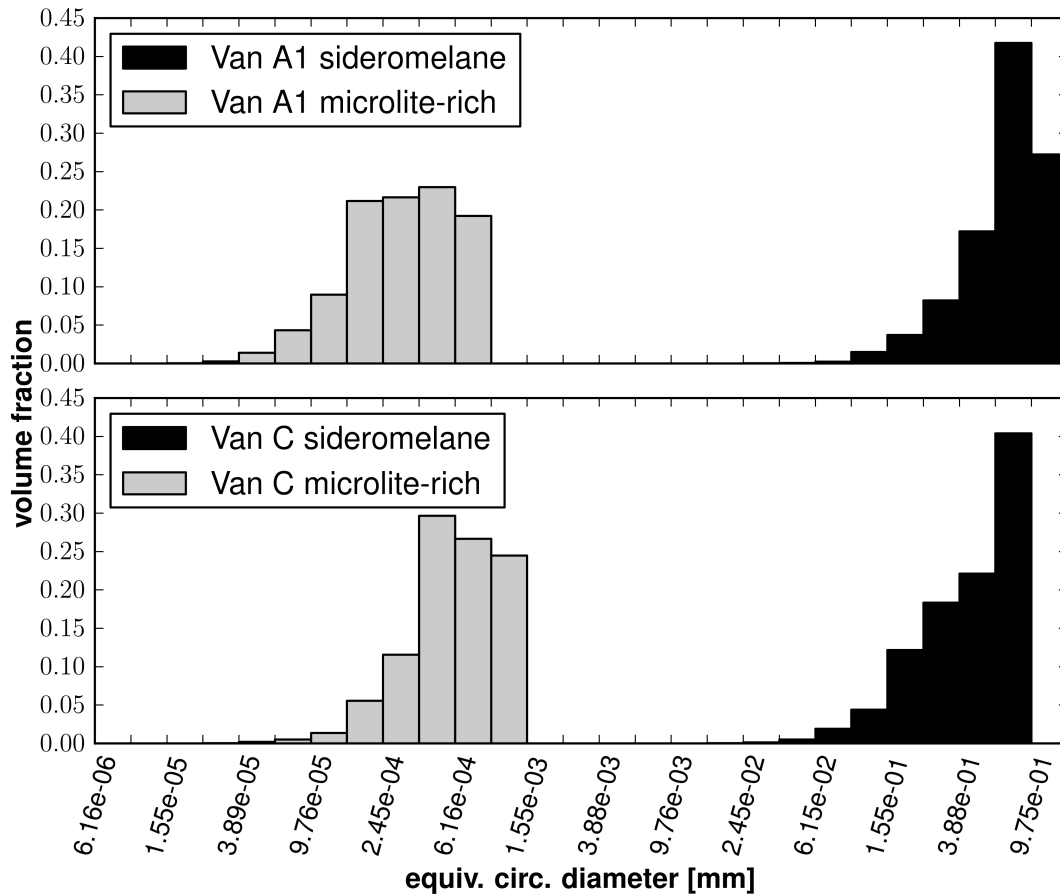


Figure 4.3: Histograms of bubble-size distributions using the equivalent circular bubble diameter for the sample Van A1 (top) and VAN C (bottom). In both two distinct single distributions for the sideromelane and the microlite-reich groundmass can be observed. Bin values are scaled following (Sahagian and Proussevitch, 1998) using a geometric scale of  $10^{-0.1}$ .

Analysis of the bubbles reveals a contrasting size distribution between the sideromelane and the crystal-rich area. Sideromelane areas are rich in small ( $< 1 \cdot 10^{-3}$  mm) vesicles whereas microlite-rich areas contain larger ( $> 4 \cdot 10^{-2}$  mm) vesicles (Fig. 4.3). This bimodal distribution is in good agreement with the results of Lautze and Houghton (2005) on lapilli from Stromboli volcano (Italy). The regular spherical shape of the vesicles in the sideromelane areas suggest a rapid cooling shortly after expansion, whereas the irregular shapes in the microlite-rich area indicate a complex deformation overprint, probably including coalescence and shearing. Bulk rock chemistry analysis using X-ray fluorescence revealed the homogeneity of the chemical composition of the eruptive products (Tab. 4.1); an observation akin to those of previous studies on Strombolian products (Lautze and Houghton, 2005, 2008). Electron probe microanalysis of the interstitial glass reveals a more evolved composition than the bulk; yet, there appears to be no chemical distinction (within the standard deviation of the measurements) between the glass in the sideromelane- and microlite-rich areas (Tab. 4.2). The crystalline phases present were found to be mostly plagioclase (labradorite; see Appendix A) with some pyroxene (augite). Thermal analyses were performed to characterize the stability of the eruptive products as well as the physico-chemical character of the glass phase. Thermogravimetric measurements show no mass loss (within the detection limit of the method 0.1 wt%) during heating to 1000 °C, which is used to infer the absence of residual water in the glass and the crystalline phases (see Appendix A). Complementary analysis of the heat capacity (Cp) reveals intricacies in the glass transition temperature (Tg) locked in during quenching of the products. Here, instead of showing a single, clear peak at the glass transition, the Cp curves of samples Van A1 and Van C produced during the burst of lava bubbles reach several successive plateaus at around 650-800 °C. For the sample Van A1 the plateau further displays the extraordinary presence of two distinct peaks at 690 and 800 °C, whereas sample Van C reveals Cp peaks at 690 and 735 °C (Fig. 4.4 a). In contrast, sample Van A2, which contain a minor amount of glass, did not produce a clear Cp peak.

sample	SiO <sub>2</sub>	TiO <sub>2</sub>	Al <sub>2</sub> O <sub>3</sub>	Fe <sub>2</sub> O <sub>3</sub>	MnO	MgO	CaO	Na <sub>2</sub> O	P <sub>2</sub> O <sub>5</sub>	K <sub>2</sub> O	Total
Van A1	55.52	0.72	18.17	8.30	0.15	2.88	7.60	3.86	0.40	2.51	99.95
Van A2	55.49	0.68	18.67	7.81	0.14	2.62	7.60	3.93	0.39	2.46	99.45
Van C	55.81	0.73	18.10	8.42	0.15	2.90	7.54	3.87	0.40	2.57	100.36

Table 4.1: XRF analysis of bulk rock compositions of all sampled eruptive products.

matrix	SiO <sub>2</sub>	TiO <sub>2</sub>	Al <sub>2</sub> O <sub>3</sub>	FeO	MnO	MgO	CaO	Na <sub>2</sub> O	P <sub>2</sub> O <sub>5</sub>	K <sub>2</sub> O	Cr <sub>2</sub> O <sub>3</sub>	Total
sideromelane (mean)	60.85	0.96	14.98	7.64	0.19	2.01	4.76	3.81	0.74	4.07	0.00	100.00
Std. dev. (N = 79)	2.01	0.11	0.87	1.52	0.10	0.89	1.33	0.51	0.20	0.80	0.10	0.00
microlite-rich (mean)	59.58	0.95	14.74	8.44	0.20	2.64	5.62	3.46	0.61	3.76	0.00	100.00
Std. dev. (N = 44)	1.85	0.19	1.46	1.68	0.09	1.10	1.87	0.48	0.16	0.97	0.12	0.00

Table 4.2: Microprobe analysis results of sideromelane (glassy) and microlite-rich groundmass. N gives the number of measurements. Given are mean and standard deviation.

## 4.5 Shallow magma mixing

---

The general bimodality of crystallinity and vesicularity of the eruptive products may indicate magma mingling, although localized second boiling may also promote such features (e.g., [Westrich \*et al.\*, 1988](#)) yet, the overall similarity in glass chemistry, despite a range in crystallinities, and the occurrence of a wide Cp plateau containing a double peak poses a geochemical paradox. A glass usually displays a sharp Cp peak at the glass transition, because a small volume of sample (e.g., a few  $mm^3$ ) is generally chemically homogeneous and it is expected to cool at a relatively constant rate, locking in a certain structural state. Chemically, the glass phase inside the sideromelane- and microlite-rich areas appears identical and volatile-free. The postulated double glass transition signature may result from the rheological influence of iron oxidation state ([Liebske \*et al.\*, 2003](#); [Bouhifd \*et al.\*, 2004](#)), if the oxidation states of magmas from different depths mingling with each other is variable. We tested this hypothesis through heat capacity measurements on crystal-free glasses with different oxidation states (made from remelted samples; see supplementary online information section), which showed distinct Cp peaks, with a temperature range comparable to that measured in samples Van A1 and Van C (Fig. 4.4 b). During repeated measurements on the reduced glass, a shift in the Tg peak to higher temperatures with the tendency to oxidize, as seen by wet chemistry measurements (Fig. 4.4 b), showed the relatively unstable nature of reduced basaltic glass, which thus prevent us from providing an accurate viscosity estimate at Tg (e.g., [Gottsmann and Dingwell, 2000](#)). It can however be inferred that the highly oxidized interstitial melt in sample Van A was more viscous than that in sample Van C. Rheologically, the comparison between glasses with different oxidation states and natural heterogeneous samples suggests that mingling indeed took place and most likely occurred over a very short period of time (seconds to a few minutes at the most) due to the unstable nature of the glass transition of reduced samples. Such an interpretation is in agreement with mingling occurring in the shallow parts of the conduit at the point where rapidly ascending magma interacts with shallow crystallized magma or recycled rocks (slumped from the crater into the conduit) shortly before being erupted. The residence of partially crystallized magma in the shallow reservoir would provide the time for the oxidation of an otherwise relatively reduced magma ascending from depth. Our observation of contrasting eruption recurrence timescales at the different vents therefore provides a measure of the oxidation level reached by the shallow magma. In our thermal analysis of the heat capacity, many samples were analyzed; yet, all samples from crater C, which produced strong Strombolian eruption at a periodicity of  $\sim 10$  minutes, were characterized by broad Cp plateau with double peaks at the lower end of the plateau. On the other hand the eruptive products from Crater A, which were produced by frequent, but weaker eruptions, were characterized by very contrasting double glass transition peaks.

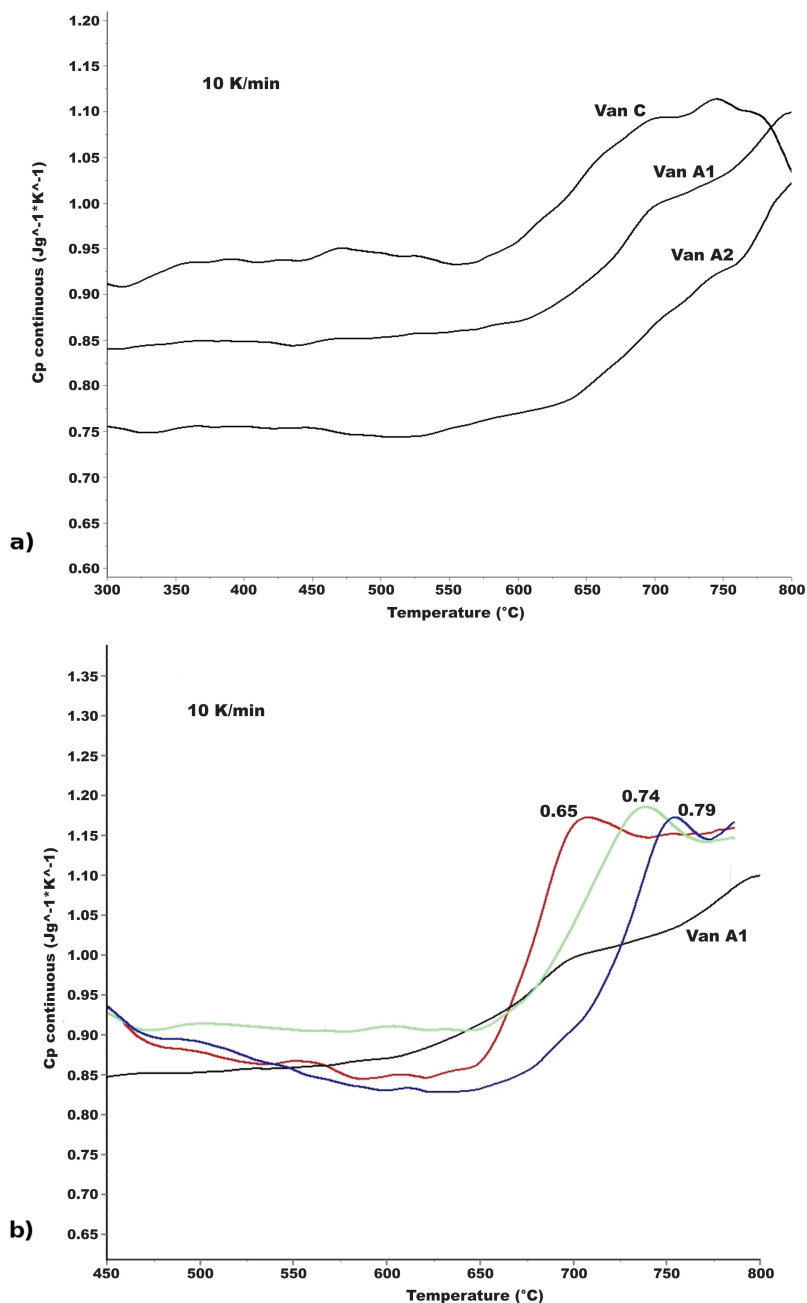


Figure 4.4: a) Results of DSC experiments for the three samples. Sample Van A1 shows two distinct Tg peaks at 690 and 780 °C, sample Van C a broad plateau ranging from 600 to 780 °C and no distinct peak can be seen in the results of sample Van A2. b) Results of DSC experiments on natural (black, sample Van A1), oxidized (blue), reduced (red) and partially reoxidized (green) samples. The natural sample shows two TG peaks, the peaks of reduced and oxidized samples vary by 60 °C, whereas the partially reoxidized sample lies in between. The numbers above the curves give the measured  $\text{Fe}^{3+}/\text{Fe}^{\text{tot}}$  ratio. All curves are done using 10° cooling and heating rate. All results are shown in the same amplitude range.

This heat capacity signature distinction between eruptive products results from mingling at different recurrence timescales, which may reflect the energy driving these eruptions as well as the importance of residence time at shallow depths, as this likely dictates the crystallinity of the magma and its degree of oxidation. In essence, the frequent recurrence of weak and short events may favor longer residency of most of the shallow magma thereby inducing

crystallization as well as the oxidation of iron, which would increase the range of oxidation states locked in at the glass transition and broaden the temperature range of the Cp plateau. In contrast, less frequent and stronger events may incorporate a larger volume of more shallow material thereby shortening the overall residency of magma in the shallow conduit which would minimize the presence of iron in the oxidized trivalent state and thus favor Cp peaks at the reduced end of the Cp spectrum. The picture illustrated by the combined rheological, petrological and geochemical analyses present the complex, but rapid interplay of multiple magmas during eruptions.

## 4.6 Conclusion

---

Strombolian eruptive products at Mt. Yasur were petrographically, geochemically and rheologically characterized to constrain the occurrence of magma mingling in the shallow magma conduit. The tephra are basaltic-andesite, which show regions with contrasting crystallinity and bubble-size distributions. Thermal analysis of these juvenile products revealed the presence of a glass phase exhibiting a broad heat capacity plateau between 650 and 800 °C, further typified by double glass transition peaks. The multiple peaks can be explained by the bimodal oxidation state of iron in an otherwise, chemically homogeneous magma. This nature of the measured glass transitions is used to infer that mingling is rapid and thus accommodated in the shallow parts of eruptive conduits, perhaps due to rejuvenation of material slumped from the crater walls into an open conduit system.

## 4.7 Methods

---

Samples erupted from different eruptive vents were petrographically described and the bubble size distribution was analyzed according to the method by [Sahagian and Proussevitch \(1998\)](#). The geochemical composition of the bulk rock as well as the interstitial glass was measured via X-ray fluorescence and an electron probe micro-analyzer as well as wet chemistry. The rheological character of the interstitial glass was determined using thermal analysis, namely: thermogravimetric measurements to assess the volatile content of the material and differential scanning calorimetric measurements to assess the temperature at which interstitial glasses undergo the glass transition. For further information see the online supplementary information section.

---

## 4.8 Appendix

---

### 4.8.1 Samples collected at Mt. Yasur

During our field campaign in August and September 2008, samples from three erupted bombs were collected on the basis of their morphological characteristics upon impact as well as their vent origin (Fig. 4.5).

### 4.8.2 Bubble size distribution

A series of transmitted light microphotographs were taken under a zoom of 2.5x and stitched to retrieve a large mosaic of crystal-rich and sideromelane areas. These mosaics were then converted to binary images (i.e., groundmass and vesicles). The vesicle sizes were analyzed using the JMicroVision software (Nicolas, 2009) and the distribution was binned according to the  $10^{-0.1}$  geometric scale suggested by Sahagian and Proussevitch (1998).

### 4.8.3 Bulk rock chemistry

The bulk rock chemistry (major elements) of the samples were carried at the Service d'Analyse des Roches et des Minéraux (SARM) in Nancy via Inductively Coupled Plasma Optical Emission Spectrometry (ICP-OES) technique. Detailed methods and uncertainties can be found in Carignan *et al.* (2001). The samples were finely powdered (300mg) and fused in Pt crucibles along with 900 mg of ultra-pure LiBO<sub>2</sub> at 980 C in an automatic tunnel oven. Samples were passed through the oven on a rail over a period of about 60 minutes at a constant speed. This method ensured that all the samples encountered the same thermal gradient. A blank (900 mg LiBO<sub>2</sub>) and five international reference materials of different compositions were prepared with the batches of samples. The reference materials were: (1) alkali basalt BR, (2) anorthosite AN-G, (3) serpentinite UB-N, (4) diorite DR-N and (5) granite GH [see Govindaraju (1995) for details].

### 4.8.4 Electron probe micro-analysis (EPMA)

Chemical composition analysis of the interstitial glass phase and of the crystals present in both the sideromelane and the microlite-rich groundmass was performed using a Cameca SX100 microprobe in the Department of Earth and Environmental Sciences at the University of Munich. The analysis was carried out using an accelerating voltage of 15 kV and a beam current of 5 nA. For measurements on the glass, the beam was defocused at a size of 5μm and measurements on crystals were performed with a focussed beam of 1μm. The measurements were calibrated for using the following standards: orthoclase for *Al*, *Si*, *K*; ilmenite for *Ti*, *Mn*; Periclase for *Fe*, *Fe<sub>2</sub>O<sub>3</sub>*; *Mg*; wollastonite for *Ca*; apatite for *P*; and Chromite for *Cr*.



Figure 4.5: Photograph of the three samples at their point of deposition . *Top:* Sample Van A1; *Middle:* Sample Van C; *Bottom:* Sample Van A2. Note the impact deformation of samples Van A1 and Van C, whereas sample Van A2 is undeformed.

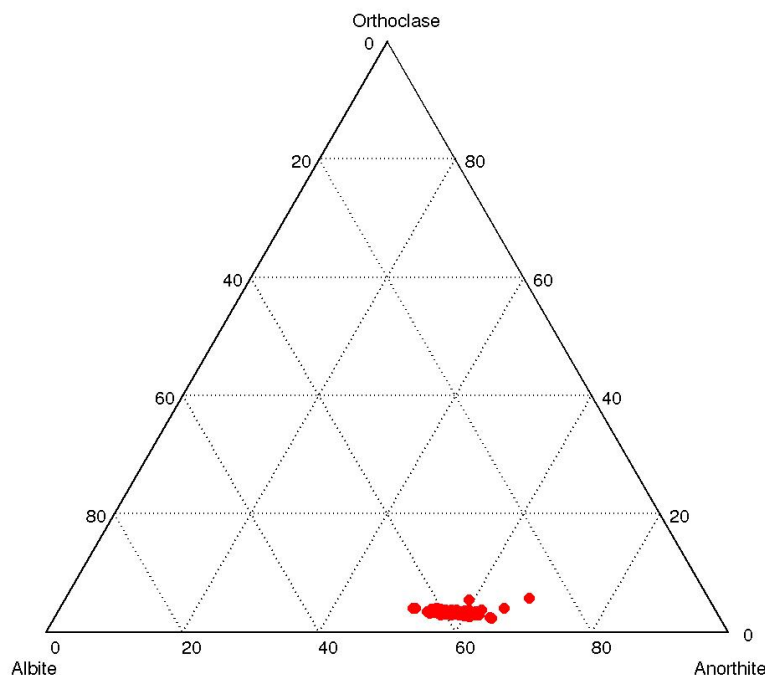


Figure 4.6: Ternary diagram of all single measurements on plagioclase using the electron microprobe.

In addition to the chemical analyses on the glass phase introduced in the paper, our analysis on plagioclase (307 data points) revealed a range of anorthite content from An50 to An70, that is in representative of a labradorite (Fig. 4.6).

#### 4.8.5 Thermogravimetric analysis

Thermogravimetric analyses were carried out using a Netzsch STA 449 C thermobalance equipment. 40 mg of sample chips were placed in a Pt crucible (covered by a lid) and heated to 1000 °C at a rate of 10 °C/min in a flowing Argon atmosphere. The measurements show no mass loss, which is used to infer the absence of residual water in the glass phase (Fig. 4.7).

#### 4.8.6 Differential scanning calorimetry

We performed differential scanning calorimetry experiments to characterize the rheological behavior of the samples in the glass transition range. For further interpretation of the results we added series of measurements on re-melted samples conditioned in oxidizing (air) and reducing ( $fO_2 = QFM - 2$ ) environments (see section 7). DSC measurements were carried out using a Setaram Sensys evo differential scanning calorimeter. 80 mg of sample chips were

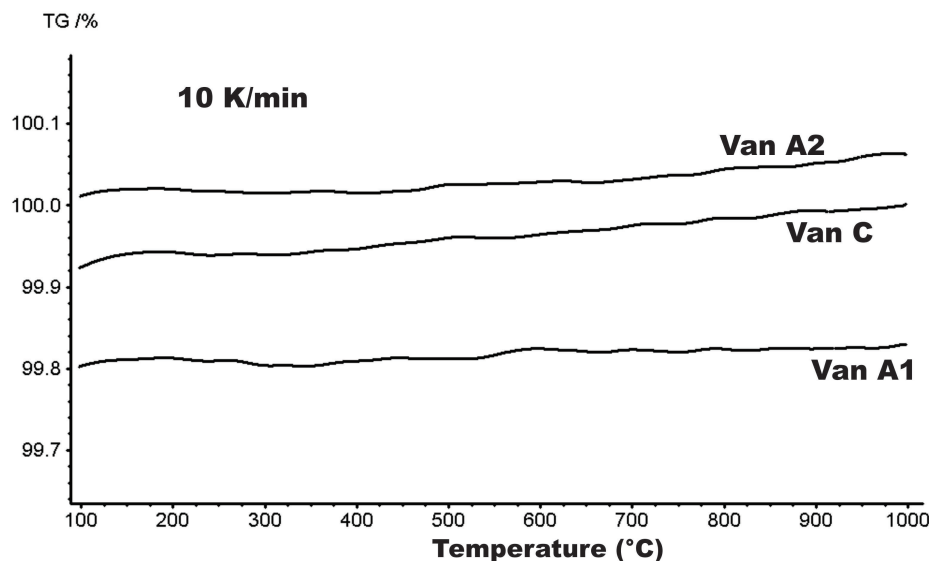


Figure 4.7: Thermogravimetric measurement of the three collected samples. The fluctuation in mass is in each case below the detection limit of the measurement, which is approximately  $\pm 0.1\%$ .

placed in a Pt crucible and heated to 800 °C at a cooling/heating rate of 10 °C /min in a flowing Argon atmosphere. The obtained peaks in heat capacity were used to determine the glass transition.

#### 4.8.7 Preparation of glass containing iron with different oxidation states

Glass samples with different oxidation states were prepared from remelted natural products. This was done to allow for the characterization of the rheological effects of iron oxidation states. Here, about 100 g of sample was crushed into powder and heated at super-liquidus temperature for 2h to allow melting of all crystals, degassing (if any) and homogenization of the liquid. The sample was quenched, crushed back to powder and the material was again melted following the above procedure to ensure the complete homogeneity of the melt. The second time, a spindle (connected to a rheometer) was introduced in the liquid and the viscosity was measured using the Couette technique developed for a concentric cylinder device as described by [Dingwell \(1989\)](#). The viscosity was essentially measured to track the process of chemical equilibration of the material. In practice, the rheometer's head (Brookfield model Rotary Variable Transducer Displacement) drives a spindle inserted in the liquid and digitally records the torque exerted by the liquid. The torque is converted into viscosity using a relationship between the read torque at a constant speed (40 to 0.5 rpm) and the viscosity defined by the calibration of a standard reference material (DGG1 from the Deutsche Glasindustrie). The accuracy in the viscosity determination was estimated at  $\pm 0.05 \log_{10}$  Pa s. The experiments were performed in a vertical tube Deltec furnace equipped with a gas-

mixing line ( $CO-CO_2$ ) (Dingwell and Virgo, 1987) to control the oxygen fugacity, monitored by a differential voltmeter linked to Pt-Pt90Rh10 sensors. To get two oxidation states, the melt was continuously stirred in air first and then under reduced condition (QFM-2) at 1300 °C during 24 hours. The melt was sampled by dipping an alumina rod into the melt to withdraw ca. 150 mg and then plunged in water to force quench without any reaction.

#### 4.8.8 Wet chemistry

A determination of the  $Fe^{3+}/Fe^{tot}$  ratio in the glass phase of the natural samples was not possible due to the thorough mingling of sideromelane and microlite-rich areas on a micro-scale. Therefore, our estimation of iron oxidation state was indirectly performed via the range of glass transition temperatures obtained from the natural samples compared against the glass transition temperatures obtained from remelted glass samples prepared under different oxygen fugacities. Here, we used wet chemistry to quantify the iron oxidation state related to the  $T_g$  obtained from glass formed under different oxygen fugacities. For the determination of the  $Fe^{2+}$  content in the remelted glass we used potassium dichromate titration. Therein, 15 mg of sample grinded to powder were placed in a polytetrafluoroethylene crucible and covered with a polytetrafluoroethylene lid. Deionized  $H_2O$  and a solution of concentrated  $H_2SO_4$ ,  $HF$  and dionized  $H_2O$  were added to the powder and left to simmer on a hot plate for 30 minutes under  $CO_2$  gas. Subsequently, the crucible was placed in an ice bath and the crucible walls were washed with deionized  $H_2O$  and a boric acid was added. A  $K_2Cr_2O_7$  titrant with concentration of about 1%  $N$  was prepared and placed in a 500 mL volumetric flask. The solution was then titrated with a standard potassium dichromate. Potential values were recorded automatically when the potential changes were within  $\pm 2$  mV/min. All potentiometric titrations were performed at 20 °C using a Metrohm Dosimat 665 automatic titrator with a 686 titroprocessor as the control unit. A detailed description of the technique can be found in [Giuli \*et al.\* \(2011\)](#). The gained values allow to calculate the  $Fe^{3+}/Fe^{tot}$  ratio in the samples, based on the  $Fetot$  concentrations obtained through EPMA.

## Motivation for Following Chapter

The characterisation of seismic sources with time-reversed wave fields is developing into a standard technique that has already been successful in numerous applications. While the time-reversal imaging of effective point sources is now well-understood, little work has been done to extend this technique to the study of finite rupture processes. The study presents a series of synthetic and real-data experiments that addresses questions concerning the quality of focussing in the source area, the localization of the fault plane, the estimation of the slip distribution and the source complexity up to which time-reversal imaging can be applied successfully. Recently, Lokmer *et al.* (2009) and O'Brien *et al.* (2010) presented studies on the time-reversal imaging at active volcanoes resolving a point source. As especially at Strombolian type volcanoes, the source is not expected to be point-localized this exhibits a strong limitation of the method. The following study on the time-reversal imaging of finite sources delivers valuable insights in the possibility to recover a time-variant source with the time-reversal imaging method.

# 5

## Time Reversal

### Exploring the potentials and limitations of the time-reversal imaging of finite seismic sources

*S. Kremers*<sup>1</sup>, *A. Fichtner*<sup>1,2</sup>, *G.B. Brietzke*<sup>1,4</sup>, *H. Igel*<sup>1</sup>, *C. Larmat*<sup>3</sup>,  
*L. Huang*<sup>3</sup>, *M. Käser*<sup>1</sup>

<sup>1</sup> Department of Earth and Environmental Sciences, Ludwig-Maximilians-University, Theresienstr. 41/III, 80333 Munich, Germany

<sup>2</sup> now at Faculty of Geosciences, Utrecht University, Utrecht, Netherlands

<sup>3</sup> EES-17 Geophysics Group, Los Alamos National Laboratory, Los Alamos, NM 87545, USA

<sup>4</sup> now at GFZ German Research Centre for Geosciences, Potsdam, Germany

published 2011 in *Solid Earth*: doi:10.5194/se-2-95-2011

#### 5.1 Abstract

---

The characterisation of seismic sources with time-reversed wave fields is developing into a standard technique that has already been successful in numerous applications. While the time-reversal imaging of effective point sources is now well-understood, little work has been done to extend this technique to the study of finite rupture processes. This is despite the

pronounced non-uniqueness in classic finite source inversions.

The need to better constrain the details of finite rupture processes motivates the series of synthetic and real-data time reversal experiments described in this paper. We address questions concerning the quality of focussing in the source area, the localisation of the fault plane, the estimation of the slip distribution and the source complexity up to which time-reversal imaging can be applied successfully. The frequency band for the synthetic experiments is chosen such that it is comparable to the band usually employed for finite source inversion. Contrary to our expectations, we find that time-reversal imaging is useful only for effective point sources, where it yields good estimates of both the source location and the origin time. In the case of finite sources, however, the time-reversed field does not provide meaningful characterisations of the fault location and the rupture process. This result cannot be improved sufficiently with the help of different imaging fields, realistic modifications of the receiver geometry or weights applied to the time-reversed sources.

The reasons for this failure are manifold. They include the choice of the frequency band, the incomplete recording of wave field information at the surface, the excitation of large-amplitude surface waves that deteriorate the depth resolution, the absence of a sink that should absorb energy radiated during the later stages of the rupture process, the invisibility of small slip and the neglect of prior information concerning the fault geometry, and the inherent smoothness of seismologically inferred Earth models that prevents the beneficial occurrence of strong multiple-scattering.

The condensed conclusion of our study is that the limitations of time-reversal imaging - at least in the frequency band considered here - start where the seismic source stops being effectively point-localised.

## 5.2 Introduction

---

Time reversal (TR) is a universal concept that can be found in numerous physical sciences, including meteorology (e.g. Talagrand and Courtier, 2007), geodynamics (e.g. Bunge *et al.*, 2003), ground water modelling (e.g. Sun, 1994) and seismology. The misfit  $\chi$  between observed and synthetic data is propagated backwards in time to detect the underlying discrepancies between the real world and its mathematical model. TR can be approached from two closely related directions: (1) the invariance of a non-dissipative physical system with respect to a sign change of the time variable, and (2) the computation of the gradient of  $\chi$  with the help of the adjoint method.

From a seismological perspective, the time-invariance of perfectly elastic wave propagation provides the intuitive justification for the TR imaging of seismic sources: Seismograms  $\mathbf{u}_0(\mathbf{x}^r, t)$  recorded at positions  $\mathbf{x}^r$  ( $r = 1, \dots, n$ ) are reversed in time, re-injected as sources at their respective receiver locations, and the resulting wave field  $\mathbf{u}(\mathbf{x}, t)$  is then propagated backwards in time through an appropriate Earth model. When the receiver configuration is sufficiently dense, the time-reversed wave field  $\mathbf{u}$  approximates the original wave field  $\mathbf{u}_0$ .

Focussing of  $\mathbf{u}$  then occurs at the time and location where  $\mathbf{u}$  was excited, thus providing information on the original earthquake source.

While being mathematically more rigorous, the adjoint method (e.g. [Tarantola, 1988](#); [Tromp \*et al.\*, 2004](#); [Fichtner \*et al.\*, 2006](#); [Fichtner, 2010](#)) leads to a similar result: The gradient of the misfit  $\chi$  with respect to the source parameters is given in terms of the time-reversed wave field generated by adjoint sources that radiate the misfit from the receiver positions back into the Earth model. In the case of a moment tensor point source, for instance, the derivative of  $\chi$  with respect to the moment tensor  $\mathbf{M}$  is given by

$$\frac{\partial \chi}{\partial M_{ij}} = - \int \epsilon_{ij}(\mathbf{x}^s, t) dt, \quad (5.1)$$

where  $\epsilon_{ij}$  and  $\mathbf{x}^s$  denote the strain tensor computed from the time-reverse field  $\mathbf{u}$  and the source position, respectively. In this sense, TR can be interpreted as the first step in an iterative gradient-based source inversion (e.g. [Tromp \*et al.\*, 2004](#); [Hjörleifsdóttir, 2007](#); [Fichtner, 2010](#)).

The history of TR imaging is likely to have started in ocean acoustics (e.g. [Parvulescu and Clay, 1965](#); [Derode \*et al.\*, 1995](#); [Edelmann \*et al.\*, 2002](#)), from where it migrated to medical imaging (e.g. [Fink, 1997](#); [Fink and Tanter, 2010](#)), non-destructive testing (e.g. [Chakraborty \*et al.\*, 1995](#); [Sutin \*et al.\*, 2004](#)) and many other fields. One of the earliest seismic applications can be found in the work of [McMechan \(1982\)](#) who introduced TR source imaging as a modified version of migration. The time-reversed wave equation is used to image earthquake sources instead of subsurface structures ([Artman \*et al.\*, 2010](#)). [Kennett \(1983\)](#) pinpointed the advantages of TR as early as 1983: (1) no prior interpretation of the time-series is needed and (2) the full elastic wave field is used to obtain the best image of the source. Early applications were limited to structurally simple or acoustic models (e.g. [McMechan \*et al.\*, 1985](#); [Rietbrock and Scherbaum, 1994](#); [Fink, 1996](#)), but recent advances in numerical modelling enabled applications in more complex scenarios with different types of seismic sources, including the classic double couple point source ([Gajewski and Tessmer, 2005](#)), extended faults ([Ishii \*et al.\*, 2005](#); [Larmat \*et al.\*, 2006](#); [Allmann and Shearer, 2007](#)), micro-seismic tremor ([Steiner \*et al.\*, 2008](#)) and volcanic long-period events ([O'Brien \*et al.\*, 2011](#)). [Larmat \*et al.\* \(2009\)](#) demonstrate the need to use specific imaging fields such as divergence or strain to distinguish sources from low velocity zones.

While TR imaging of effective point sources is now well-understood, little has been done to explore its potential to detect the details of finite rupture processes. This is surprising because classical finite-source inversions (e.g. [Cotton and Campillo, 1995](#); [Cesca \*et al.\*, 2010](#)) are known to be highly non-unique ([Mai \*et al.\*, 2007](#)). The urgent need to improve finite-source inversions motivates this study where we attempt to answer several key questions with the help of both synthetic and real-data experiments: (1) How well does the time-reversed field focus in the source area? (2) Does TR imaging provide constraints on the source volume? (3) Can regions with large slip (asperities) be identified? (4) Can the rupture speed be esti-

mated? (5) Up to which level of complexity does TR imaging provide useful information on the rupture process?

This paper is organised as follows: In a first series of synthetic tests we study TR imaging of single and multiple point sources under nearly ideal conditions. We then extend our experiments to synthetic data computed from a finite-rupture model. To improve the focussing of the time-reversed field, we investigate the influence of the station configuration and the weighting of the adjoint sources. Finally, we provide an application to the strong-motion data recorded during the 2000 Tottori (Japan) earthquake.

### 5.3 Numerical method

For our TR experiments we employ a spectral-element algorithm to model wave propagation in 3D elastic media (Fichtner and Igel, 2008; Fichtner *et al.*, 2009b,a). The model volume is divided into equal-sized hexahedral elements, and Perfectly Matched Layers (PML) are used to avoid reflections from the unphysical model boundaries. In the interest of simplicity, we restrict ourselves to isotropic and non-dissipative media.

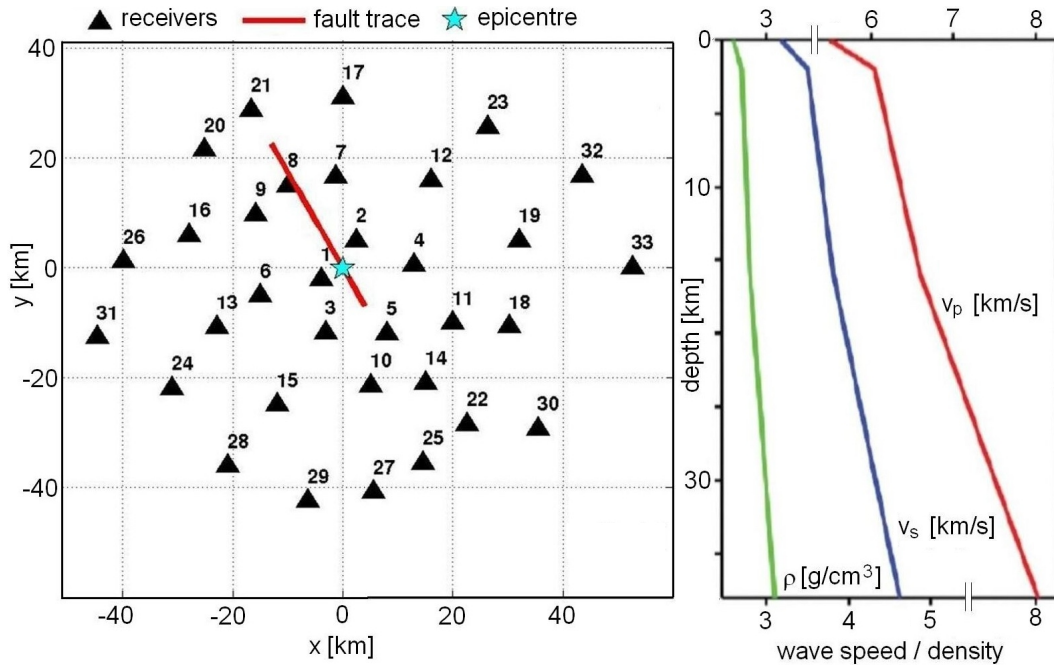


Figure 5.1: **Left:** Geographic model setup. Stations are marked by triangles. The red line and the star mark the fault trace and the epicentre for the finite-fault simulations in section 5.5. **Right:** Velocity and density model used in all synthetic simulations.

The model used in our synthetic tests is  $160 \times 170 \times 40$  km wide. It comprises  $60 \times 60 \times 16$  elements, which corresponds to  $\sim 3$  million grid points when the polynomial degree is 4. This setup allows us to model wave fields with frequencies up to 2 Hz. Both the receiver configuration (figure 5.1, left) and the structural model (figure 5.1, right) in most of our simulations are the same as in the SPICE source inversion benchmark (Mai *et al.*, 2007) that was intended to mimic the circumstances of the 2000 Tottori (Japan) earthquake. For the real data experiment we use the Japanese KiK-net stations (figure 5.11) and the layered velocity model of Semmane (2005). As we intend to work in the frequency range of kinematic source inversions ( $f = 0.1 - 1$  Hz) the velocity models were chosen alike. Even if the models seem dramatically smooth for time-reversal purposes, we argue that no unknown complexity should be added.

To generate the time-reversed wave field, the displacement is recorded at the surface receivers, flipped in time and then re-injected as three-component adjoint sources. For the propagation of the reverse field we use the same algorithm, setup and velocity model as for the forward simulation.

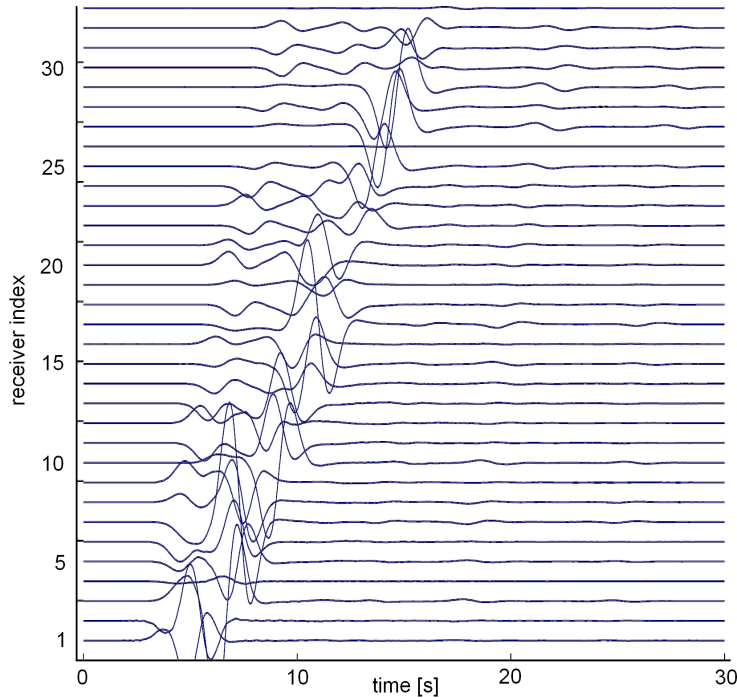


Figure 5.2: N-S-component synthetic seismograms recorded at the 33 stations for a moment tensor point source with only  $M_{xy} \neq 0$ . The stations are sorted by distance to the epicentre, and the traces are scaled to the maximum amplitude.

## 5.4 Synthetic points source simulations

### 5.4.1 Single point source

Our first series of tests with one single double couple point source is deliberately simplistic. It is intended to serve as a reference for TR under near-ideal conditions. The TR method should be able to recover the point source, because otherwise there would be little hope for success in finite-source imaging.

The moment tensor point-source, with only  $M_{xy}$  different from zero, is at 12.5 km depth. As source time function we use a Gaussian wavelet with a dominant frequency of 1 Hz. The wave field is computed for the 33 receivers shown in the left panel of figure 5.1. To illustrate the characteristics of the waveforms, a selection of N-S-component synthetic seismograms is shown in figure 5.2.

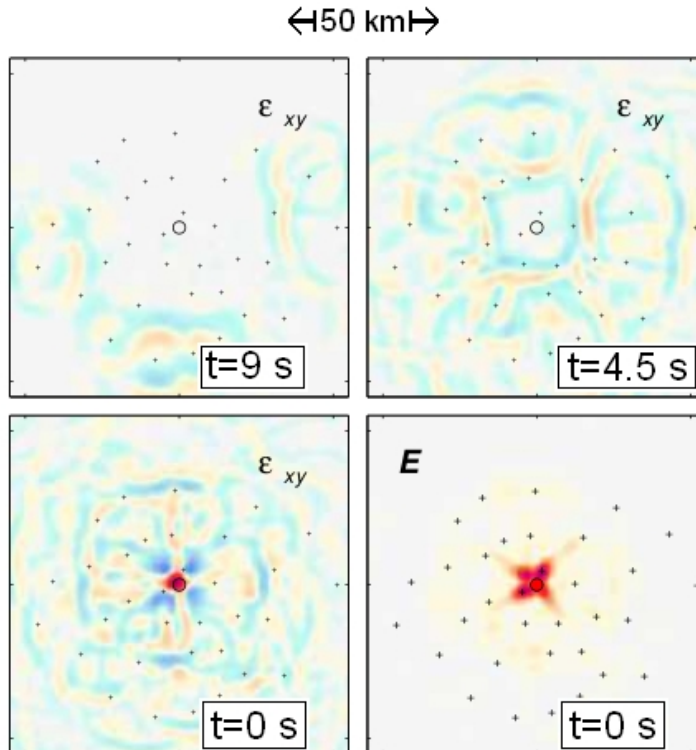


Figure 5.3: Snapshots at the point-source depth (12.5 km) of the time-reversed strain field  $\epsilon_{xy}$  at different times, and the energy  $\frac{1}{2}\mathbf{v}^2$  (lower right) at  $t = 0$ .

As suggested by equation 5.1, we monitor the time-reversed strain component  $\epsilon_{xy}$ . Snapshots of  $\epsilon_{xy}$  at different times are shown at the point-source depth (12.5 km) in figure 5.3. The adjoint field starts to propagate from the stations with the largest epicentral distance and then focusses at the hypocentre as  $t$  approaches 0. Weaker or no focussing was observed for the other components of the strain tensor, as expected. While the focusing of  $\epsilon_{xy}$  near the

source can clearly be observed,  $\epsilon_{xy}|_{t=0}$  is still significantly different from zero in other regions of the model volume that are distant from the source. These 'ghost waves' result from the imperfect reconstruction of the forward wave field by a finite number of irregularly spaced adjoint sources located at the surface. Depending on the particular setup, ghost waves may dominate the reverse field, thus masking the focussing at the source location. The influence of ghost waves can be reduced by using, for instance, the energy  $E = \frac{1}{2}\mathbf{v}^2$  to image the source (figure 5.3, lower right). This leads to the suppression of contributions far from the source, but also to a less optimal focussing directly at the source location. In numerous experiments a similar trade-off could be observed for other functionals of the time-reversed field, including the different components of the rotation vector  $\nabla \times \mathbf{u}$  and the rotation energy  $\frac{1}{2}(\nabla \times \mathbf{u})^2$ . This suggests that time-reversal imaging always involves a compromise between the focussing at the source and the suppression of ghost waves.

Our test with a point source moment tensor demonstrates that focussing in space and time can indeed be observed, at least under the previously described circumstances. This result motivates the study of more complex scenarios. In the following we focus our attention on the  $xy$ -component of the time-reversed strain field,  $\epsilon_{xy}$ . This restriction effectively corresponds to the injection of the prior information that the displacement on the infinitesimal or finite faults is a pure strike-slip.

### 5.4.2 Multiple point sources

Based on the encouraging results from the previous section, we add complexity to the source model and now consider three double couple point sources (only  $M_{xy} \neq 0$ ) that are positioned along the fault of the SPICE Tottori benchmark (figure 5.1, left). The point sources have different initiation times that correspond to a hypothetical rupture velocity of 2 km/s along the fault. The objective of this test is to reveal whether each of the three point sources can be resolved individually in both time and space.

Snapshots of the  $xy$ -component reverse strain,  $\epsilon_{xy}$ , are shown in figure 5.4. Circles mark the point source locations. Moving from the upper left to the lower right corner, we observe focusing at each of the three source locations around their respective initiation times of 16.9 s, 4.1 s and 0.0 s, with an uncertainty of  $\sim 1$  s. The width of the regions where focussing can be observed is  $\sim 5$  km, which is close to the wavelength of the surface waves ( $\sim 3$  km). From this we infer that the observed hypothetical rupture velocity is  $2 \pm 0.3$  km/s. We have thus obtained a first, and probably optimistic, estimate of the achievable space-time resolution in the subsequent finite-source imaging experiments.

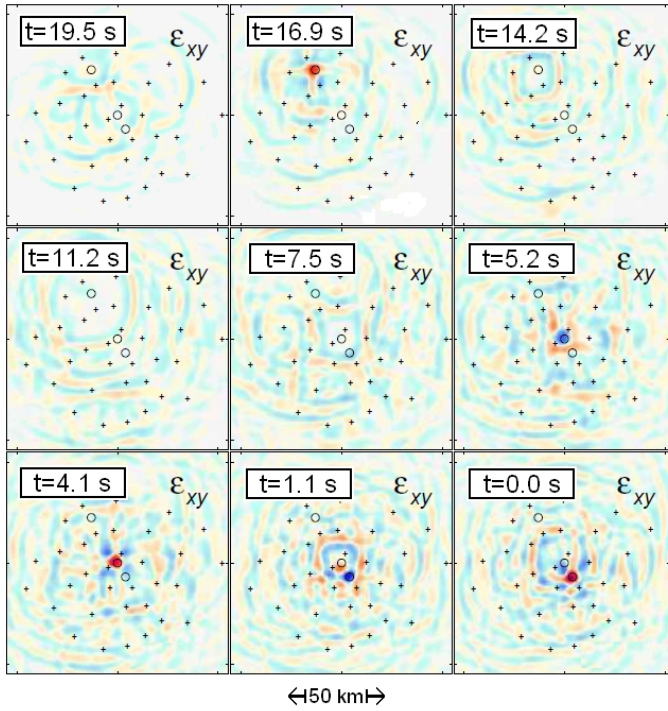


Figure 5.4: Snapshots of the time-reversed strain field  $\epsilon_{xy}$  at 12.5 km depth. Receiver and source locations are indicated by + and o, respectively. Focusing at all three source locations can be observed with an uncertainty of  $\sim 5$  km in space and  $\sim 1$  s in time. The observed hypothetical rupture velocity is  $2 \pm 0.3$  km/s, compared to 2 km/s used to generate the forward wave field.

### 5.4.3 Quantitative assessment of focussing for point sources

So far, a purely visual analysis of the time-reversed wave fields was sufficient to observe focussing. However, in anticipation of more complex finite-source scenarios, we examine the usefulness of a more quantitative criterion for the focal time within a pre-defined test volume: Starting with the point source simulations we determine the quantity  $S_V = \int_V \epsilon_{xy}^2 d^3\mathbf{x}$  within a test volume  $V$  around the source locations, and then consider the time when the maximum occurs as an estimate of the focal time. Since the wavelengths range between 4 and 20 km, we let  $V$  extend 10 km in all directions around the hypocentre location. As we seek a quantitative comparison of the focussing for various setups, we normalise  $S_V$  by  $S_\otimes = \int_\otimes \epsilon_{xy}^2 d^3\mathbf{x}$ , where  $\otimes$  denotes the remaining model volume outside  $V$ .

Figure 5.5 shows the normalised  $S_V$  for the single and multiple point source scenarios from sections 5.4.1 and 5.4.2, respectively. Distinct peaks at the expected source times are clearly visible in both cases. In the multiple point source experiment we observe that the peaks for the first two sources (at 0.0 s and 4.1 s) are comparatively low, probably due to their spatial proximity and overlapping test volumes. We conclude that the analysis of  $S_V$  is, at least for point sources, a useful diagnostic that allows us to estimate focal times and to compare the quality of focussing for different experimental setups.

Considering the multiple point source test successful, we now increase the complexity and make the transition to finite source models.

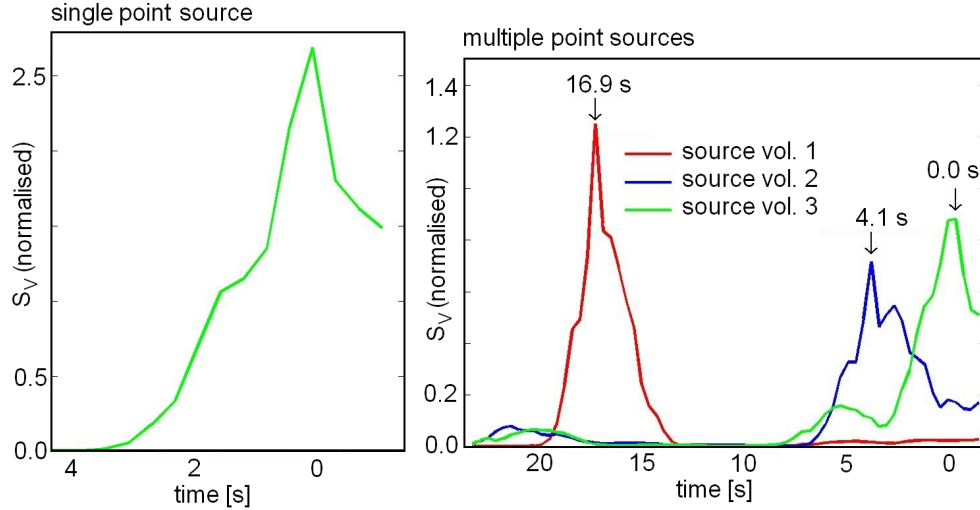


Figure 5.5: **Left:** Time evolution of the normalised  $S_V = \int_V \epsilon_{xy}^2 d^3\mathbf{x}$  for the single point source experiment from section 5.4.1. A pronounced peak occurs at the focal time  $t = 0.0$  s. **Right:** The same as to the left but for the multiple point source experiment from section 5.4.2. Peaks can be observed at the focal times of the different point sources.

## 5.5 Synthetic finite source simulations

The SPICE kinematic source inversion blind test offers the opportunity to analyse the performance of TR finite source imaging. The blind test mimics the 2000 Tottori (Japan) earthquake that was recorded by a large number of strong-motion sensors. Figure 5.1 (left) shows the receiver configuration, the fault trace and the epicentre location. Synthetic seismograms for the 33 receivers are part of the benchmark package. They were generated by pure strike slip motion, and with the slip and rupture time distributions shown in figure 5.6. The excited wave field has a maximum frequency of 3 Hz.

In an attempt to facilitate the visual identification of both the snapshots of the corresponding time-reversed strain component  $\epsilon_{xy}$  are shown in the top panel of figure 5.7. In reverse time, the rupture propagates in NW-SE direction. However, a clear focus restricted to the fault plane cannot be observed - in contrast to our expectation. The wave field remains diffuse, compared to the previous point source simulations. A robust inference concerning the hypocentre location and the initiation time is not possible.

In an attempt to facilitate the visual identification of both the fault and the rupture process, we analyse the cumulative squared strain  $S_T = \int_T \epsilon_{xy}^2 dt$ . Based on physical intuition one would expect  $S_T$  to be large only in those regions where significant strain occurs consistently over a longer period of time, i.e. along the fault. However, neither  $S_T$  directly on the fault plane nor  $S_T$  integrated over depth allow any meaningful inference concerning the location of the fault or the original slip distribution (see the bottom panels of figure 5.7). In fact,  $S_T$  is

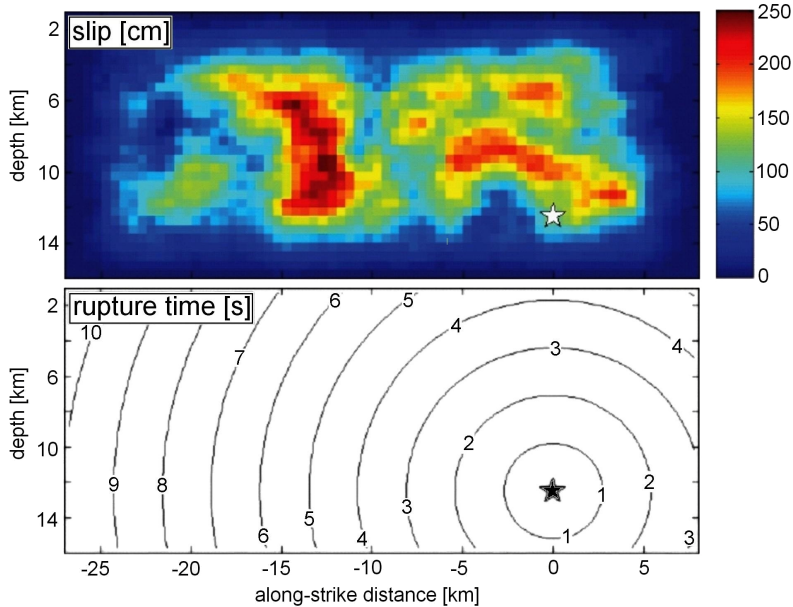


Figure 5.6: Synthetic slip (top) and rupture time (bottom) distributions of the SPICE Tottori benchmark (Mai *et al.*, 2007). Both the rupture speed and the rise time are constant at  $v_r = 2.7$  km/s and 0.8 s, respectively.

largest near the surface, which reflects the dominance of surface waves in the time-reversed wave field. Moreover,  $S_T$  on the fault plane reaches a local maximum where the original slip distribution (figure 5.6) is close to zero. The depth-integrated  $S_T$  is largest far off the fault trace.

Similar efforts to enhance the focussing on the fault by integrating, for instance,  $\epsilon_{xy}$  or  $\frac{1}{2}\mathbf{v}^2$  over time, did not lead to any significant improvements. We are therefore led to the early conclusion that no obvious functional of the time-reversed field allows us to identify the fault plane or the slip distribution unambiguously. In what follows we try to improve our results by (1) modifying the station distribution, and (2) weighting the adjoint sources.

### 5.5.1 Modifications of the station distribution

#### Dense regular grid of stations

The results from the previous section suggest that the number of stations and their spatial distribution provided insufficient information for the reconstruction of the original wave field. This motivates a synthetic test with a larger number of receivers (225 instead of 33) that are regularly spaced. While this scenario may be too optimistic in the near future, it provides valuable insight into TR finite source imaging under idealistic conditions.

For this experiment we computed synthetic seismograms with the help of a Discontinuous Galerkin method (Käser and Dumbser, 2006) that allows us to model the discontinuous displacement on the fault with high accuracy. Snapshots of the resulting time-reversed strain component  $\epsilon_{xy}$  are displayed in figure 5.8.

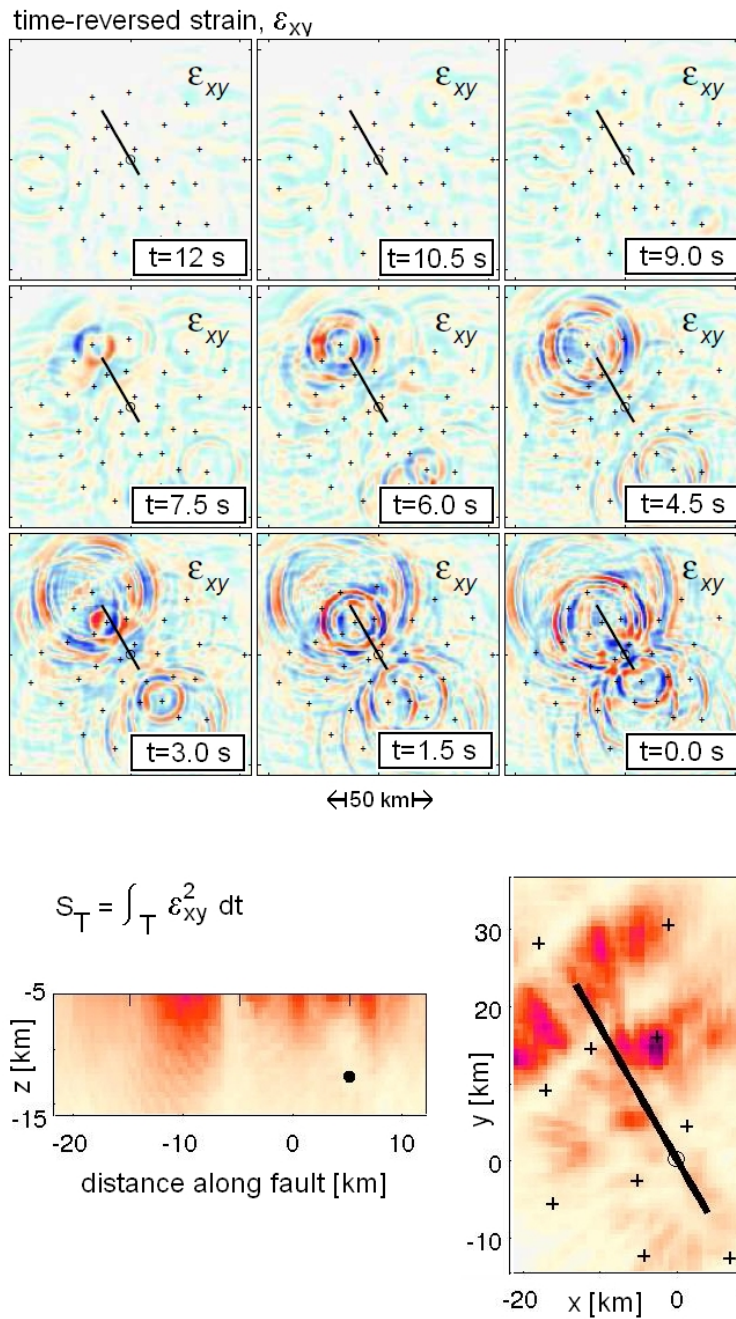


Figure 5.7: **Top:** Snapshots of the time-reversed strain component  $\epsilon_{xy}$  at 12.5 km depth. The fault trace is indicated by the black line. All snapshots are shown in the same amplitude range. **Bottom:** Cumulative squared strain  $S_T = \int_T \epsilon_{xy}^2 dt$  plotted on the fault plane (left) and integrated over depth (right).

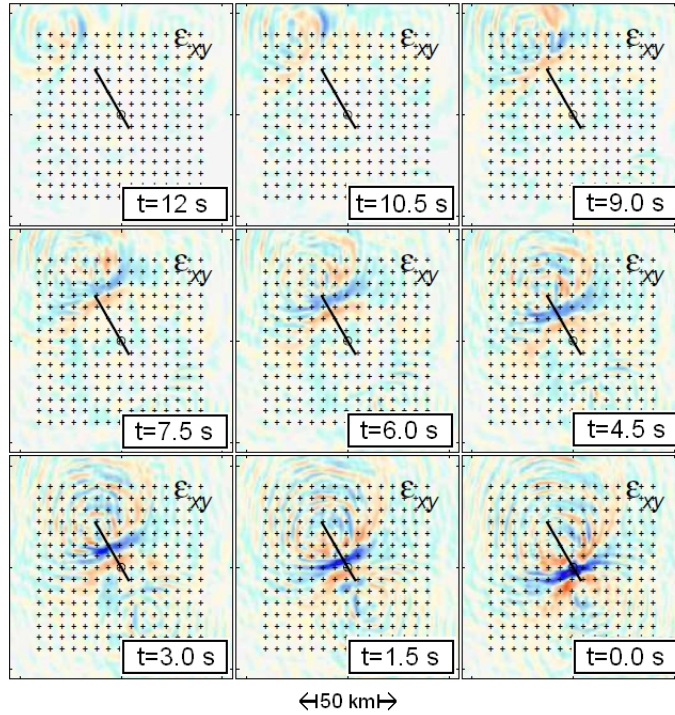


Figure 5.8: Snapshots of the time-reversed strain component  $\epsilon_{xy}$  at 12.5 km depth for the dense array of 225 regularly spaced receivers. The fault trace is indicated by the black line. All snapshots are shown in the same amplitude range.

Compared to figure 5.7 (original station distribution) we observe a sharper peak. Most of the energy propagates along the fault plane and in a direction that is consistent with the rupture time distribution (5.6, bottom). However, the focus is still elongated perpendicular to the fault, which complicates its unambiguous identification. Any inference on the details of the original slip distribution (figure 5.6) remains clearly impossible.

To obtain more useful results, we again explored a variety of functionals of the time-reversed field, including the time-integrated strain, the kinetic energy and the rotation amplitude. Neither of these functionals provided significant improvements, thus confirming our earlier conclusion that the overall quality of the focussing is rather independent of the field used for imaging.

### Station arrays

As an alternative to the previous densification of the receiver configuration we investigate the installation of several small sub-arrays that are composed of four stations that form a 2 km by 2 km quadrangle. This geometry is intended to have a beam-forming effect that hopefully improves the focussing of the time-reversed field.

The corresponding time-reversed strain field  $\epsilon_{xy}$  is shown in figure 5.9. The use of small sub-arrays clearly results in a more pronounced concentration of energy along the fault than with the original station setup (figures 5.1 and 5.7). However, the problem of unambiguously

identifying the fault itself remains unresolved also with this configuration. Again, the use of various functionals of the time-reversed field does not lead to significantly better results.

The previous experiments seem to imply that modifications of the receiver geometry are unlikely to improve the reconstruction of the original wave field to an extent that is sufficient to infer the slip distribution on the fault or even the fault itself.

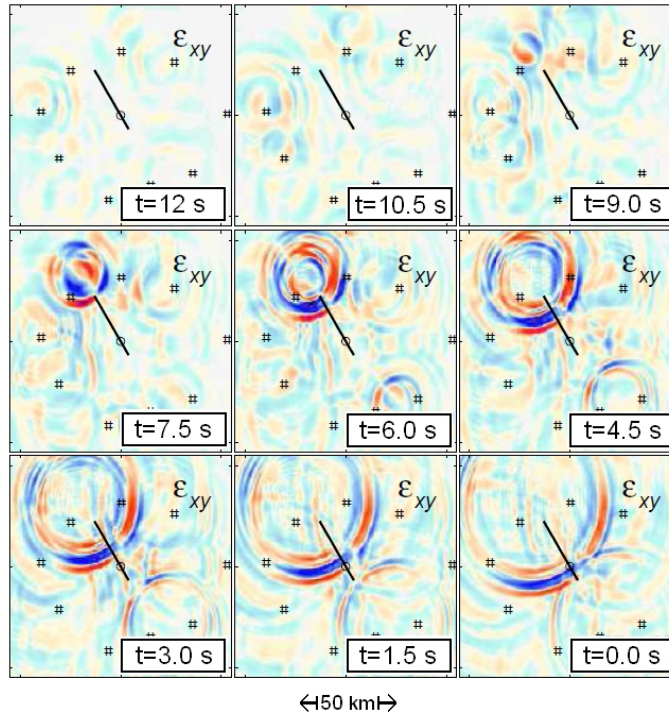


Figure 5.9: Snapshots of the time-reversed strain component  $\epsilon_{xy}$  at 12.5 km depth for the 9 sub-arrays composed of 4 receivers each. The fault trace is indicated by the black line. All snapshots are shown in the same amplitude range.

### 5.5.2 Weighting of adjoint sources

A visual analysis of this failure (see figures 5.7 and 5.9) reveals that the highly unequal contributions from different receivers may be part of the problem. While receivers close to fault dominate the time-reversed field due to the high amplitudes of the recorded waveforms, receivers at larger distances make only negligible contributions. This suggests that the reconstruction of the original wave field may be improved by assigning weights to the adjoint sources at position  $\mathbf{x}^r$  that compensate for the geometric amplitude reduction with increasing propagation distance. In the following we examine the effects of two different schemes where the weights are proportional to (1) the squared epicentral distance, and (2) the inverse energy of the recorded waveforms, i.e.  $2/\int \mathbf{v}(\mathbf{x}^r)^2 dt$ . It is important to note that the weighting scheme based on the distance from the epicentre corresponds to the incorporation of prior information that may not be available in applications where the epicentral coordinates are among the unknowns. Contrary to our expectations, the adjoint source weighting

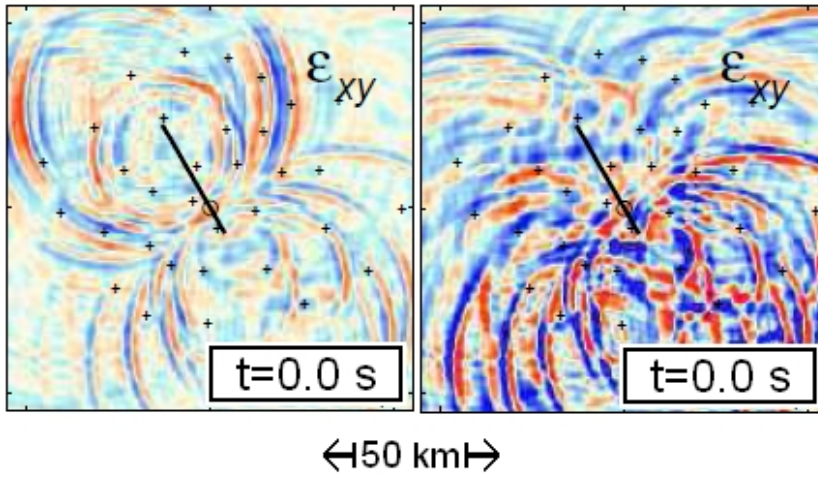


Figure 5.10: Snapshots of the time-reversed strain component  $\epsilon_{xy}$  at 12.5 km depth and  $t = 0$  for the weighted adjoint sources. **Left:** weight proportional to the squared epicentral distance. **Right:** weight proportional the inverse energy  $2/\int \mathbf{v}(\mathbf{x}^r)^2 dt$ .

deteriorates the focussing of the time-reversed strain field, as can be seen in figure 5.10. The negative effect is strongest for the inverse energy weight. In both cases, neither the details of the rupture process nor the fault trace can be inferred from the images.

## 5.6 Time-reverse imaging of the Tottori earthquake source

One of the original motivations for this study was to use time reversal imaging in order to reveal the rupture details of the 2000 Tottori (Japan) earthquake. However, following the negative results of our finite-source synthetic experiments, we are forced to revise our ambitious goals, and to limit ourselves to the detection of the epicentre and the focal time. For this real-data experiment we use 111 surface recordings from the Japanese KiK-net (figure 5.11, <http://www.kik.bosai.go.jp/>), band-pass filtered between 0.03 and 0.5 Hz which is similar to the frequency range commonly used in kinematic source inversions. The dominant wavelength of the surface wave-dominated field is around 20 km, which is close to the estimated fault length of  $\sim 30$  km (Semmane, 2005). We therefore expect to resolve only a point source. The amplitude at all adjoint sources was set equal to one to remove the strong influence of stations close to the source. For the time-reversed field wave propagation we use the layered Earth model described in Semmane (2005). All data processing was done using ObsPy, a newly developed python based toolbox for seismology (Beyreuther *et al.*, 2010).

Figure 5.12 shows the propagation of the time-reversed strain component  $\epsilon_{xy}$  from  $t = 30$  s to  $t = -30$  s. We observe clear focussing around the focal time and epicentre location as estimated by Semmane (2005). The uncertainty in time is  $\sim 3$  s, and the uncertainty in space is around 50 km, which is close to the dominant wavelength. The identification of

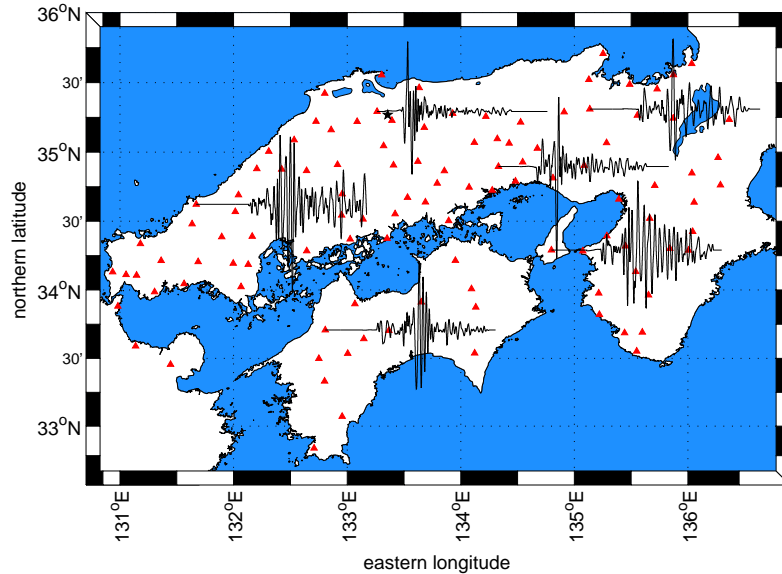


Figure 5.11: Source-receiver geometry of the real-data TR experiment for the 2000 Tottori earthquake. Red triangles mark the positions of the 111 stations used in the experiment, and the black star indicates the epicentre as inferred by Semmane (2005). The seismograms shown are vertical component velocities in the chosen frequency band.

the focal depth is not possible due to the comparatively long wavelengths and the presence of large-amplitude surface waves that mask the focussing of lower-amplitude body waves at greater depth. For negative times, i.e. prior to the initiation of the rupture, the time-reversed field propagates away from the epicentre, therefore attesting to the appropriateness of the structural model. A very similar focussing and defocussing could be observed for the other strain components and various functionals of the time-reversed field.

To obtain a more quantitative estimate of the focal time, we proceed as in section 5.4.3, where we computed the quantity  $S_V = \int_V \epsilon_{xy} d^3\mathbf{x}$  for a volume  $V$  surrounding the inferred point-source location. The time evolution of  $S_V$ , shown in figure 5.13, reveals a pronounced peak that serves as an estimate of the focal time. Our estimate positions the focal time at +3 s relative to the initiation time of the rupture as inferred by Semmane (2005). This discrepancy is likely to be related to the inferred location of the Tottori hypocentre within an area of small amount of final slip (e.g. Semmane, 2005; Piatanesi *et al.*, 2007). Taking the corresponding rise times into account, this may explain a weak detectability by means of TR for the hypocentral parameters of the Tottori event. The peak in figure 5.13 is therefore likely to approximate the rupture time of the first large-slip region, or the centroid time of the whole event (both at about +4 s, according to Semmane (2005) or Piatanesi *et al.* (2007) rather than the precise initiation time of the finite-size rupture.

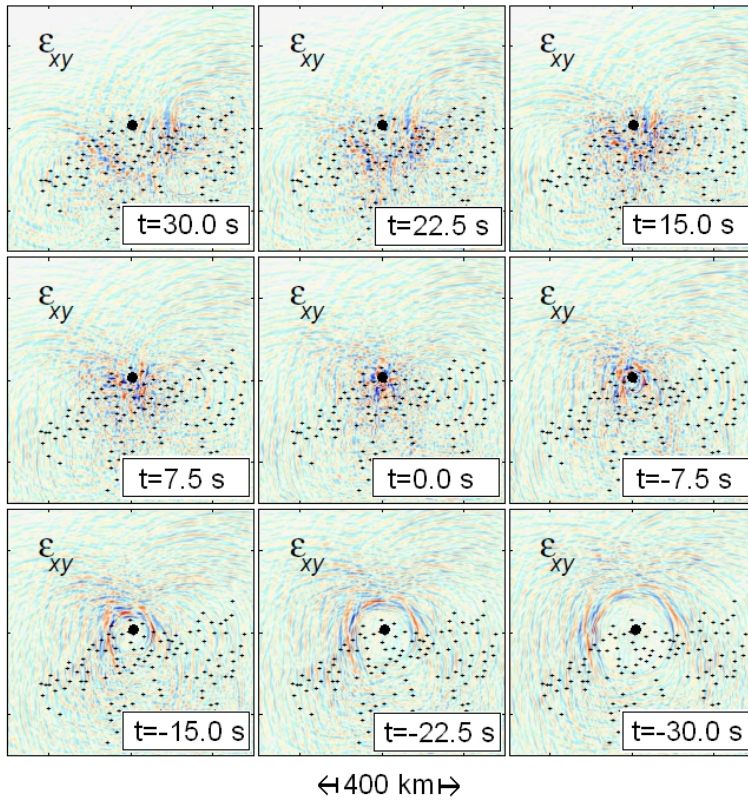


Figure 5.12: Snapshots of the time-reversed strain component  $\epsilon_{xy}$  at the surface for the Tottori data recorded at the 111 stations shown in figure 5.11. The coastlines are omitted to enhance the visibility of the time-reversed field. Estimates of both the focal time ( $t = 0$  s) and the epicentre location (black dot) are taken from Semmane (2005).

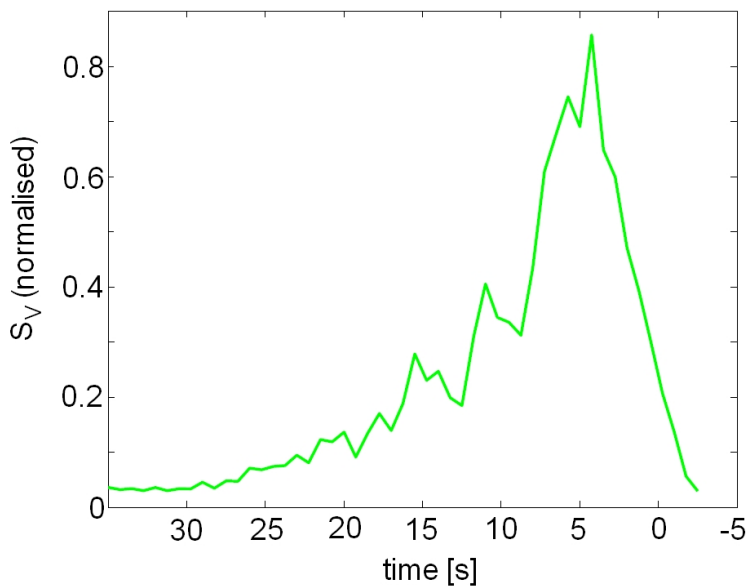


Figure 5.13: Time evolution of the normalised  $S_V = \int_V \epsilon_{xy}^2 d^3\mathbf{x}$  for a volume  $V$  that extends 20 km by 20 km around the epicentre as estimated from the time-reversal images from figure 5.12. The peak occurs at +3 s relative to the focal time estimated by Semmane (2005) ( $t = 0$ ).

## 5.7 Discussion

---

In the previous sections we explored the potentials and limitations of the TR imaging of seismic sources on regional scales. For this we studied a variety of scenarios with both synthetic and real data.

The potential of the method clearly lies in the estimation of the location and the timing of point sources. In a series of synthetic experiments we were able to observe the focussing of the time-reversed field in the vicinity of the original point source location and the original focal time. The uncertainties in the source location and time are governed by the frequency content and the receiver configuration. Our point source scenarios provide a proof of principle, but they are idealistic in the sense that we disregarded errors in the data and the assumed Earth model.

Our primary interest was in the detection of finite-rupture processes. Unfortunately, however, neither the rupture details nor the position of the fault itself could be inferred from the properties of the time-reversed wave field. To improve this result we analysed various functionals of the wave field (strain, energy, rotations), modified the receiver geometry (densification, sub-arrays) and applied weights to the adjoint sources in order to compensate for geometric spreading. None of these strategies can be considered successful.

The reasons for this failure are manifold: **(1) Incomplete information:** Firstly and most importantly, the information recorded at the surface is plainly insufficient to reconstruct the original wave field with an accuracy that allows for the unambiguous identification of the rupture process. For instance, the body wave energy radiated downwards is entirely disregarded. This distinguishes TR on regional scales from TR on global scales where information is lost only through dissipation. **(2) Large-amplitude surface waves:** Partly as a consequence of the previous item, the time-reversed field from stations that are distant from the fault is dominated by large-amplitude surface waves. The surface waves tend to mask the focussing of the lower-amplitude body waves that are primarily contributed by the stations closer to the fault. This effect results in a weak depth resolution, which means, in particular, that the focal depth can hardly be constrained. **(3) The missing sink:** An even more profound and general reason for failure is the incompleteness of the TR procedure. Our interest is in the seismic wave equation

$$\rho \ddot{\mathbf{u}}(\mathbf{x}, t) - \nabla \cdot \boldsymbol{\sigma}(\mathbf{x}, t) = \mathbf{f}(\mathbf{x}, t), \quad (5.2)$$

where  $\mathbf{u}$ ,  $\boldsymbol{\sigma}$  and  $\mathbf{f}$  denote the seismic displacement field, the stress tensor and an external force density. A complete time reversal of equation 5.2 would require the implementation of a sink  $\mathbf{f}(\mathbf{x}, -t)$  that acts as the counterpart of the source  $\mathbf{f}(\mathbf{x}, t)$  in the forward direction, and that absorbs elastic energy so that the time-reversed field is zero for  $t < 0$ . The sink, however, is disregarded simply because it is unknown. The missing sink poses a serious problem for finite-source inversions when fault segments are active at different times. The energy from segments that act late in the rupture process is not absorbed by the sink and therefore continues to propagate. The unabsorbed energy masks the focussing at the fault segments

that act early in the rupture process. The immediate implication is that TR for finite sources is always dominated by those fault segments with large slip near the end of the rupture time.

**(4) Invisibility of small slip:** A corollary of the previous item is that no information can be obtained about the rupture details on segments of the fault with small amount of final slip. This means, in particular, that the hypocentral parameters cannot be detected in those cases where the rupture initiation is associated with small slip. **(5) Lack of prior information:** The poor performance of TR finite-source imaging as compared to the classical kinematic source inversions is also due to the neglect of an apparently essential piece of prior information: The rupture occurs along a fault and is not diffusely distributed throughout the model volume. **(6) Incomplete knowledge of the 3D Earth structure:** While excluded a priori in the synthetic experiments, inaccurate Earth models can prevent focusing in real-data applications. The focusing observed in our experiment with Tottori data suggests that the model is sufficient to explain at least the arrival times of the direct waves. However, the absence of horizontal heterogeneities in the model does not allow for the correct back-propagation of scattered or even multiply-scattered waves. This issue is closely related to **(7) the insufficient complexity of 3D Earth models** that results either from the inherent smoothness of the Earth or the limited resolution of seismic tomography. The presence of strong multiple scattering is known to enhance focusing in laboratory experiments but cannot be exploited in seismology where the knowledge about sub-wavelength heterogeneities is too inaccurate.

## 5.8 Conclusions

---

The principal conclusions to be drawn from our work are as follows: (1) Time-reversal imaging is well-suited to infer both the location and the timing of point sources. (2) Time-reversal imaging in the used frequency range is not able to detect the details of finite rupture processes. Neither modifications of the receiver configuration (within reasonable bounds) nor the weighting of adjoint sources lead to sufficient improvements. (3) The dominant causes for this failure are the incomplete recording of wave field information at the surface, the presence of large-amplitude surface waves that deteriorate the depth resolution, the missing sink that should absorb energy radiated during the later stages of the rupture process, the invisibility of small slip and the neglect of prior information.

While our experiments are certainly not exhaustive, they nevertheless suggest that the limitations of TR imaging start where the source stops being point-localised.



## Motivation for Following Chapter

Consistently active volcanoes have always fascinated mankind (e.g., Stromboli, Italy). However, beyond the beauty of the eruption, our understanding of the mechanism driving the eruption is still incomplete. In general, Strombolian eruptions are agreed to be caused by the rise and burst of gas slugs, i.e. bubbles in the range of several meters in diameter that have decoupled from the melt phase, at the top of a magma column (e.g., [Blackburn \*et al.\*, 1976](#); [Seyfried, 1997](#); [Chouet, 2003](#); [Johnson, 2003](#); [James \*et al.\*, 2004](#)). The mechanism responsible for generation of these large gas pockets is still under debate, proposed models are a slug formation enhanced by structural barriers at depth that allow for a development of a foam layer ([Jaupart and Vergnolle, 1989](#); [Vergnolle and Jaupart, 1990](#); [Vergnolle, 1996](#)) or by inclined dipping feeder systems ([Chouet, 2003](#)).

Here we invert a multi-parameter geophysical dataset to constrain the location and source mechanism of Strombolian explosions at Mt. Yasur, Vanuatu. The used dataset consists of a combination of seismic, acoustic and Doppler-radar data. An estimate for the source volume is presented based on a combination of infrasound and maximum particle velocities. The previously applied time-reversal imaging method together with moment tensor inversion is used to constrain source location and mechanism. The results presented in the following chapter are the first of its kind for Mt. Yasur and will help to better understand the consistent active and potentially hazardous volcanic system.

# 6

## Source localization

### Inverting the Source Mechanism of Strombolian Explosions at Mt. Yasur, Vanuatu, using a Multi-Parameter Dataset

*S. Kremers<sup>1</sup>, J. Wassermann<sup>1</sup>, K. Meier<sup>2</sup>, C. Pelties<sup>1</sup>, M. van Driel<sup>3</sup>, J. Vasseur<sup>1</sup>, M. Hort<sup>2</sup>*

<sup>1</sup> Department of Earth and Environmental Sciences, Ludwig-Maximilians-University, Theresienstr. 41/III, 80333 Munich, Germany

<sup>2</sup> Institut f. Geophysik Uni Hamburg, Germany

<sup>3</sup> ETH Zurich, Institute of Geophysics, Zurich, Switzerland

submitted to *Journal of Volcanology and Geothermal Research*

#### **6.1 Abstract**

---

The source mechanism of Strombolian explosions at Mt. Yasur, Vanuatu, is analyzed. The novelty of the approach presented here lies in the combination of seismic, acoustic and Doppler-radar data. Using a combination of acoustic (infrasound) and Doppler Radar (maximum particle velocities), we are able to estimate the volume of the eruptive source. We show

a correlation exists between source volume and the maximum particle velocity. To determine both source location and mechanism we use the time reversal imaging method and moment tensor inversion. A seismic velocity model is introduced based on the wave speeds of direct waves and the results of frequency-wavenumber analyses of the installed small aperture arrays. We show that Time Reversal imaging can deliver an estimate of the source depth without any a priori assumptions even in an unfavourable scenario in terms of topography and receiver setup. The inverted source mechanism retrieved from moment tensor inversion is found to be largely isotropic, with minor deviatoric components. The inverted source location points to an area to the north-east of the active craters, representing a common feeder system of the activity at Mt. Yasur. The results presented here are the first of its kind for Mt. Yasur and will help to better understand the consistent active and potentially hazardous volcanic system, a major tourist attraction in the Vanuatu archipelago.

## 6.2 Introduction

---

Mt. Yasur is located on Tanna island, which is part of the subduction related volcanic island chain that forms the country of Vanuatu. The volcanic activity on Tanna island can be traced back as far as the late Pliocene undergoing a series of major volcanic episodes (Carney and Macfarlane, 1979; Chen *et al.*, 1995). The most recent episode formed the Siwi Group in the easternmost part of the island which is characterized by deposits that are predominantly basaltic to basaltic-andesitic in composition (Robin *et al.*, 1994; Allen, 2005; Bani and Lardy, 2007). Present activity in the Siwi Group is connected to the Mt. Yasur cinder cone, that rises approximately 361 m above sea level. It has three small active craters aligned in NE-SW direction (denoted as A, B and C from south to north) that are surrounded by a larger 400-m-diameter crater (Oppenheimer *et al.*, 2006). The three craters show varying styles of activity from ash-venting to strong Strombolian or Vulcanian activity (Carney and Macfarlane, 1979; Oppenheimer *et al.*, 2006; Bani and Lardy, 2007; Perrier *et al.*, 2011; Métrich *et al.*, 2011; Kremers *et al.*, 2012b) that now persists for at least 300 years (Simkin *et al.*, 1981).

In general, Strombolian eruptions are agreed to be caused by the rise and burst of large gas slugs, i.e. bubbles in the range of several meters in diameter that have decoupled from the melt phase, at the top of a magma column (e.g., Blackburn *et al.*, 1976; Seyfried, 1997; Chouet, 2003; Johnson, 2003; James *et al.*, 2004). The mechanism responsible for generation of these large gas pockets is still under debate, proposed models are a slug formation enhanced by structural barriers at depth that allow for a development of a foam layer (Jaupart and Vergnolle, 1989; Vergnolle and Jaupart, 1990; Vergnolle, 1996) or by inclined dipping feeder systems (Chouet, 2003). The rising gas slugs, that can easily reach lengths up to several tens of meters (e.g., Chouet *et al.*, 2003; Gerst, 2010) fill most of the conduit horizontally (Vergnolle, 1996; Seyfried and Freundt, 2000; Vergnolle *et al.*, 2004). Seismic signals that are believed to be generated by fluid mass transport (Chouet, 1994;

Ripepe and Gordeev, 1999; Konstantinou, 2002; O'Brien and Bean, 2008) have been observed amongst others at Stromboli (Italy) in the long to very-long-period (LP - VLP, 3 - 30 s, Neuberg *et al.*, 1994) and ultra-long-period (VLP, 100 - 1000 s, Dreier *et al.*, 1994; Wassermann, 1997; Kirchdörfer, 1999) range. Aster *et al.* (2003) demonstrated the excitation of a resonator as source of VLP events at Mt. Erebus (Antarctica). James *et al.* (2006) showed experimentally that the interaction of a rising slug with the conduit geometry can create pressure oscillations that are recorded as seismic signals in the VLP to LP range. Other authors attributed these signals more generally to resonance effects caused by pressure fluctuations in a fluid filled conduit (Ripepe, 1996; Chouet, 1996; Wassermann, 1997; Neuberg *et al.*, 2000; McNutt, 2005; Neuberg *et al.*, 2006; Bean *et al.*, 2008). As low-frequency signals at volcanoes often show highly emergent onsets, conventional approaches for localization based on first arrival picks can not be applied. Techniques that have amongst others been used to localize the source of LP and VLP events are beam-forming on diffraction hyperboloids (Wassermann, 1997), a waveform semblance method (Kawakatsu *et al.*, 2000), moment tensor inversion (e.g., Chouet *et al.*, 2003; O'Brien and Bean, 2008; Bean *et al.*, 2008) and time reversal (O'Brien *et al.*, 2011).

This study aims to enhance the understanding of Strombolian eruptions in general and in detail the generation, rise and burst of gas slugs at Mt. Yasur (Tanna, Vanuatu), which is besides Mt. Erebus (Antarctica) the only Strombolian-type volcano that allows a direct visual observation of the processes acting at the magma-air interface. We performed a multi-disciplinary field experiment combining seismic, acoustic and radar monitoring techniques. The combination of the monitored parameters allows us to define the slug rise time and length, correlate seismic amplitudes with particle velocities and recorded acoustic pressures and thus validate or falsify proposed models for Strombolian type activity. Furthermore, we generate a seismic velocity model of Mt. Yasur that is based on frequency-wavenumber analysis and the determination of the mean seismic wave speed through correlation of event onsets at radar and seismic (array) stations. Using this velocity model and the corresponding numerical mesh, we perform moment tensor (MT) inversion and time reversal (TR) simulations to locate the source of VLP signals ( $< 1$  Hz) that are observable prior to the manifestation of surface activity. For a stability test and the MT inversion on the Mt. Yasur data we computed Green's functions (GF) including a superficial low-velocity layer. Although this layer is small compared to the used wavelengths it can have a strong influence on the inverted source mechanism (Lokmer *et al.*, 2007; Bean *et al.*, 2008). MT inversion is performed in the Fourier domain using an algorithm developed by van Driel *et al.* (2012). The algorithm searches over a large grid of possible source positions, using a misfit criterion for the selection of the best source location. This technique represents the source as a point, i.e. the source extent is small compared to the used wavelength. Assuming that a rising slug in the conduit acts as source of the LP signal the source position will only be represented as a centroid. In contrast, TR is a promising approach to invert for an extended time-variant source. In doing so, we flip the recorded seismic signals in time and re-inject it in the model domain. For this purpose,

a high-order accurate Discontinuous Galerkin Finite element method (DGM) is used (Dumbser and Käser, 2006). The created seismic wavefield travels back in time and should in theory focus and the true source location in space and time. The use of two principally different inversion methods allows us to verify the found source parameters. Additionally, the combination with other measured geophysical parameters such as infrasound and using the of results from a petrological study (Kremers *et al.*, 2012b) allows us to further constrain the source characteristics of explosive Strombolian eruptions at Mt. Yasur volcano.

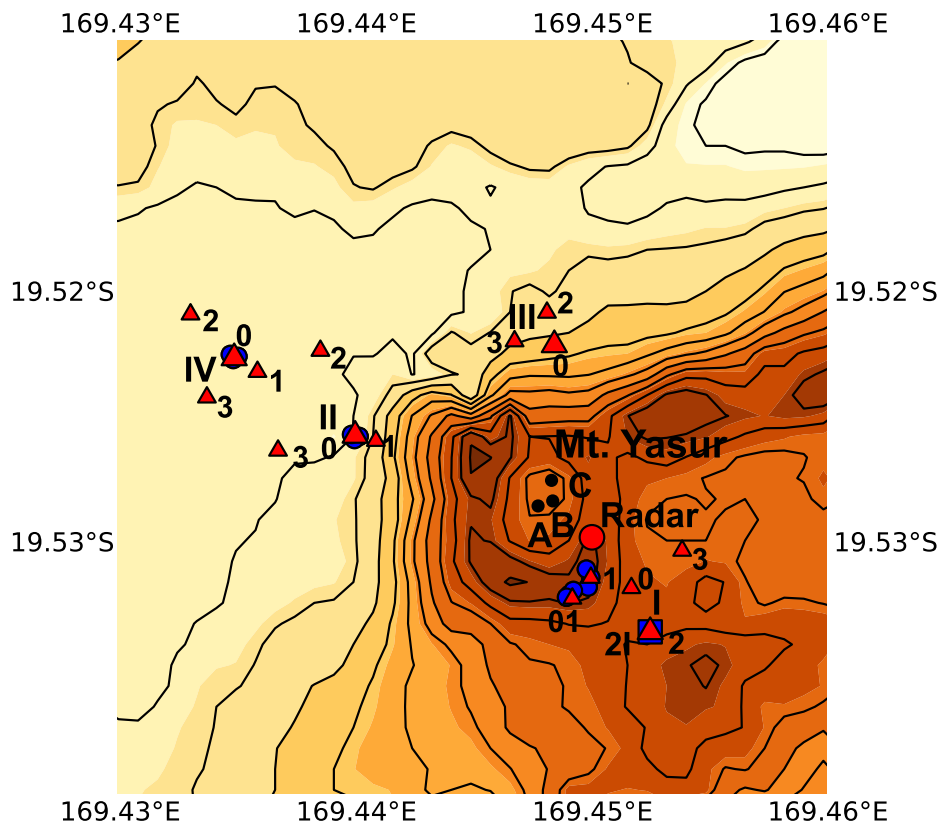


Figure 6.1: Station setup at Mt. Yasur. The red triangles give the location of the seismic arrays, called 'I', 'II', 'III', and 'IV'. Large red triangles are seismic broadband stations. The blue spheres show the installed short-period infrasound arrays, the large blue square the acoustic broadband station. The large red sphere gives the location of the Doppler-Radars, the infrared - and video camera. The three active craters are denoted as 'A', 'B' and 'C' from south to north, respectively.

## 6.3 Data

We installed four seismic small aperture arrays, each consisting of one Streckeisen STS2 broadband seismometer and two (array III) to four (array I) Mark L4C 1-s short period sensors (Fig. 6.1). The mean aperture of the arrays was around 300 m, the minimum distance between the stations around 100 m. Additionally, we deployed four band limited (0.05 - 5 Hz) infrasonic arrays (SensorTec) and one MB2005 (MATEC) broadband infrasound (0.01 - 20 Hz) receiver to record the acoustic pressure. The data was digitized with three- and six-component EarthDataLoggers (EDL), that continuously recorded the seismic and acoustic wavefield with 100 Hz sampling rate. The recordings at all stations were synchronized using GPS time signal. The velocity of ejecta exiting crater A (Fig. 6.1) and the corresponding temperatures were measured using two Doppler-Radars (METEK) and a TVS 700 infrared camera (GORATEC) (Meier *et al.*, 2009). Additionally, the erupted products of crater A and C were sampled for a complete petro-chemical characterization in

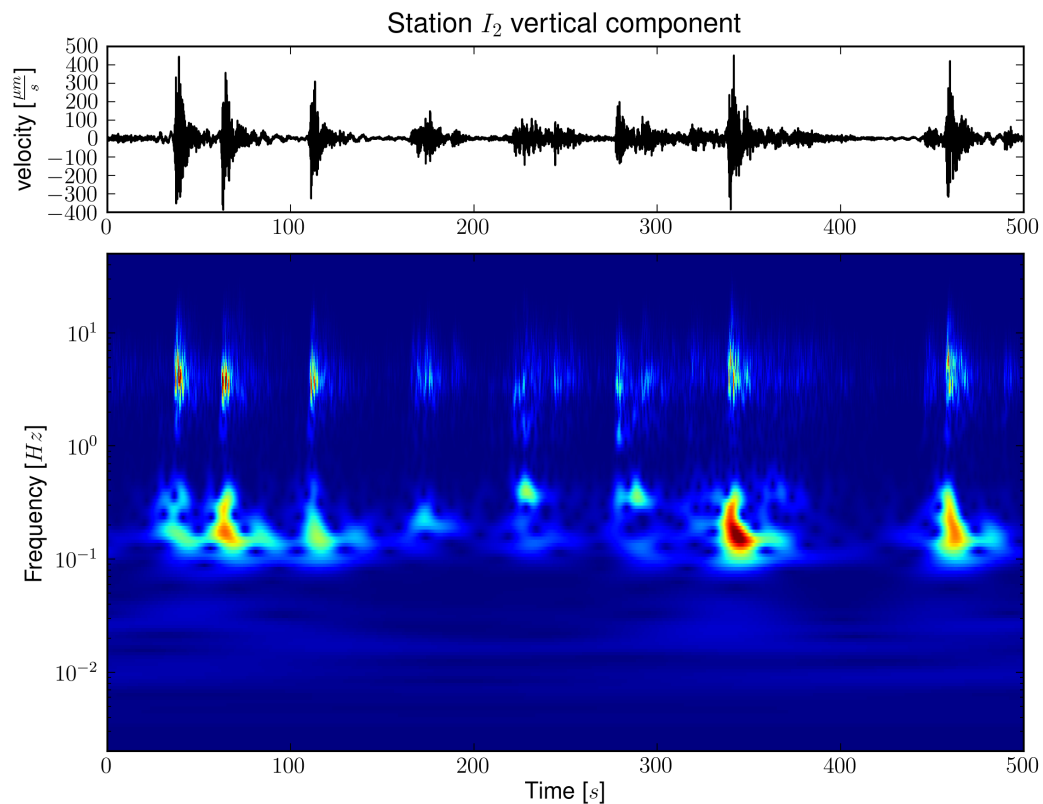


Figure 6.2: 500 second record of vertical component of velocity at seismic broadband station  $I_2$  and the continuous wavelet transform of the data using a morlet wavelet. Warm colors define high spectral amplitudes, cold colors lower amplitudes and background.

the lab. The results of this study are presented in [Kremers \*et al.\* \(2012b\)](#) and will be used here to constrain the source properties of Mt. Yasur.

During the time of the two week field campaign in August-September 2008, the three active craters showed very different styles of activity ([Fig. 6.1](#)). Crater A had an eruption recurrence time of under one minute. Crater B showed very irregular ash-venting, while crater C was producing strong eruptions every ten minutes. From the location of the Doppler radar a direct observation of the vent exit of crater A was possible. In the first days of the experiment, the surface of the lava column was visible, that afterwards retreated in the conduit. Our observations from video recordings and camera pictures suggest that the prevailing mechanisms acting at crater A are Strombolian bubble burst, and gas-jetting activity. A direct observation of crater C was prevented by the lower crater rim, however, the similarity in eruptive behavior and correlated signals in seismic and infrasound recordings point to highly similar mechanisms.

In total, we recorded over 20.000 explosive events at Mt. Yasur. In order to make this large dataset easily accessible we use the recently developed XML-based database SeisHub ([Barsch, 2009](#)). This web-based archive allows to store, process and share large, continuous datasets and the corresponding meta data, which makes it an ideal tool for geophysical multi-station experiments. The data are accessed and processed using ObsPy ([Beyreuther \*et al.\*, 2010](#); [Megies \*et al.\*, 2011](#)), a python toolbox for seismology.

As described above, Mt. Yasur's three active craters erupt frequently with highly varying recurrence rates. At the time of the field study, we observed an eruptive event roughly every minute. This high event number and the missing phases of quiescence in the seismic recordings result in an overlap of pre- and post-eruptive signals of different events ([Fig. 6.2](#)). Therefore, we aim to select only events of clear onset, a good signal-to-noise ratio (SNR) and that are clearly distinguishable from preceding and successive events in the used inversion techniques.

The spectrogram of the 500 s vertical component data of station  $I_2$  ([Fig. 6.2](#)) shows mainly energy in two distinct frequency bands: the long-period (LP) to very-long-period (VLP) band below 1 Hz and a high frequency band above 1 Hz. Correlation with Doppler-Radar measurements show that the high-frequency radiation is generated by the surface activity (bubble burst at the free surface; [Meier \*et al.\*, 2009](#)). In contrast, the VLP signal shows an onset before the surface activity which is interpreted as fluid movement or deformation buildup by the moving gas phase in the volcanic conduit.

During the experiments we observed two distinct eruption features at Mt. Yasur: eruptions that carried a high fraction of fine ash and events with virtually no fine-ash present ([Fig. 6.3](#)). The two types alternated on a daily to weekly bases. Seismic signals for ash-loaded events show significantly lower amplitudes in the HF band, whereas the VLP signals are unaffected ([Fig. 6.4](#)). Consequently, also the infrasound signals of events with a high ash-load have lower amplitudes (middle trace in [Fig. 6.5](#)) than the ash-free signals (upper trace in [Fig. 6.5](#)).



Figure 6.3: Strombolian eruptions at Mt. Yasur. *left*: Eruption that carries virtually no fine ash fraction; *right*: Eruption with high amount of fine ash.

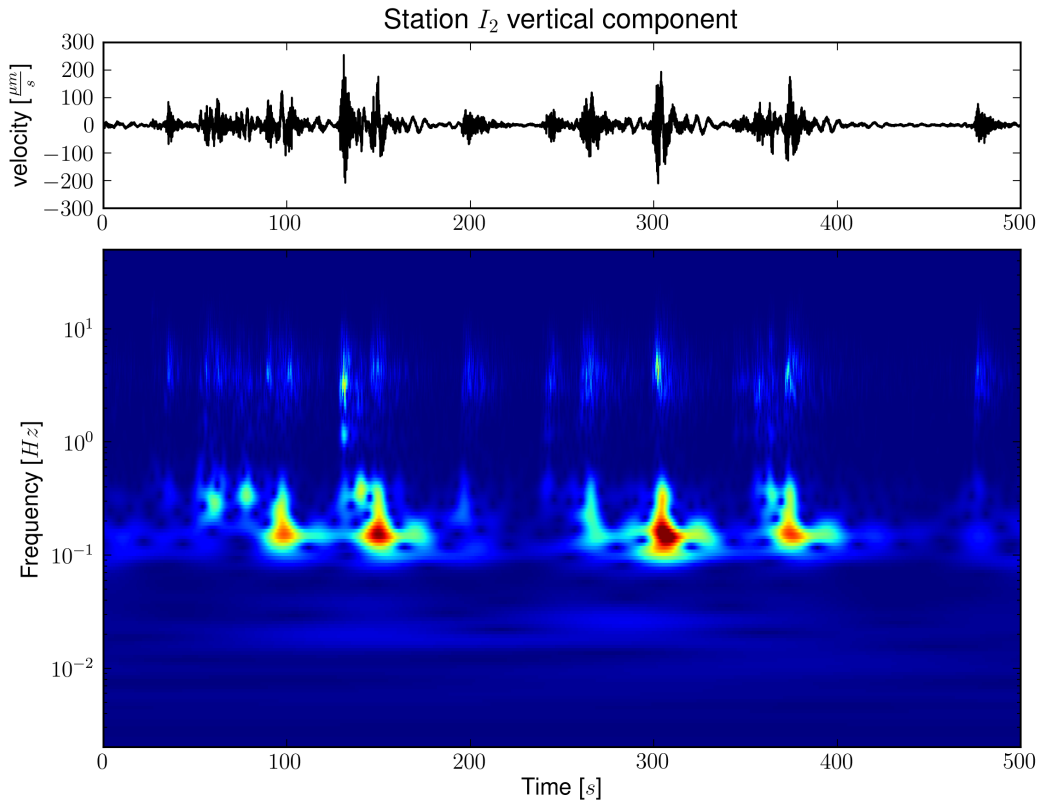


Figure 6.4: 500 second record of ash-loaded eruption sequence. Shown is the vertical component of ground velocity at seismic broadband station  $I_2$  and the continuous wavelet transform of the data using a morlet wavelet. Warm colors define high spectral amplitudes, cold colors lower amplitudes and background. The amplitudes in high-frequency band above 1 Hz denote significantly lower as in the ash-free eruptions.

### *Determination of ground velocity model*

In order to invert for the source processes acting at depth we need a suitable velocity model of Mt. Yasur volcano. The model is based on a recent study by [Perrier \*et al.\* \(2011\)](#), the correlation of seismic and acoustic data with Doppler radar measurements and the results of frequency-wavenumber analysis.

The structure of Mt. Yasur's volcanic edifice is dominated by a complex system of ring faults connected to the collapse of the Siwi caldera that created the Siwi ignimbrite sequence ([Carney and Macfarlane, 1979](#); [Robin \*et al.\*, 1994](#); [Allen, 2005](#)). The post-collapse uplift formed the present Yenhake resurgent block ([Chen \*et al.\*, 1995](#); [Perrier \*et al.\*, 2011](#)). Since about 1,400 years B.C., the eruptive activity has been restricted to Mt. Yasur ([Métrich \*et al.\*, 2011](#)). The analysis of Mt. Yasur's eruptive deposits suggests an continuous activity similar

to the present Strombolian to Vulcanian eruptions, interrupted by irregular sub-plinian eruptive phases (Nairn *et al.*, 1988). A precise estimation of the shallow velocity structure of this complicated geological setting is essential for the determination of the seismic source mechanism connected with the eruptive activity at Mt. Yasur. The localization of seismic sources in and below the volcanic edifice is strongly dependent on the correct determination of sub-surface velocities.

Event onset time	max particle velocity [ $\frac{m}{s}$ ]	fundamental frequency [ $Hz$ ]	slug length [ $m$ ]
2008-08-27 19:04:36.920	155.13	1.10	129.56
2008-08-27 19:05:50.900	126.76	1.50	93.89
2008-08-27 19:06:46.160	27.45	2.92	45.06
2008-08-27 19:11:26.230	73.56	1.81	76.43
2008-08-27 19:24:13.210	65.05	1.79	77.40
2008-08-27 19:25:01.620	70.01	1.97	69.85
2008-08-27 19:25:37.330	136.00	1.35	104.97
2008-08-30 00:00:36.260	199.82	0.80	181.45
2008-08-30 00:15:18.170	57.95	2.19	62.26
2008-08-30 00:17:53.960	31.71	2.22	61.19
2008-08-30 00:19:17.330	71.43	2.45	54.77
2008-08-30 00:24:33.470	60.79	3.05	42.83

Table 6.1: The selected events for estimation of the slug length. Given are event onset time, maximum particle velocity, corrected fundamental frequency in the infrasound records and estimated slug length.

A simple estimate of the mean velocity along the ray path can be retrieved by plotting the seismic and acoustic records as a function of distance from the source. The precise event time is obtained from the onset of Doppler-Radar velocity measurements assuming that the acoustic source is identical with the source of the high-frequency seismic waves. The gradient of a least-squares fit to the estimated onsets of the signals at the respective stations delivers the mean velocity. We use ten bubble burst events at crater A that show clear onsets at all stations in both seismic and acoustic records for the approach. The results suggest a mean  $v_p$  velocity of 2340.2  $\frac{m}{s}$  (top in Fig. 6.7) with a standard deviation of 901.5  $\frac{m}{s}$  and a mean sound velocity of 380.1  $\frac{m}{s}$  with a standard deviation of 4.78  $\frac{m}{s}$  (bottom in Fig. 6.7). It has to be mentioned that the large standard deviation of the seismic  $v_p$  velocity can introduce errors in the source parameters inverted by TR and MT. We will address this issue later when discussing the inversion results. We choose the  $v_s$  value according to the

results of Perrier *et al.* (2011) for the shallow low-velocity layer ( $v_s = 700 \frac{m}{s}$ ) and slightly higher for the deeper layer ( $v_s = 1400 \frac{m}{s}$ ).

We note that in both the seismic and acoustic traces in Fig. 6.7 the fit to the estimated onsets at the stations crosses the y-axis at zero, which supports the hypothesis that the source of the seismic high-frequency and acoustic signals is actually the same. The missing offset in the acoustic trace compared to the seismic trace tells us that the source is shallow, i.e. that the level of the magma column did not lower significantly in the course of the experiment.

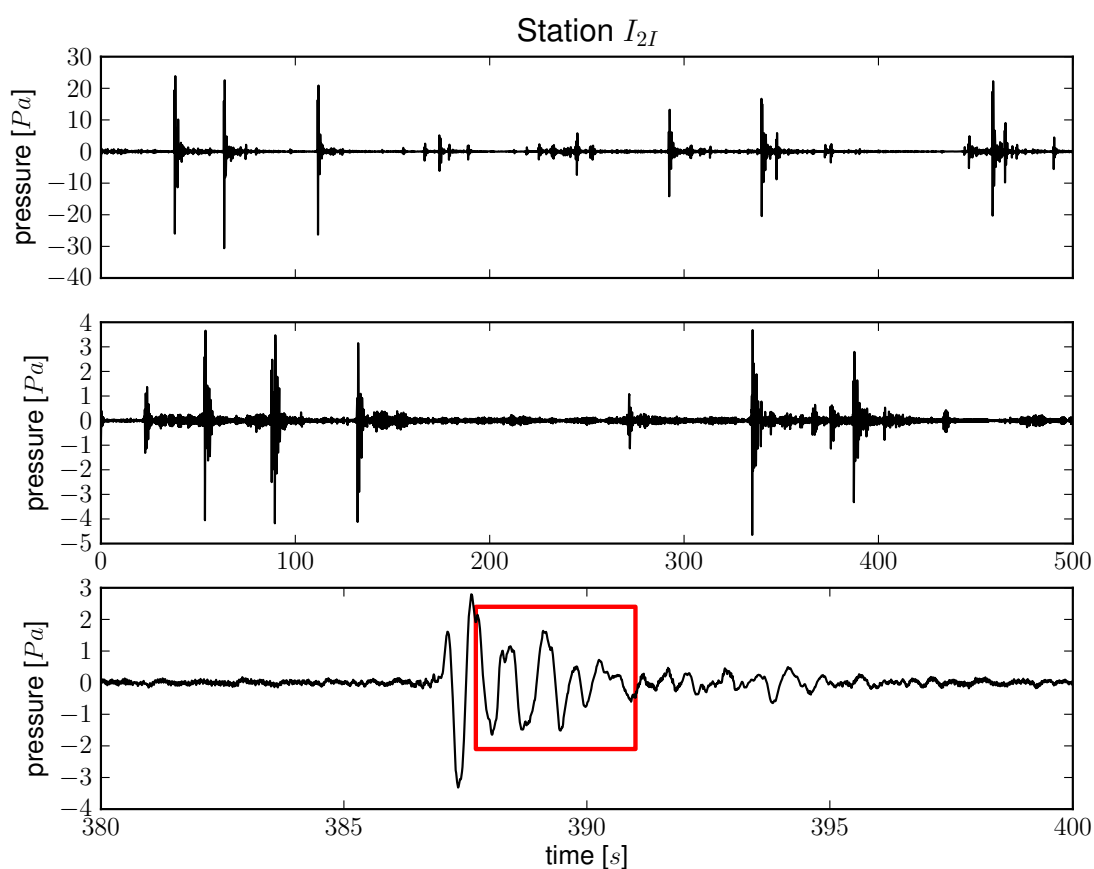


Figure 6.5: 500 second record at acoustic station  $I_{2I}$ . *top:* Ash-free eruptions sequence. *middle:* Ash-loaded eruption sequence. Note the significantly higher acoustic pressures in the ash-free record. *bottom:* Zoom in the event on  $t = 387$  s on the middle trace. The red box show the part of the signal that reflects the resonance of the cavity (the slug) after the passage of the initial shockwave sequence.

*Frequency-wavenumber analysis*

The seismic small aperture arrays allow us to perform frequency-wavenumber (fk) analysis (Lacoss *et al.*, 1969). The classic fk method is based on a horizontal plane wave propagation across the array. Summing coherent signals from single array sites allows to significantly increase the SNR of a seismic signal, a technique usually referred to as beam-forming (e.g., Mykkeltveit *et al.*, 1983). The shifts in coherent signals between array stations give an estimate of the seismic velocity and the event backazimuth. Therefore, the fk method provides a powerful tool to obtain the apparent velocity at the location of the array, to determine the event backazimuth and provides a first basic estimate of the source localization.

The maximum aperture of the installed arrays was  $\sim 500$  m, allowing to resolve frequencies of waves propagating over the array down to  $\sim 1$  Hz. A combination of the arrays II and IV increases the aperture to 1000 m and therefore lowers the frequency limit to  $\sim 0.3$  Hz. It has to be mentioned that using these frequencies we are within one wavelength from the source. Strictly speaking, this prevents the plane-wave assumption used in the fk-analysis. Therefore, the inferred results can only be seen as an estimate of the true ground velocity with a maximum error of  $\pm 200 \frac{m}{s}$ .

The estimated velocity across the array is the apparent velocity (Fig. 6.8), i.e. it has to be corrected for the incidence angle of the waves passing the array. The correct P-wave velocity denotes as

$$v_p = v_{app} \cdot \sin i \quad (6.1)$$

where  $v_{app}$  is the apparent velocity,  $v_p$  the true P-wave velocity and  $i$  the incidence angle. Fig. 6.8 illustrates the energy traveling across the array with a backazimuth corresponding to an event at crater A, which is confirmed by observations made with the Doppler radar. As the combined array II-IV is located relatively far away from the volcano in an area with no present topography a horizontal propagation of the wave across the array is assumed. In this case,  $v_{app} \approx 2.3 \frac{km}{s}$  is equal to the maximum of the true ground velocity  $v_p$ . This may only be an estimate, but it supports the number we received from the measurement of direct waves.

Perrier *et al.* (2011) used small aperture arrays at Mt. Yasur to determine Rayleigh phase velocity dispersion curves using the spatial autocorrelation - (SPAC; Aki, 1957) and the fk - method. With the results of these methods and by applying an inversion technique based on the Neighborhood Algorithm they are able to create one-dimensional velocity profiles for each site. In total their velocity model reaches a depth of 200 m and consist of two layers above a halfspace. The detailed parameters can be seen in the upper part of Tab 6.2.

The estimated parameters for the lower layer are in good agreement with our observations from fk analysis and the measurement of direct waves. However, we find no information on the velocity of one or two shallow layers in our data. Therefore, we choose a model consisting of two layers for our numerical forward and inverse simulations. At top, we insert

a low-velocity layer that includes topography and reaches to a depth of 100 m based on the results of [Perrier \*et al.\* \(2011\)](#). This is an important feature as [Bean \*et al.\* \(2008\)](#) pointed out that at volcanoes the existence of a shallow low-velocity layer has strong influence on the moment tensor mechanisms and magnitudes retrieved from Moment Tensor (MT) inversion at volcanoes. Below this layer, until a depth of 4000 m we significantly increase the seismic velocities to  $v_p = 2300 \frac{m}{s}$  and  $v_s = 1400 \frac{m}{s}$  (lower part of Tab. 6.2) applying a Poisson ratio of 0.2 which is often used in volcanic context ([Christensen, 1996](#)).

	depth [m]	$v_p$ [ $\frac{m}{s}$ ]	$v_s$ [ $\frac{m}{s}$ ]	density [ $\frac{g}{cm^3}$ ]
	5 - 30	600 - 800	250 - 350	
<a href="#">Perrier <i>et al.</i> (2011)</a>	30 - 100	950 - 1550	370 - 675	
	> 100	1420 - 2400	660 - 1060	
this	< 100	1500	700	1.5
study	100 - 4000	2300	1400	2.4

Table 6.2: *top*: Velocity structure of Mt. Yasur as derived by [Perrier \*et al.\* \(2011\)](#). The found velocity model consists of a superficial low-velocity layer, an intermediate layer and an underlying halfspace. *bottom*: Parameters used for the construction of Mt. Yasur's numerical representation. The upper low-velocity layer includes topography and reaches to a depth of 100 m, the lower layer includes the rest of the model down to a depth of 4000 m.

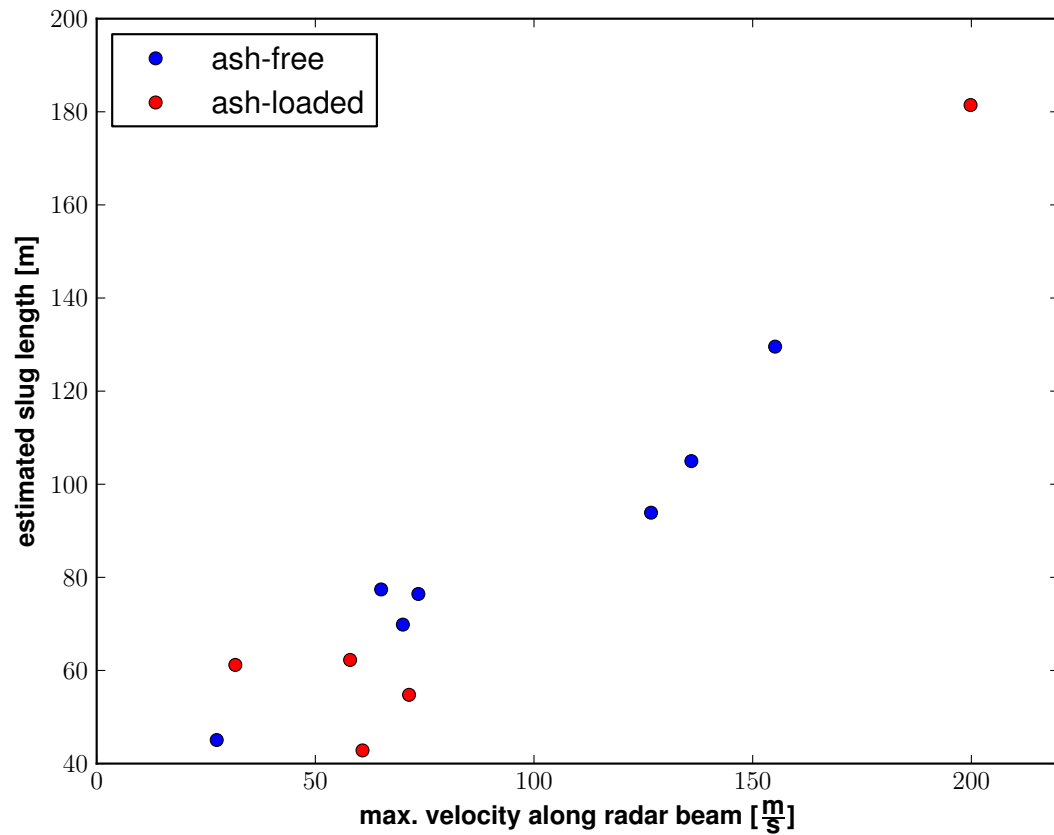


Figure 6.6: The maximum velocity along the radar beam vs the estimated slug length using the infrasound fundamental frequencies for the selected events shown in Tab. 6.1. The red and blue marks indicate event carrying a high fine-ash fraction and no ash, respectively. We observe a good correlation of the two parameters.

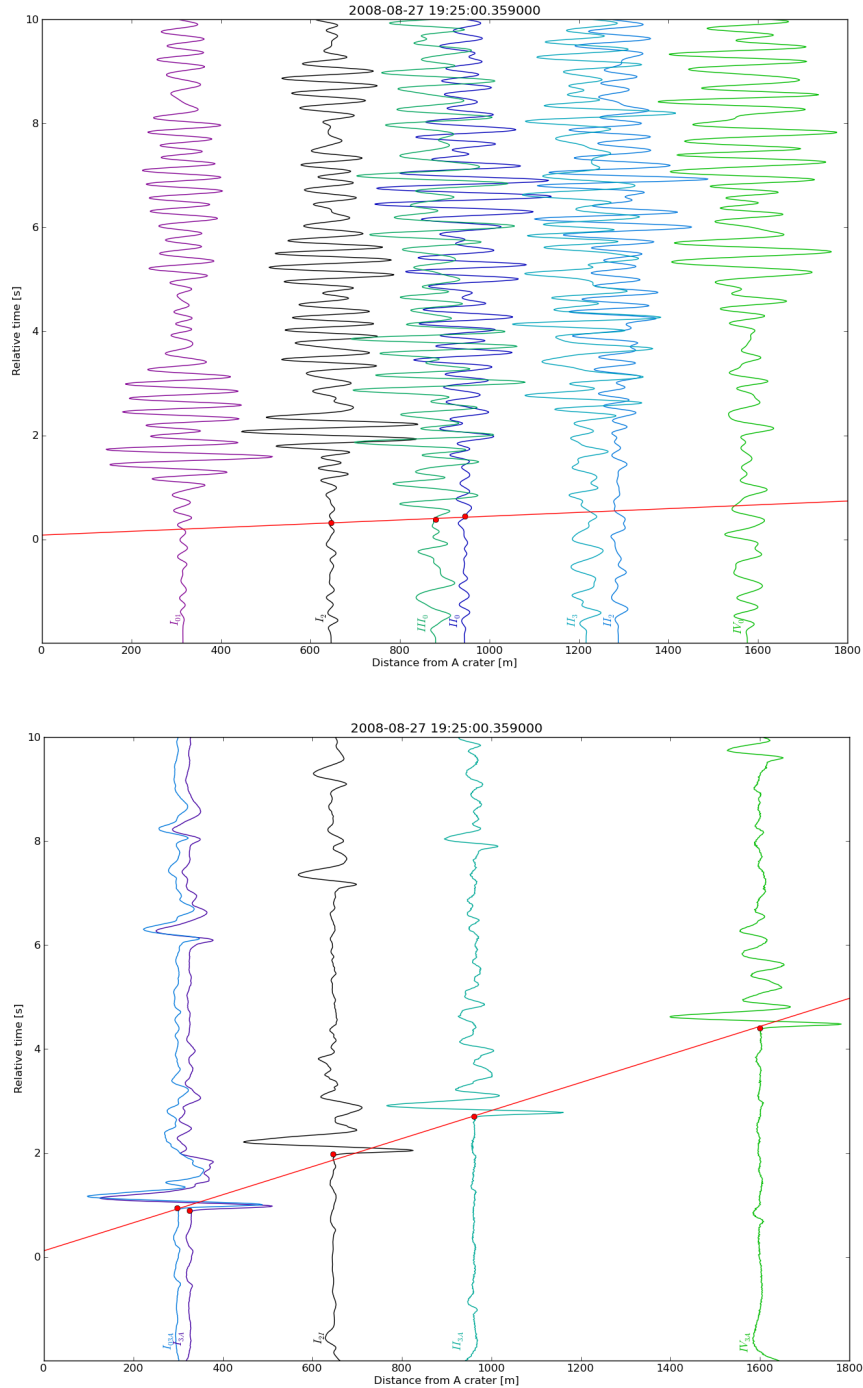


Figure 6.7: *top*: Seismic traces of stations  $I_{01}$ ,  $I_2$  (array I),  $III_0$  (array III),  $II_0$ ,  $II_3$ ,  $II_2$  (array II) and  $IV_0$  (array IV). The corresponding event is a Strombolian bubble burst on the 27 August 2008, at 19:25:00. The stations are arranged in their true distances from the vent exit, the red dots mark the estimated onsets and the red line the fitted gradient. The slope corresponds to a mean  $v_p$  velocity of  $2749.6 \frac{m}{s}$ . *bottom*: Acoustic traces of stations  $I_{03A}$  (at seismic station  $I_{01}$ ),  $I_{3A}$  (seismic station  $I_1$ ),  $I_{2I}$  (acoustic broadband station at seismic station  $I_2$ ),  $II_{3A}$  (seismic station  $II_0$ ) and  $IV_{3A}$  (seismic station  $IV_0$ ). The corresponding event is a Strombolian bubble burst on the 27 August 2008, at 19:25:00. The stations are arranged in their true distances from the vent exit, the red dots mark picked onsets and the red line the fitted gradient. The slope corresponds to a mean sound velocity of  $382.3 \frac{m}{s}$ .

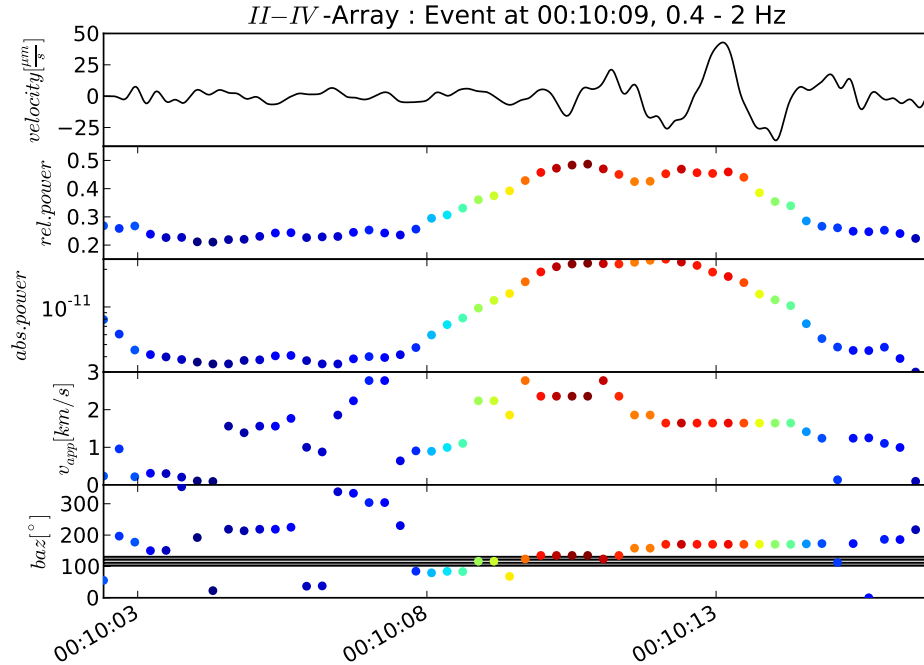


Figure 6.8: fk analysis using array II-IV on a Strombolian bubble burst event at crater A. The data is bandpassed between  $f_{min} = 0.4$  and  $f_{max} = 2$  Hz. Shown are the vertical velocity record of seismic station  $II_0$ , the calculated relative and absolute power, the apparent ground velocity and the source backazimuth. The shading in the lower plot denotes the backazimuth of the centre of gravity of array II - IV to *upper*: crater A and *lower*: crater C.

### Numerical method

Both TR and MT inversion are based on a precise modeling of the seismic wavefield. The specific conditions at volcanoes make certain demands on the numerical solver in order to capture the observed complex wave scattering, e.g. the capability to handle highly complicated topography and strongly heterogeneous geological settings. As our study aims to include a modeling of high frequencies (up to 5 Hz) the influence of the topography is clearly relevant (Ripperger *et al.*, 2003; Parsiegla and Wegler, 2008). Bean *et al.* (2008) showed that complex topography can also have a strong influence in the LP band. The importance of a correct free-surface approximation by the spatial problem discretization is well known and has been analyzed by various groups (e.g. Robertsson, 1996; Bohlen and Saenger, 2006; Pelties *et al.*, 2010). Therefore, we employ the software SeisSol to model the seismic wave propagation (Dumbser and Käser, 2006). SeisSol is a high-order accurate Discontinuous Galerkin Finite Element method (DGM) implemented on unstructured tetrahedral meshes. The code was successfully verified in different benchmarks, (e.g., Chaljub *et al.*, 2010) that focus on models with strong material contrasts and complex topography.

Compared to standard Finite Difference methods (FDM), free-surface boundary conditions are incorporated more easily and naturally by Finite Element methods (FEM). Furthermore, FEM enable the use of unstructured tetrahedral or deformed hexahedral element types that can be easily aligned to undulating material interfaces and non-planar topography. Due to the short wavelength of topography of Mt. Yasur we choose a tetrahedral element discretization to expedite the meshing process so that the complete model building sums up to only 2 hours. The resulting model discretization is presented in Fig. 6.9.

In order to get reliable synthetic seismograms the shortest modeled wavelength is sampled by two elements with an approximation order of  $\mathcal{O}6$  in space and time. This corresponds to an element edge length of  $h = 70$  m in the shallow low velocity layer and  $h = 140$  m in the volume below. In addition, that mesh coarsening towards the sides is applied to save computational costs in areas that do not contribute to the recorded time series. No spurious reflections either from the absorbing boundaries nor from the mesh coarsening have been observed. As the complex rheological features of Mt. Yasur are unknown, we choose a fully elastic modeling of the seismic wave propagation.

The numerical model of Mt. Yasur includes topography that is based on 90 m resolution digital elevation model provided by the USGS ([http://dds.cr.usgs.gov/srtm/version2\\_1/SRTM3/Australia/](http://dds.cr.usgs.gov/srtm/version2_1/SRTM3/Australia/)). The total model dimensions are  $25 \cdot 25 \cdot 13$  km, large enough to prevent reflections from the non-physical model boundaries. In the region of interest, i.e. within a radius of 1 km around the crater region and down to 4 km depth, we use a fine scale mesh to be able to accurately resolve frequencies up to 5 Hz. The rest of the model is filled up with increasingly larger elements.

## 6.4 Results

---

The simultaneous recording of various geophysical parameters allows us to define the source processes of Strombolian eruptions at Mt. Yasur both at the surface and at depth. We begin with the determination of the size of the resonating cavity (the slug) based on infrasound records. Following this, we use TR and MT inversion to determine the source parameters of VLP signals with the purpose to constrain source depth, conduit geometry and the radiated source pattern.

### 6.4.1 Determination of source extent using infrasound

The acoustic waves are recorded by three narrow band arrays consisting of three stations each. Additionally, a MB2005 broadband sensor is deployed at the seismic station  $I_2$  (Fig. 6.1). As shown in Fig. 6.5 we record signals that vary strongly in acoustic amplitudes. The different amplitude characteristics are related to the above mentioned surface activity regimes

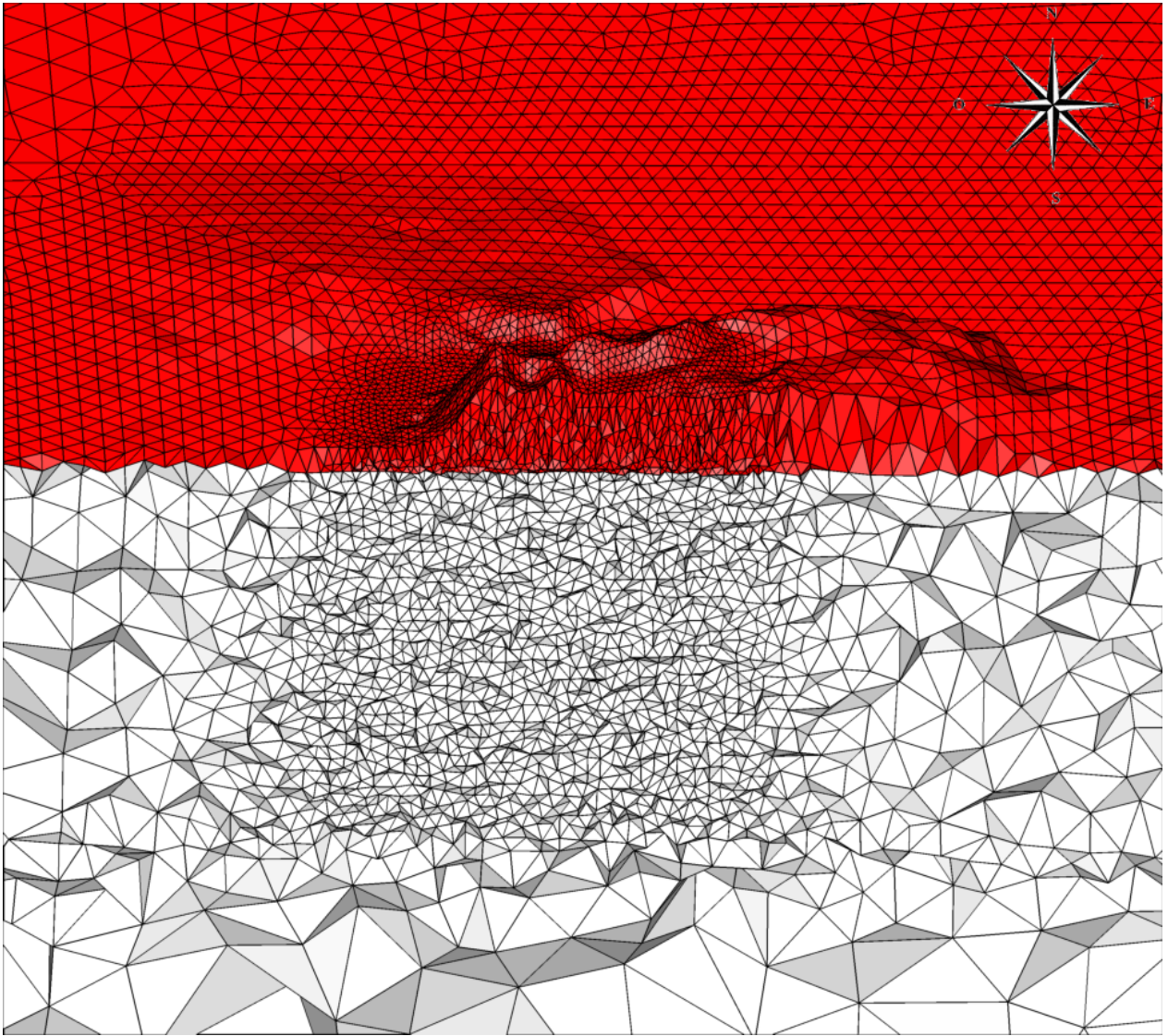


Figure 6.9: Discretized model of Mt. Yasur including topography. Shown is a vertical cut at  $x = 0$ , the red area is the superficial low velocity layer with topography in north direction. The white elements illustrate a higher seismic velocity in the subsurface representation of Mt. Yasur. The volcanic edifice is finely meshed in the center to allow the simulation of frequencies up to 6 Hz. Note the mesh coarsening to the sides of the model to save computational time. Topography is exaggerated by a factor of three.

of ash-free and ash-rich explosions. Besides the recording of the shock wave caused by the small distance between source and receiver, Vidal *et al.* (2006) pointed out very clearly in both experiment and theory, that the acoustic amplitude can not be correlated with initial gas-overpressure at the source (in the bursting bubble). The reason for this is the strong dependence of the acoustic amplitudes on the characteristic time of rupture of the bubble shell as well as the source radiation pattern. However, the fundamental resonance frequency after the passage of the shock wave (red box in the lower trace in Fig. 6.5) is strongly correlated with the cavity length and therefore allows an estimation of the source volume.

Generally, each surface activity regime produced different signal signatures not only in terms of amplitudes, but also in terms of a fundamental frequency (Meier *et al.*, 2009). During phases of increased ash loading infrasonic transients are characterized by lower frequencies and lower amplitudes. This can be attributed to a different source mechanism and/or propagation effects (Meier *et al.*, 2012). In order to estimate the source volume from selected infrasound observations it is thus necessary to first correct the signal frequency content for propagation effects. This correction is performed using the approach of Meier *et al.* (2012). They showed that the presence of a fast-moving volcanic cloud leads to strong signal alteration due to Doppler-shifting. Following equation (5) in their paper, the fundamental frequency of the undisturbed signal at the source  $f_{src}$  is related to the frequency of the recorded signal  $f_{rec}$  via

$$f_{src} = f_{rec} \frac{1 - v_{cloud}/c_{air}}{1 - v_{cloud}/c_{cloud}} \quad (6.2)$$

Here,  $v_{cloud}$  is the propagation speed of the volcanic cloud depending on the strength of explosion under consideration, assuming that the minimum velocity of the cloud is given by the speed of the fastest particles measured with the Doppler-radar.  $c_{cloud}$  and  $c_{air}$  are the speed of sound inside and outside the volcanic cloud, respectively. The speed of sound inside the cloud varies according to the temperature of the cloud and its ash loading, i.e. according to the surface activity regime.

To calculate the undisturbed fundamental frequency for selected signals we assumed a mean cloud temperature of 800 °C (close to the estimated magmatic temperature) and an ash loading of 5% and of 95% to mirror the ash-free and the ash-rich scenarios, respectively. The propagation speed of the volcanic cloud was extracted from Doppler-radar measurements in all cases. The calculated corrected fundamental resonance frequencies are then used to estimate the slug length using the  $\frac{\lambda}{4}$  method (Vidal *et al.*, 2006). Tab.6.1 summarizes the selected events, the associated fundamental frequencies and the estimated resonator lengths. The uncertainty in sound velocity results in an maximal error of  $\pm m$  when estimating the slug length. We find a good correlation between the estimated slug length and the maximum particle velocity derived from Doppler-Radar measurements (Fig. 6.6). Large slugs are associated with more vigorous explosions showing higher particle velocities.

We constrained the shallow source parameters of explosive eruptions at Mt. Yasur and demonstrated that we observe a correlation between slug size and particle ejection velocity.

We will now focus on the characterization of the source pattern of the VLP signals at depth using TR imaging and MT inversion.

### 6.4.2 Time reversal

As previously discussed, the source of the high-frequency part of the seismic signals at Mt. Yasur is connected to the bubble burst at the free surface. However, the origin of the VLP part of the signal that precedes the bubble burst remains unclear. Various studies have shown that this part of the signal is likely to be associated with fluid movement, e.g. with the rise of gas slugs in the conduit (e.g., [Chouet \*et al.\*, 2003](#); [Aster \*et al.\*, 2003](#); [O'Brien and Bean, 2008](#)).

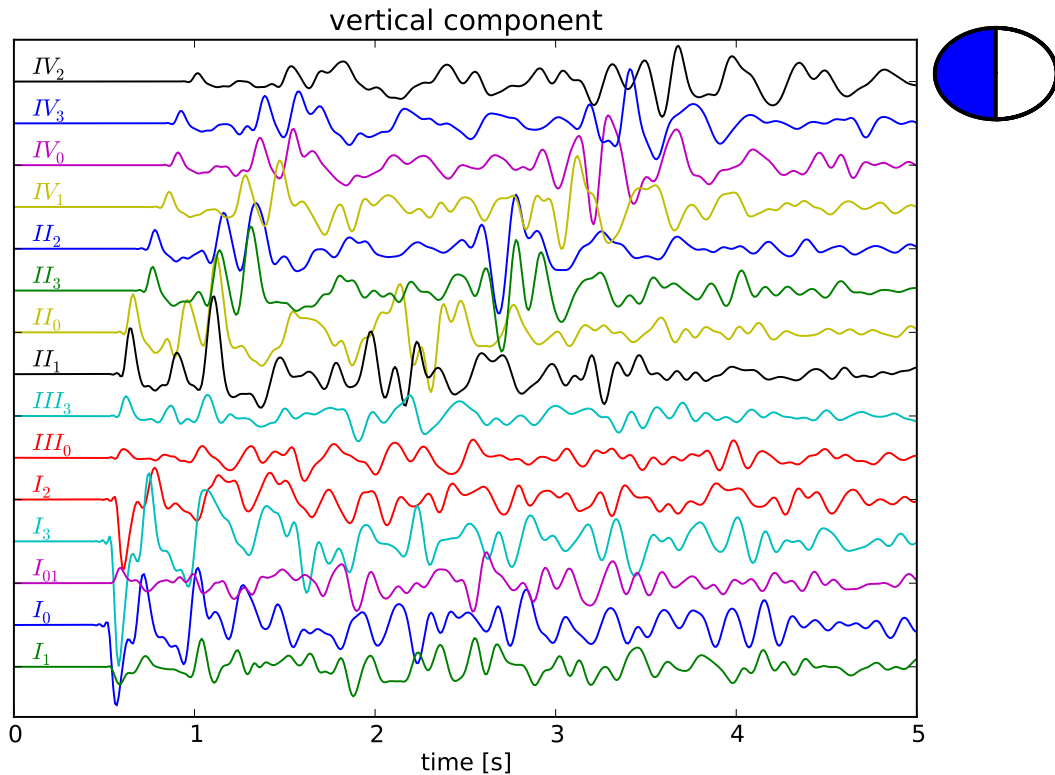


Figure 6.10: Vertical component of synthetic seismograms recorded with the Mt. Yasur stations setup. The beachball in the upper right shows the used source mechanism. The moment tensor ( $M_{xz}$ ) was placed at a depth of at 600 m. The source time function was a brune pulse with a flat amplitude spectrum up to 6 Hz. All seismograms are shown in the same amplitude range.

TR has been used for a long time in medical imaging (e.g., Fink, 1997; Fink and Tanter, 2010) and non-destructive testing (e.g., Chakroun *et al.*, 1995; Sutin *et al.*, 2004), but only recently in seismology (e.g., Gajewski and Tessmer, 2005; Larmat *et al.*, 2006; Allmann and Shearer, 2007; Steiner *et al.*, 2008; Larmat *et al.*, 2008) mainly due to advances in computational power. Lokmer *et al.* (2009) imaged with TR the location and radiation pattern of synthetic long-period volcanic tremor in 2D. O'Brien *et al.* (2011) located the source of long-period events at Mt. Etna (Italy) with TR and showed the consistency of the solution with MT inversion and cross-correlation methods. However, Kremers *et al.* (2011) showed in an attempt to use TR on finite sources, that the limitations of the method begin where the source no longer fulfills the requirement of being point-localized. Nevertheless, TR can deliver an estimate of the source location and time without any a-priori assumptions of these parameters.

In the TR simulations, the seismograms recorded at the stations are reversed with respect

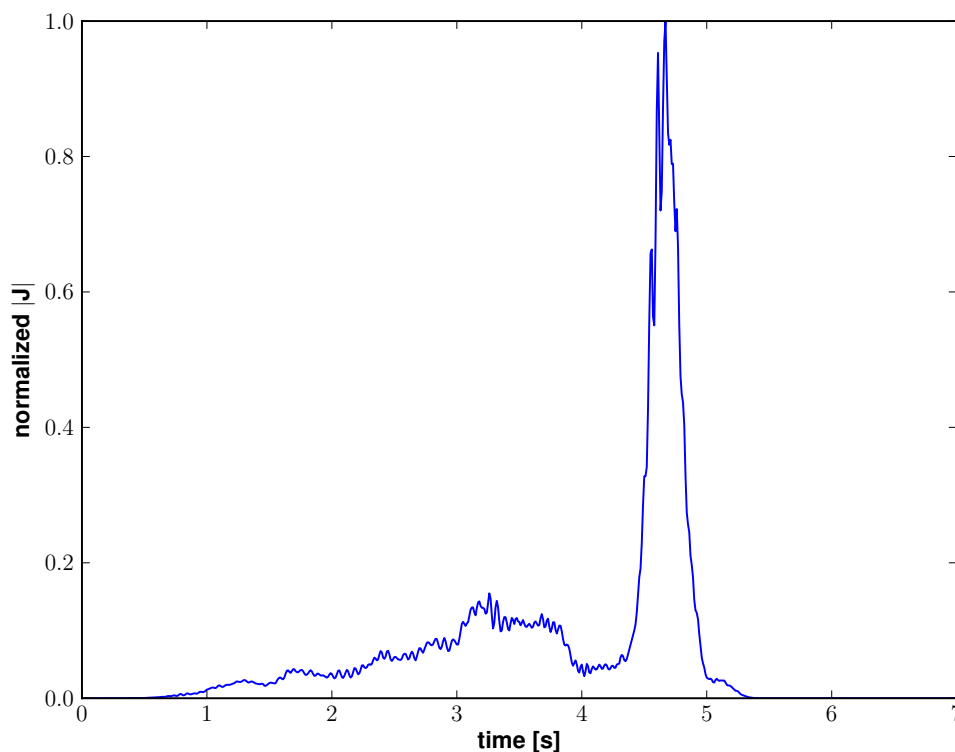


Figure 6.11: The normalized energy current density vector  $J$  for the selected source volume based on the maximum magnitude. At the source time  $t_0 = 4.7s$  we observe a sharp peak.

to time and re-injected in the model as three-component single forces. Each seismogram is divided by its maximum amplitude to account for the effects of geometrical spreading and attenuation. The medium is chosen completely homogeneous to avoid high amplitude reflections from a shallow layer. Furthermore, in the TR simulations the free-surface is replaced by an absorbing boundary condition in order to avoid so-called artificial ghost waves (e.g., Larmat *et al.*, 2009; Kremers *et al.*, 2011) that travel along the surface. Since surface waves have much larger amplitudes than typical body waves, finding the exact source position is strongly blurred by this spurious effect. Our first-order approach of using simple outflow boundaries reduces this effect significantly. We sample the time-reversed wavefield with a rate of 100 Hz using a regular grid of receivers that are placed in the model domain with a spacing of 100 m. The source location is found by computing the energy of the recorded signals at every time step for all receivers in the grid.

We first use TR to locate the source of this part of the signal using events that show clear onsets and good SNRs. In a first step we demonstrate the functionality of the method in a purely synthetic test, in a second step we use TR to locate the source of VLP signals recorded at Mt. Yasur.

#### *Synthetic test*

We set up a synthetic test to validate the used setup and algorithm. We placed a point source represented by a moment tensor  $M_{xz}$  ( $M_{zx}$ ) at  $x = -50$ ,  $y = 0$  and  $z = -600$  m below the centre of the volcano and model the excited forward wavefield with SeisSol. The wavefield is recorded using the station setup shown in Fig. 6.1. The recorded seismograms (Fig. 6.10) are weighted uniformly and are re-injected into the model as single forces. We use the described receiver grid in the model of Mt. Yasur to record the propagated time-reversed wavefield. Larmat *et al.* (2009) and O'Brien *et al.* (2010) showed that the energy current density vector  $J$  provides a valuable tool to locate the source in time and space. We compute  $J$  in a test volume extending 200 m in every direction around a source position throughout the model domain. The volume with the maximum of the magnitude of  $J$  is then chosen as the most likely source position, and the location of the maximum in time as the source time. The method finds the correct source volume of the forward simulation and the correct source time at  $t_0 = 4.7s$  (Fig. 6.11). The energy of the wavefield shown in three slices through the model at source time illustrates the successful source location (Fig. 6.12). We observe that the focus is not clearly constrained to the marked source location, an inaccuracy that we attribute to the relatively small number of stations.

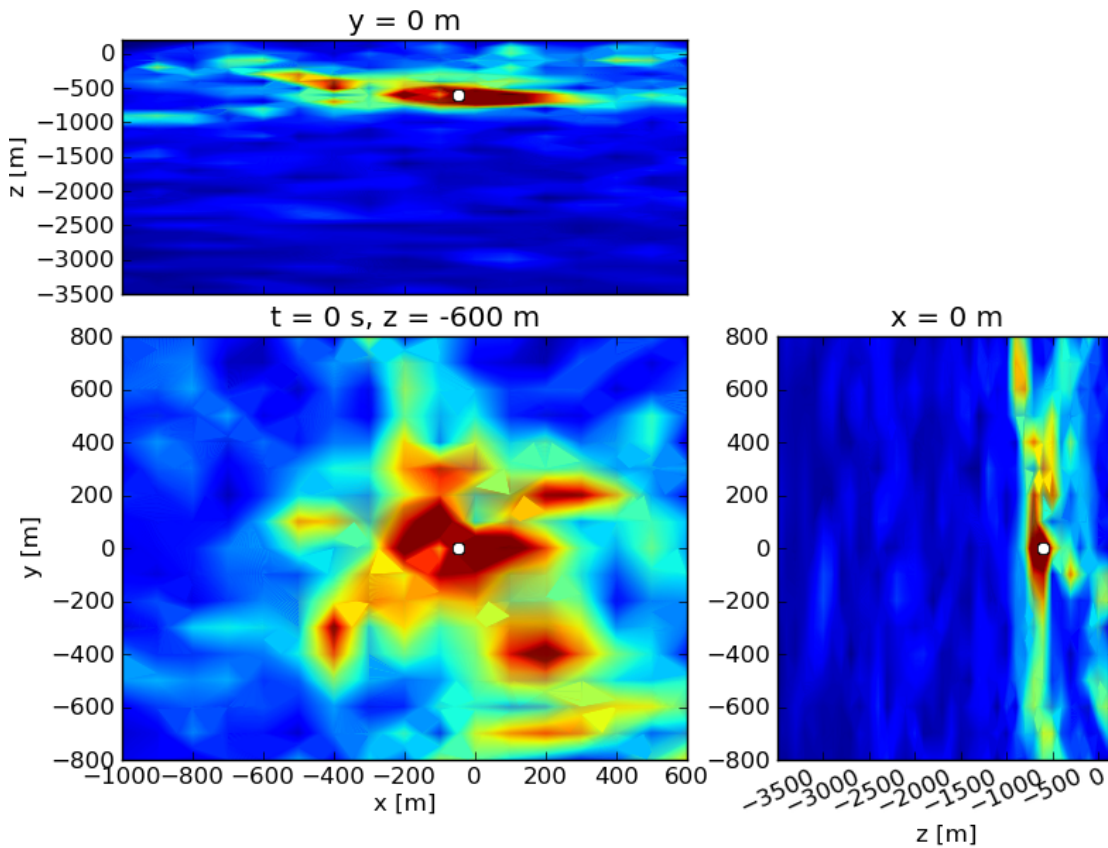


Figure 6.12: The energy of the time-reversed wavefield at source time shown in three slices through the model domain. *lower left:* Horizontal cut at  $z = -600$  m; *upper left:* Vertical cut at  $y = 0$  m; *right:* Vertical cut at  $x = 0$  m. The white sphere denotes the true location of the source position. The focus around the correct source position at  $x = 0$ ,  $y = 0$  and  $z = -600$  m is visible in all three slices.

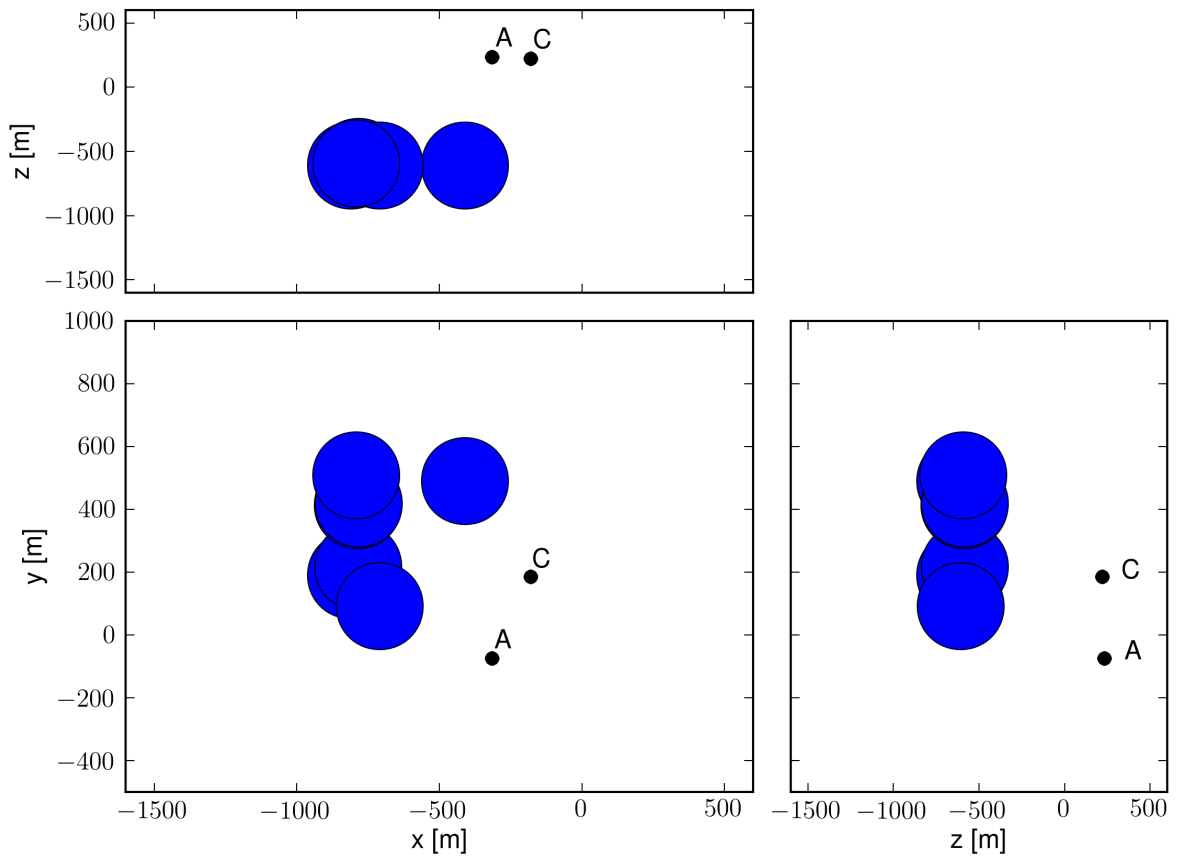


Figure 6.13: The estimated source volume for the seven time-reversed events shown in three slices through the model domain. *lower left*: Horizontal cut at  $z = 0$  m; *upper left*: Vertical cut at  $y = 0$  m; *right*: Vertical cut at  $x = 0$  m. The events cluster at a source depth of  $\sim 600$  m, in a region north-west of the crater area. The extent of the spheres denoting the source position is  $\sim 400$  m in every direction.

#### *Mt. Yasur data*

TR simulations are performed on seven events that show clear signal onsets and good SNRs. The recorded seismograms are corrected for instrument response and bandpassed with corners at  $f_{min} = 0.2$  and  $f_{max} = 0.9$  Hz and are flipped in time and normalized to remove the influence of close stations. As described before, we compute the current energy density vector  $J$  to identify the source time and volume in a volume search procedure. The resulting source locations for the seven selected events are illustrated in Fig. 6.13. The source location is shown as a perfect sphere for clarity. We observe that the events cluster in the

same region, however the extent of the source volume is relatively large ( $\sim 400$  m in every direction). The high energies at the surface ( $z = 0$ ) represent artificial ghost waves that are not necessarily part of the forward wavefield and are therefore neglected. An example is shown in Fig. 6.14. The large extent of the source volume can be attributed to the long wavelengths used in the TR simulations and the relatively small station number. Additionally, the flat topography present at Mt. Yasur is not favorable for TR. Taking into account all these negative conditions, the retrieved source estimate is still a good result.

With the relatively large source region predicted by TR we have a first estimate of the source location of the VLP signals at Mt. Yasur. In the following we perform MT inversion on the VLP events aiming to further constrain source position and mechanism.

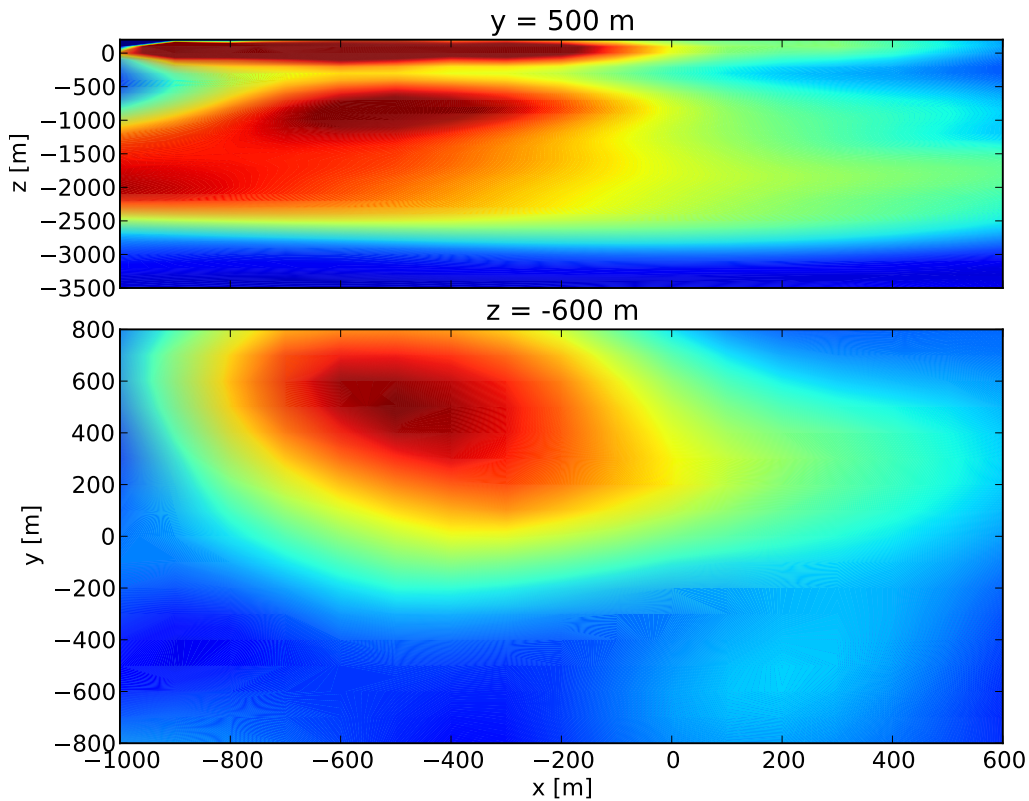


Figure 6.14: The energy of the time-reversed wavefield at source time indicated by the energy current density vector  $J$ . The source pattern is shown in two slices through the model domain at  $z = -600$  m and  $y = 500$  m.

### 6.4.3 Moment tensor inversion

MT inversion is the most common technique to infer the source mechanism and location of LP to VLP events at active volcanoes (e.g., [Ohminato \*et al.\*, 1998](#); [Chouet \*et al.\*, 2003](#); [O’Brien and Bean, 2008](#)). Usually, the inversion is carried out in a grid search over a large number of possible source locations. Based on the misfit of the synthetic seismograms compared to the observation a source location is selected. The inverted moment tensor can be decomposed into six independent mechanisms and corresponding source time functions. Additionally, the moment tensor can be constrained to a single mechanism.

#### *Green’s Functions*

We place a regular grid of possible source positions (trial sources) in the Mt. Yasur model that will be used by the Moment Tensor (MT) inversion scheme to identify the position based on the minimum misfit between observed and synthetic data. The trial source positions cover an area of  $1 \times 1$  km around the crater and reach to a depth of 4 km. In the shallow low-velocity zone the grid spacing is set to 50 m, below that and down to depth of 1 km it is increased to 100 m, while the rest of the model is covered by a grid with a spacing of 200 m. This results in a number of 7884 trial sources. To calculate Green’s Functions (GF) with SeisSol, this large number of trial sources would result in  $7884 \cdot 6 = 47304$  forward simulations, i.e. six calculations for each independent moment tensor component times the number of trial sources. Therefore, we chose a reciprocal calculation of the GF (for details see [Graves and Wald, 2001](#)). This procedure dramatically reduces the computational cost for the calculation of the GF, as we are now left with only  $16 \cdot 3 = 48$  calculations, i.e. three calculations for the orthogonal components times the number of receivers.

#### *Inversion*

For the inversion we use an algorithm developed by [van Driel \*et al.\* \(2012\)](#). The method allows for both constrained and unconstrained MT inversion, performing a search on a grid of trial source positions and minimizing the misfit between observed and synthetic data. The misfit  $\epsilon^2$  minimized for each frequency denotes as

$$\epsilon^2 = \sum_{i=1} W_i^{stat} \frac{\sum_j \int |u_j(x_i, t) - u_j^{inv}(x_i, t)|^2 dt}{\sum_j \int |u_j(x_i, t)|^2 dt} \quad (6.3)$$

where  $i$  is an index for the station,  $j$  for the component,  $u$  is the observed data,  $u^{inv}$  the inverted seismogram and  $W$  a diagonal weighting matrix. This means that the seismograms are weighted with the sum of the  $l^2$ -norm of all three components in the MT inversion, resulting in an equal weighting of close and distant stations ([Ohminato \*et al.\*, 1998](#)). An additional model selection criterion is given by Akaike’s Information Criterion (AIC, [Akaike, 1974](#)). Again, we will first show the functionality of the code in a synthetic test case and

then invert selected recorded events first in an unconstrained inversion. In a second step the dominant inverted mechanism is then used in a constrained inversion as suggested by Lokmer *et al.* (2009) and Bean *et al.* (2008).

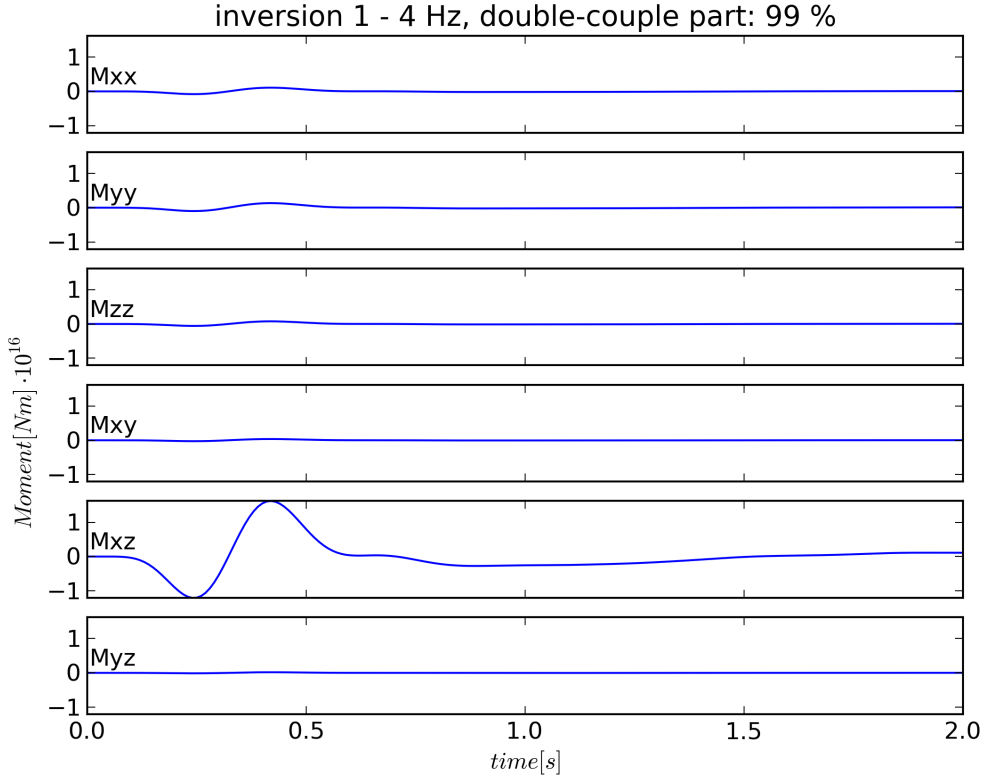


Figure 6.15: The six independent moment tensor components of a synthetic test for an unconstrained inversion over a grid covering the full model domain. As input we used a brune pulse on the  $M_{xz}$  component. This component is successfully recovered by the algorithm, with a double-couple component of 99%.

### *Synthetic test*

For a functionality test of the algorithm and the reciprocally calculated GF we use data from the same forward simulation as in the synthetic TR test case (Fig.6.10). We perform an unconstrained inversion over the full grid of 7884 trial sources in a frequency band from 1 - 4 Hz. The inversion finds the correct source location at  $x = -50$ ,  $y = 0$  and  $z = -600$  m. The resulting time-dependent moment tensor shows only significant entries in the

$M_{xz}$  component (Fig. 6.15), delivering precisely the used moment tensor component of the forward simulation. The decomposition of the moment tensor delivers a double-couple part of 99%. This purely synthetic test validates the functionality of the used algorithm and the reciprocally calculated GF and therefore justifies the application of the method to real data.

#### *Mt. Yasur data*

We perform MT inversion on a predefined set of events that show good SNRs at all seismic stations. The inversion is performed in the VLP to LP band (0.2 - 0.9 Hz), aiming to constrain source location and mechanism. We start by performing an unconstrained inversion over the full grid space, which means that the source mechanism is time-dependent. The inverted locations show a clustering in four regions (Fig. 6.16), three of which are in the crater region of Mt. Yasur ('A' and 'C' denote the vents producing explosive eruptions). The fourth cluster is located at the boundary of the trial sources grid and is therefore neglected. The inverted mechanisms show dominant isotropic components with small double-couple (DC) and almost no compensated linear vector dipole (CLVD) parts (upper part of Tab. 6.3). A clear representation of the results can be obtained by plotting the components in the Cartesian diamond diagram (Fig. 6.18, Chapman and Leaney, 2012). For the constrained inversion we focus on the clusters that were located in the crater region. We keep the mechanism fixed to a purely isotropic source and perform a grid search 500 m in each direction around the previously detected source location. The result show that the scatter in the source position is now significantly lower (lower part in Tab. 6.3). A waveform fit at broadband station  $III_0$  between observed and synthetic data is shown in Fig. 6.17 for event 2008-27-08 19:28:23. The relatively large misfit implies that our velocity model is not completely resembling the seismic velocity structure at Mt. Yasur. As described earlier, this can have a strong influence on the inverted source mechanism (Bean *et al.*, 2008). The results of the constrained inversion illustrate that the recorded signals can be explained by a purely isotropic source mechanism. The stability of the misfit criterion is illustrated for one event in Fig. 6.19. The horizontal slide at source depth shows the probability density function of the summed  $l_2$ -misfit (Tarantola, 2005). In a significance test we performed the inversion with varying rates of CLVD ( $\pm 25\%$ ) plus an isotropic component. The results show that misfit and source position differ within the standard deviation and the AIC drops according to the reduced number of degrees of freedom. This shows that the isotropic component is the defining source mechanism in the inverted events and the CLVD part can not be significantly resolved by the data. From tests with erroneous velocity models we know, however, that this introduces a significant isotropic component in the inverted mechanism (*F. Siepmann pers. comm.*). Nevertheless, the strong isotropic component of the source mechanism of the recorded VLP events at Mt. Yasur seems to be a stable feature. Unfortunately, this dominant isotropic component allows no conclusion on the source geometry and thus the orientation of the dike or feeder system at Mt. Yasur volcano.

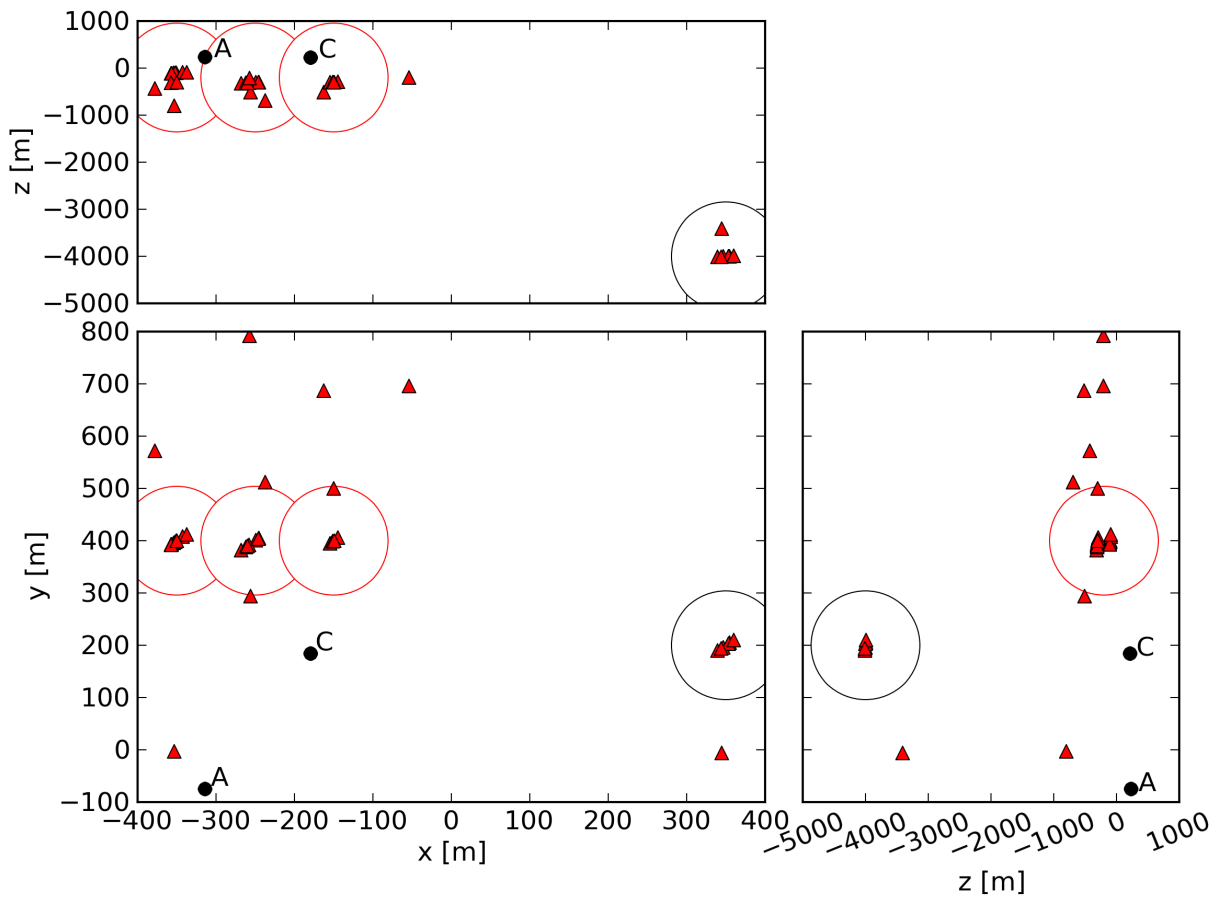


Figure 6.16: The locations of the inverted moment tensor performing an unconstrained inversion in the frequency band 0.2 - 1 Hz on the *lower left*:  $xy$  - plane; *upper left*  $xz$  - plane; *right*:  $zy$  plane. We observe clustering of the locations in three main regions (red circles). The locations in the black circle cluster at the model boundary and are therefore neglected. 'A' and 'C' denote the location of the craters.

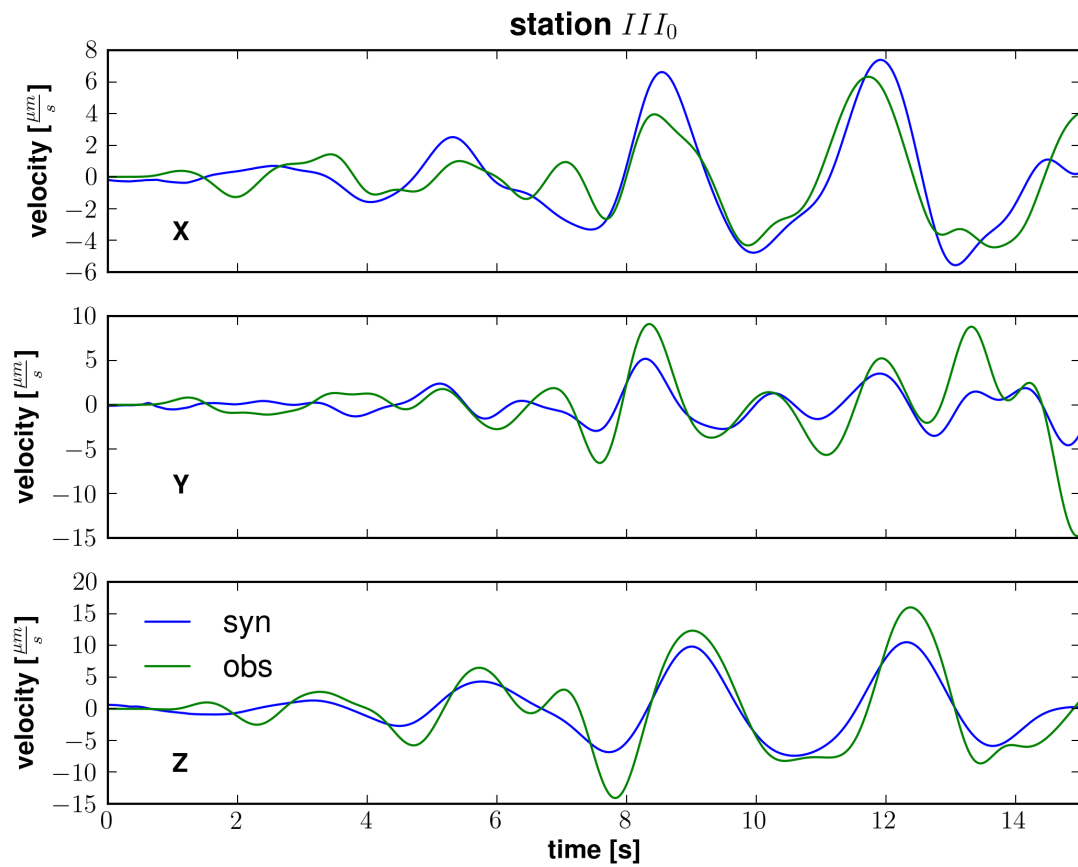


Figure 6.17: Waveform fit between observed (green) and synthetic (blue) data for event 2008-27-08 19:28:23 at station  $III_0$ .

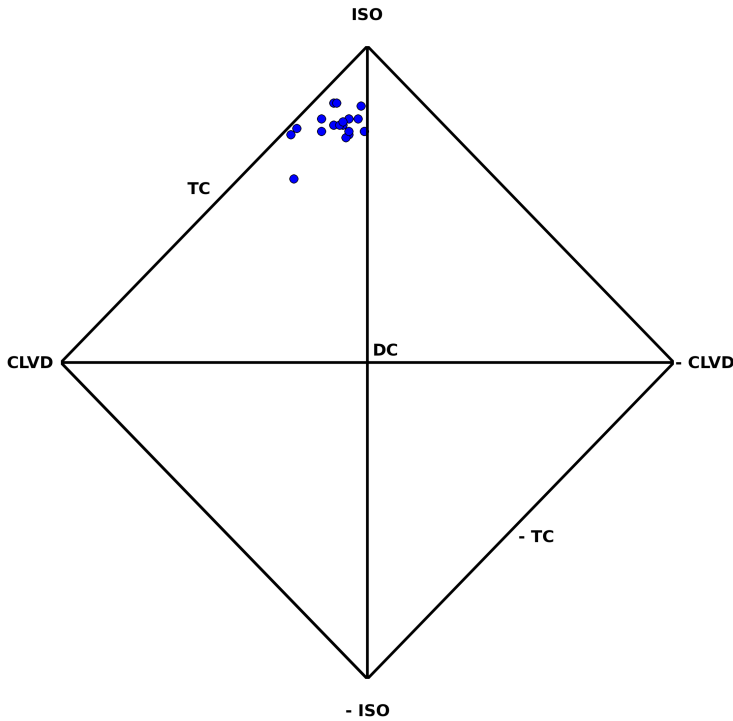


Figure 6.18: The inverted mechanisms of the unconstrained inversion shown in a cartesian diamond diagram (Chapman and Leaney, 2012). 'ISO' denotes a  $M_{iso}$  source, 'CLVD' a  $M_{clvd}$  source and 'DC' a  $M_{DC}$  source. 'TC' marks the position of a tensile crack. All results of the unconstrained inversion cluster in the area representative of an almost pure isotropic source.

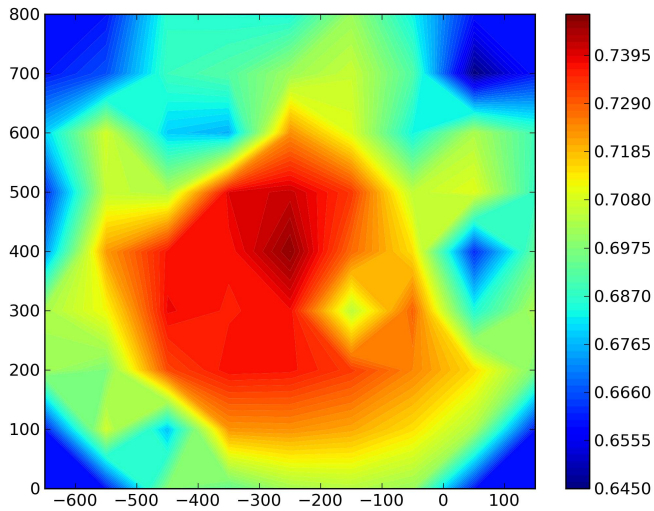


Figure 6.19: Horizontal cut through the trial source grid at the inverted source depth for event 2008-30-08 00:11:22. The contours denote the probability density function of the summed  $l_2$  misfit (Tarantola, 2005). The function shows a stable maximum at the source position.

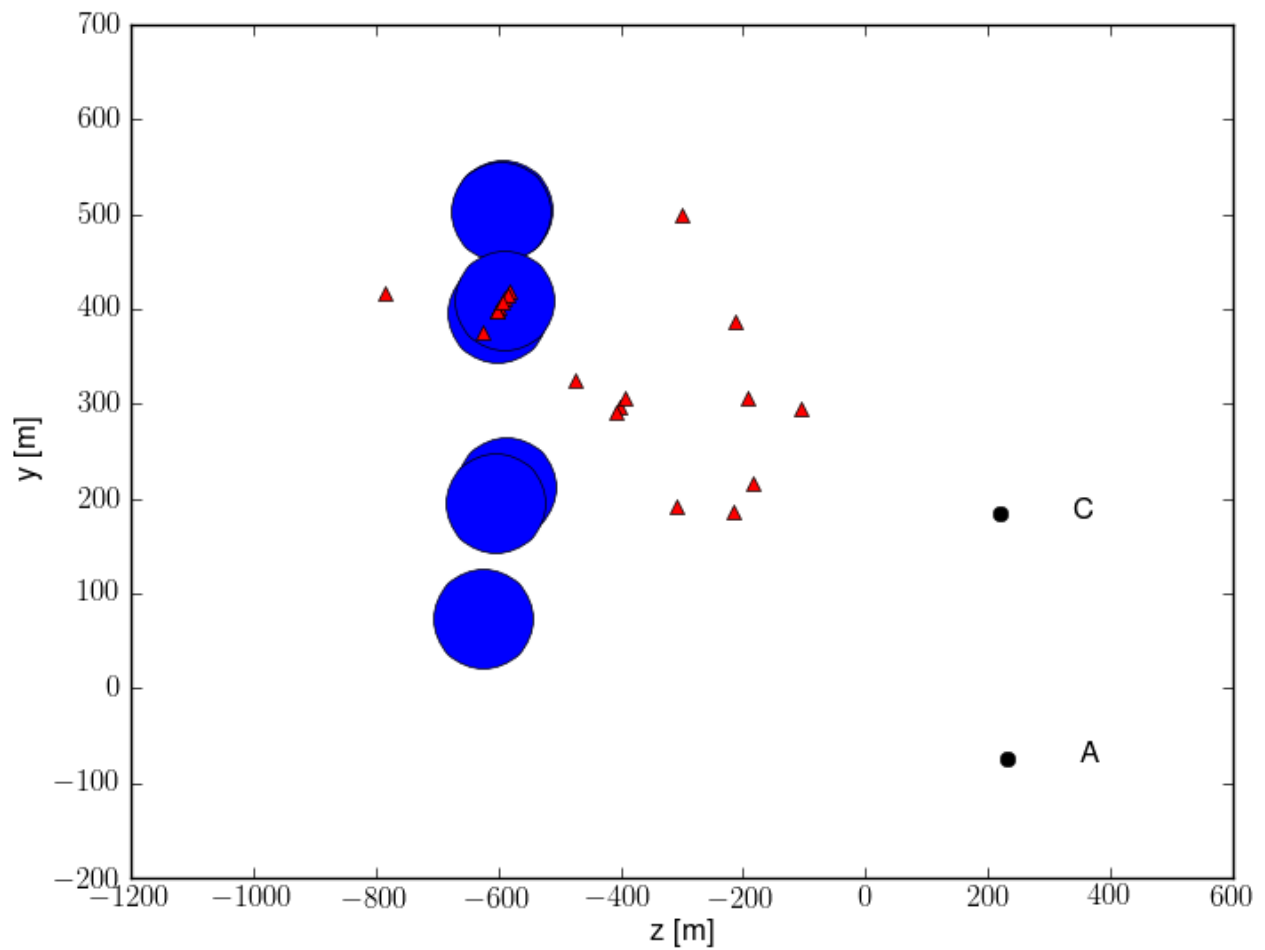


Figure 6.20: The inverted source locations using TR and constrained MT inversion in the  $yz$  - plane. 'A' and 'C' denote the location of the craters. The locations cluster in a region to the north-west of the crater region in a depth of 100 - 800 m.

## 6.5 Discussion

---

This study presents the results of a multi-component field campaign at Mt. Yasur, consisting of seismic and acoustic arrays, two Doppler radars and a infrared camera to monitor the on-going eruption. We apply a technique proposed by [Vidal \*et al.\* \(2006\)](#) to estimate the source volume of infrasound records. The results shows that the maximum particle velocity measured with the Doppler radar correlates nicely with the estimated slug lengths. [Tab. 6.3](#) gives an overview over the inverted events in the VLP frequency band (0.2 - 0.9 Hz). In contrast to the particle velocity, the inverted seismic moment could not be correlated with the estimated slug sizes, i.e. the slug size does not map in seismic moment. This is an important result, as it suggests that a large source volume not necessarily implies a stronger seismic source process. This is in some way confirming results of laboratory experiments by [Vidal \*et al.\* \(2006\)](#) suggesting that the radiated seismic and acoustic energy is rather dependent on the location and the characteristic timescale of the bubble rupturing process.

Furthermore, we obtained a ground velocity model for numerical simulations using a combination of seismic and Doppler radar data. The results from fk arrays analysis support the chosen parameters. The numerical simulations were performed with SeisSol, a high-order discontinuous Galerkin scheme. We successfully demonstrated the functionality of the TR method in a synthetic test. Following this, we located the source of VLP signals with TR for seven selected events. The inverted source volume shows a relatively large span of  $\sim 400$  m in every direction, nevertheless we observe a clustering to the north-west of the crater region in a depth of  $\sim 600$  m. It has to be mentioned that the estimation of the source depth is an extremely difficult task at Mt. Yasur due to the unfavorable flat topography and the small number of stations. Therefore, the given source depths can only be seen as a rough estimate. In a second inversion procedure, we used MT inversion to further constrain source position and mechanism. Again, we validated the method in a synthetic test case for frequencies up to 4 Hz. Subsequently, we performed an unconstrained inversion over the full grid space. The inverted mechanism was then kept fixed in a following constrained inversion around the previously estimated source position. The results support the source location north-west of the crater area predicted by TR ([Fig. 6.20](#)), the depth varies between 100 - 800 m. The found mechanisms represent an almost purely isotropic source. As [Lokmer \*et al.\* \(2009\)](#) pointed out, the inverted source time function is extremely sensitive to superficial velocity structure. This can cause a bias of the inverted mechanism and/or the inverted source position. The retrieved summed  $l_2$  misfits for a large part of the inverted events imply uncertainties in the used velocity model. However, we could show the found source mechanism is dominantly isotropic and that CLVD components can not be resolved by the data. We are aware of possible error sources that lie in the used velocity model, especially the thickness of the low-velocity layer and the velocity of the medium below can introduce biased results, i.e. introducing artificial isotropic components. Nevertheless, the found dominant isotropic component of the source mechanism seems to represent a stable feature. It is still under discussion what mechanism generates the VLP signals at depth and if the source depth represents the top of a magma

reservoir or changes in the conduit geometry. Unfortunately, our source inversion results prevent a confirmation of one of the proposed models, however, the relatively shallow source depths and the short rise times ( $< 10$  s) rather imply an interaction with the conduit geometry.

The activity at Mt. Yasur is currently produced from three craters (Oppenheimer *et al.*, 2006), where at the time the field campaign one (crater B) was only producing minor ash-venting. However, the results especially of MT inversion show no separation of events for the different craters which points to a common feeder system. This is supported by the results of a related study on the eruptive products (Kremers *et al.*, 2012b) that shows that the erupted products are chemically identical. Unfortunately, in this study no statement about the depth of a magma reservoir based on the analysis of melt inclusions or geothermobarometry could be made. Furthermore, seismic and acoustic records from the different craters point to a highly similar eruption mechanism, implying that the differences in recurrence time are controlled by the geometry of the shallow feeder system and/or variabilities in degassing and cooling rate.

event time	source location [m] (x, y, z)	mechanism [%] (iso, dc, clvd)	seismic moment [ $10^{13} Nm$ ]	$L_2$ misfit	AIC	stereographic projection
2008-27-08 19:00:28	(-150, 400, -300 )	(73, 21, 6 )	6.63	0.56	-260.61	
2008-27-08 19:01:50	(-350, 400, -300 )	(72, 3, 25 )	11.49	0.56	-256.45	
2008-27-08 19:04:26	(-150, 400, -300 )	(81, 17, 2 )	8.90	0.51	-347.22	
2008-27-08 19:04:55	(-150, 400, -300 )	(76, 16, 8 )	15.57	0.51	-334.73	
2008-27-08 19:07:35	(-250, 400, -300 )	(82, 8, 10 )	8.84	0.42	-520.69	
2008-27-08 19:08:34	(-150, 400, -300 )	(77, 20, 3 )	9.83	0.26	-947.50	
2008-27-08 19:09:14	(-250, 400, -300 )	(82, 7, 11 )	5.54	0.55	-272.44	
2008-27-08 19:18:40	(-350, 400, -300 )	(74, 3, 23 )	11.57	0.49	-375.24	
2008-27-08 19:19:53	(-150, 400, -300 )	(77, 17, 6 )	13.84	0.54	-289.60	
2008-27-08 19:22:22	(-150, 500, -300 )	(77, 8, 15 )	8.93	0.50	-357.63	
2008-27-08 19:25:18	(-350, 400, -100 )	(73, 26, 1 )	11.25	0.62	-170.18	
2008-27-08 19:28:23	(-350, 600, -400 )	(73, 26, 1 )	2.72	0.49	-378.54	

event time	source location [m] (x, y, z)	mechanism [%] (iso, dc, clvd)	seismic moment [ $10^{13}Nm$ ]	$L_2$ misfit	AIC	stereographic projection
2008-30-08 00:02:27	(-350, 400, -100)	(73, 12, 15)	26.61	0.37	-681.40	
2008-30-08 00:04:44	(-250, 400, -300)	(75, 17, 8)	5.03	0.58	-255.85	
2008-30-08 00:05:14	(-250, 400, -300)	(75, 14, 11)	6.58	0.59	-245.86	
2008-30-08 00:06:50	(-350, 400, -100)	(75, 16, 9)	20.45	0.51	-387.57	
2008-30-08 00:07:11	(-250, 400, -300)	(71, 22, 7)	5.60	0.62	-206.40	
2008-30-08 00:11:22	(-250, 400, -300)	(77, 17, 6)	7.38	0.61	-213.75	
2008-30-08 00:17:42	(-250, 300, -500)	(58, 18, 24)	3.58	0.56	-301.85	
2008-30-08 00:21:47	(-250, 400, -300)	(72, 22, 6)	2.84	0.51	-378.79	
2008-30-08 00:23:51	(-350, 400, -100)	(75, 14, 11)	28.57	0.62	-203.24	
2008-27-08 19:00:28	(-250, 400, -600)	(100,0,0)	8.99	0.58	-434.52	
2008-27-08 19:01:50	(-250, 400, -600)	(100,0,0)	19.21	0.58	-434.88	
2008-27-08 19:04:26	(-150, 300, -400)	(100,0,0)	11.05	0.50	-572.23	
2008-27-08 19:04:55	(-250, 400, -600)	(100,0,0)	18.39	0.55	-484.14	
2008-27-08 19:07:35	(-350, 300, -100)	(100,0,0)	6.13	0.42	-733.04	
2008-27-08 19:08:34	(-250, 400, -600)	(100,0,0)	14.57	0.26	-1141.99	
2008-27-08 19:09:14	(-350, 200, -200)	(100,0,0)	4.77	0.54	-498.29	
2008-27-08 19:18:40	(-250, 400, -600)	(100,0,0)	20.85	0.52	-531.28	
2008-27-08 19:19:53	(-150, 300, -400)	(100,0,0)	15.95	0.53	-512.07	
2008-27-08 19:22:22	(-250, 400, -600)	(100,0,0)	15.39	0.51	-574.42	
2008-27-08 19:25:18	(-350, 200, -300)	(100,0,0)	4.06	0.59	-428.84	
2008-27-08 19:28:23	(-250, 400, -600)	(100,0,0)	7.48	0.54	-503.35	
2008-30-08 00:02:27	(-450, 500, -300)	(100,0,0)	7.70	0.37	-905.58	
2008-30-08 00:04:44	(-250, 400, -600)	(100,0,0)	7.31	0.59	-451.35	
2008-30-08 00:05:14	(-250, 400, -600)	(100,0,0)	9.97	0.59	-463.01	
2008-30-08 00:06:50	(-250, 400, -200)	(100,0,0)	5.56	0.50	-606.43	
2008-30-08 00:07:11	(-250, 400, -800)	(100,0,0)	12.31	0.62	-406.59	
2008-30-08 00:11:22	(-350, 300, -500)	(100,0,0)	10.88	0.60	-437.52	
2008-30-08 00:17:42	(-250, 200, -200)	(100,0,0)	2.02	0.54	-540.84	
2008-30-08 00:21:47	(-150, 300, -400)	(100,0,0)	4.17	0.49	-626.72	
2008-30-08 00:23:51	(-450, 300, -200)	(100,0,0)	9.61	0.61	-424.73	

Table 6.3: The results of the *top*: unconstrained and *bottom*: constrained moment tensor inversion for 21 selected events in a frequency range from 0.2 - 0.9 Hz. Given are the picked event onset times, the inverted source location and mechanism, as well as the misfit and the Akaike Information Criterion (AIC, [Akaike, 1974](#)). The misfit is calculated as the sum of the  $l_2$ -norm of all three components, respectively. The last column shows the resulting fault plane solution. In the constrained inversion the mechanism is fixed to a purely isotropic source.



# 7

## Conclusions

This study presented the results of a comprehensive study including the eruptive behavior and products of Mt. Yasur from experimental volcanology, petrology and geophysical monitoring techniques. A link between these research fields allowed for a deepened understanding of the observed activity.

The results presented in chapters 2 and 3 deal with laboratory studies on explosive volcanic eruptions upon rapid decompression. Although the experiments were performed with a larger sample size ( $60 \times 60$  mm), the results verify previously observed trends (on smaller samples,  $25 \times 60$  mm in terms of fragmentation threshold, fragmentation speed and energy density by showing that these parameters are independent of sample size. This is an important result as it suggests that a scaling to large-scale processes is valid. In fact, the controlling parameter is found to be the setup-specific decompression rate. It has been shown before, that a precise determination of these values can deliver valuable insights into the explosive dynamics in nature (e.g., Spieler *et al.*, 2004; Scheu *et al.*, 2008). In chapter 3 the effect of changes in decompression rate were quantified. Introducing the normalized energy supply rate  $\psi$  allows to quantitatively compare the results of various sample sizes. It could be shown that the measured speed of fragmentation is heavily influenced by variations in decompression rate. Contrastingly, the particle velocity measured with a high-speed camera was found to be in good agreement with a model presented by Alatorre-Ibargüengoitia *et al.* (2010) using a different setup. This means that the speed of the erupted particles is not primarily dependent on the rate of decompression, but rather on the initially applied gas overpressure. A model is presented that correlates measured particle velocities to decompression rate and initial gas-overpressure. Using the measured maximum particle velocities at Volcán de Colima (Scharff *et al.*, 2011) and Mt. Yasur (Meier *et al.*, 2009) the

model estimates decompression rates in the order of  $0.4 - 2.4 \frac{GPa}{s}$ , which is at the upper end of previously suggested values (Toramaru, 2006). As the particle velocity is obviously not directly dependent on the eruptive mechanism, it is argued that this is a valid estimate not only for the fragmentation process at Volcán de Colima but also for the Strombolian bubble burst at Mt. Yasur. Furthermore, the interpretation of infrasound records allowed to estimate the length of the resonating cavity at Mt. Yasur, which believed to be an elongated gas bubble. Again applying the model yielded overpressures in the range of  $0.77 - 2.57 MPa$ , which is in the range of previously found values (Stromboli, Italy, Chouet *et al.*, 2003; Mt. Erebus, Antarctica, Gerst, 2010). The results show the importance of a thorough determination of the decompression rate in fragmentation experiments. The use of  $\psi$  allows to remove non-physical variations introduced by setup variations. Furthermore, it provides a powerful tool to correlate decompression rate to particle ejection velocity and initial gas overpressure.

In chapter 4 the Strombolian eruptive products at Mt. Yasur were petrographically and geochemically characterized. The samples are basaltic-andesite, which show regions with contrasting crystallinity and bubble-size distributions (bubble sizes of  $< 1 \cdot 10^{-3}$  and  $> 4 \cdot 10^{-2}$  mm). Furthermore, the juvenile bombs revealed bimodal textures; that is, they contain regions of microlite-free glass (sideromelane) and regions of microlite-rich groundmass. Thermal analysis of these juvenile products revealed the presence of a glass phase exhibiting a broad heat capacity plateau between 650 and 800 °C, further typified by double glass transition peaks, a feature that is not reported to have been observed before. The multiple peaks can be explained by the bimodal oxidation state of iron in an otherwise chemically homogeneous magma. This nature of the measured glass transitions is used to infer that mingling is rapid and thus accommodated in the shallow parts of eruptive conduits, perhaps due to rejuvenation of material slumped from the crater walls into an open conduit system.

The geophysical source localization part of the thesis is commenced by the study in chapter 5 on Time-reversal (TR) as a source imaging technique. It was found that TR imaging is well-suited to infer both the location and the timing of point sources. However, TR imaging in the used frequency range is not able to detect the details of finite rupture processes. Neither modifications of the receiver configuration (within reasonable bounds) nor the weighting of adjoint sources led to sufficient improvements. The dominant causes for this failure are the incomplete recording of wave field information at the surface, the presence of large-amplitude surface waves that deteriorate the depth resolution and the missing sink that should absorb energy radiated during the later stages of the rupture process. The results thus suggested that the limitations of TR imaging start where the source stops being point-localised.

Chapter 6 presents the results of the geophysical monitoring and source localization techniques performed on the Mt. Yasur dataset. Two distinct eruptive features at Mt. Yasur were presented, an ash-free and a ash-loaded eruption type. These distinct features were shown to generate highly non-similar acoustic signals, whereas especially the seismic

long-period (LP,  $f < 1$  Hz) signals remained unaffected. A technique proposed by Vidal *et al.* (2006) was applied to estimate the source volume of the radiated infrasound signals from fundamental resonance frequencies - similar to what was done in chapter 3. A correction for the estimated frequencies was applied following Meier *et al.* (2012). The results showed that the maximum particle velocity measured with the Doppler radar correlates nicely with the estimated slug lengths. The inverted seismic moment does not show any correlation with the estimated slug sizes, i.e. the slug size does not map in seismic moment. This is an important information, as it states that a larger source volume does not necessarily produces a larger seismic moment.

Following chapter 5 the TR imaging technique was applied to recorded signals in the LP and very long period (VLP,  $f < 0.1$  Hz) frequency band. The results supported the previous findings in the study on finite sources. It was possible to estimate a source volume with TR imaging in this frequency band, where the source is point-localized compared to the used wavelengths. The source location was found to be in the north-east section of the crater region at around 600 m depth. Unfortunately, the results allowed no assumption on the source mechanism. However, O'Brien *et al.* (2010) showed that the found solution can be clearly improved with the use of a higher station number or under the requirement of a more favourable topography than at Mt. Yasur. In second inversion technique, moment tensor (MT) inversion was performed using an algorithm developed by van Driel *et al.* (2012) to further constrain source location and mechanism. The found solution has a dominant isotropic part with small deviatoric components. In a second step a constrained inversion was performed that kept the source mechanism fixed to a purely isotropic mechanism. The results point to the model of an opening crack - a model that has been previously proposed for Strombolian type activity (e.g., Legrand *et al.*, 2000). As Lokmer *et al.* (2009) pointed out, the inverted source time function is extremely sensitive to superficial velocity structure. This can cause a biasing of the inverted mechanism and/or the found source position. The retrieved summed  $l_2$  misfits between observed and synthetic seismograms for a large part of the inverted events imply uncertainties in the used velocity model. However, the found source mechanisms seem to represent a stable feature, whereas the uncertainty in the source location is in the range of some hundred meters. A separation for events at different craters was not observed in both TR imaging and MT inversion, which points to a common feeder system.

**Main conclusions:** The results provided in this thesis support the following as the main conclusions:

1. The presented model based on laboratory fragmentation experiments and the normalized energy supply rate  $\psi$  allow a size-independent determination of parameters that are characterizing explosive volcanic eruptions, such as fragmentation threshold, fragmentation speed and energy density. Furthermore, the model provides a tool to correlate decompression rate to particle ejection velocity and initial gas overpres-

sure. The retrieved results have shown to be in the range of previously suggested values.

2. The petrological characterization of Mt. Yasurs eruptive products revealed a chemically homogeneous magma in all analyzed samples. The found differences in bubble distribution and especially the multiple glass transition peaks in the thermal analyses are believed to be caused by the bimodal iron oxidation state. This points to a shallow magma-mingling process due to rejuvenation of material slumped from the crater walls into an open conduit system.
3. The results on the TR imaging of finite sources illustrate that it is not able to detect the details of finite rupture processes (in the long-period range). Effectively, it is suggested that the limitations of the method begin where the source stops being point-localized, with respect to the used frequencies.
4. At Mt. Yasur the source of LP to VLP signals is located with the TR imaging method. As pointed out above, no information about the source mechanism could be retrieved. Using MT inversion, the source mechanism is inverted as representing an opening crack or a purely volumetric source. The source is found to be located in the north-east section of the crater area at 600 – 800 m depth, which validates the results of TR imaging. The uncertainty in the location is estimated as a few hundred meters, caused by uncertainties in the used velocity model. A correlation between the inverted seismic moment and the previously estimated slug sizes could not be found. As no differences in the seismic signals and inversion results between events at different craters could be observed, we assume that the active craters at Mt. Yasur share a common feeder system.

## 7.1 Model for Strombolian activity at Mt. Yasur

---

Combining the results of all presented studies the following model for explosive Strombolian eruptions at Mt. Yasur is proposed:

A common feeder system for all active craters at Mt. Yasur is suggested Fig. 7.1. This is supported by the results of TR imaging and MT inversion, as well as the homogeneity of the eruptive products of craters A and C. The differences in event recurrence rate are believed to be controlled by either the conduit geometry or variations in degassing or cooling rate. The multiple glass transition peaks in the thermal analyses point to a shallow magma-mingling process due to rejuvenation of material slumped from the crater walls

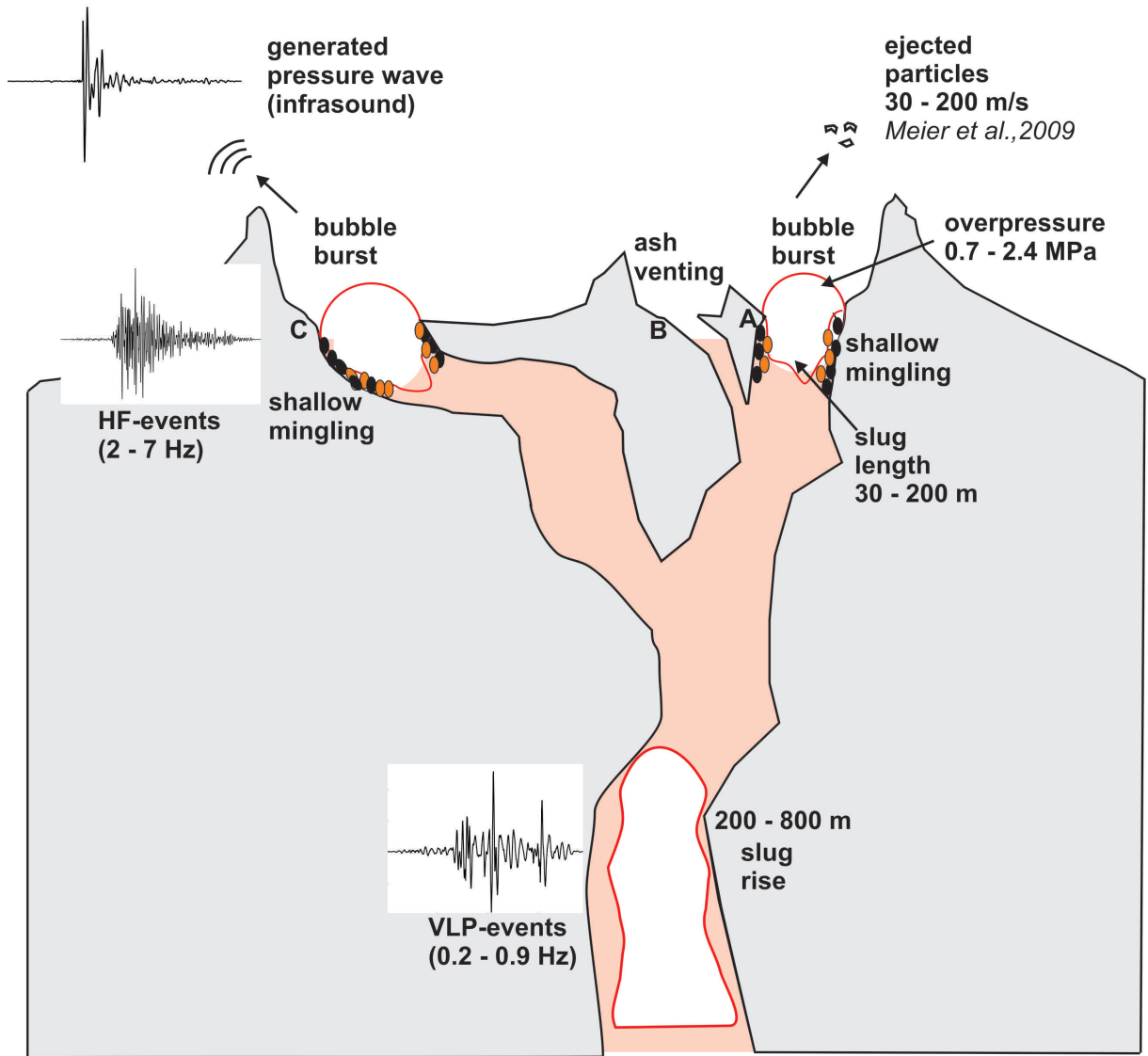


Figure 7.1: Sketch illustrating the proposed model for the Strombolian activity at Mt. Yasur volcano using the combined results of the different disciplines and analysis techniques.

into an open conduit system. This process is highly likely to contribute to the observed distinct eruptive features, namely ash-free and ash-loaded eruptions. Based on laboratory experiments and the recorded acoustic signals, most eruptions at Mt. Yasur are due to the burst of gas slugs with lengths of 40 – 180 m that have achieved an effective overpressure of up to 2.5 MPa.

The results illustrate the importance of combined studies that overcome the limitations of single disciplines. In this way, a more comprehensive view of volcanic eruptions and the associated observations is possible. Such a multi-disciplinary approach will contribute to a better understanding of volcanic processes and the associated hazards.

## References

- Abràmoff, M. D., Hospitals, I., and Magalhães, P. J.** (2004). Image Processing with ImageJ. *Medicine*, **11**(7), 36–42. [3.3.3](#)
- Akaike, H.** (1974). A new look at the statistical model identification. *Automatic Control, IEEE Transactions on*, **19**(6), 716 – 723. [6.4.3](#), [6.3](#)
- Aki, K.** (1957). Space and time spectra of stationary stochastic waves, with special reference to microtremors. *Bull. Earthq. Res. Inst.*, **35**, 415 – 456. [6.3](#)
- Alatorre-Ibargüengoitia, M. A., Scheu, B., Dingwell, D., Delgado-Granados, H., and Taddeucci, J.** (2010). Energy consumption by magmatic fragmentation and pyroclast ejection during Vulcanian eruptions. *Earth and Planetary Science Letters*, **291**(1-4), 60–69. [1](#), [3.2](#), [3.5.3](#), [3.4](#), [3.8](#), [7](#)
- Alatorre-Ibargüengoitia, M. A., Scheu, B., and Dingwell, D.** (2011). Influence of the fragmentation process on the dynamics of Vulcanian eruptions: An experimental approach. *Earth and Planetary Science Letters*, **302**(1-2), 51–59. [3.2](#), [3.5.3](#), [3.7](#), [3.7](#), [3.7](#), [3.7](#)
- Alidibirov, M. and Dingwell, D.** (1996a). An experimental facility for the investigation of magma fragmentation by rapid decompression. *Bulletin of Volcanology*, **58**, 411–416. [1.2](#), [2.2](#), [2.4](#), [3.2](#)
- Alidibirov, M. and Dingwell, D.** (1996b). High temperature fragmentation of magma by rapid decompression. *Nature*, **380**, 146–149. [1](#), [1.2](#), [2.2](#), [2.4](#), [3.2](#)
- Alidibirov, M. and Dingwell, D.** (2000). Three fragmentation mechanisms for highly viscous magma under rapid decompression. *Journal of Volcanology and Geothermal Research*, **100**, 413–421. [2.4](#), [3.2](#)
- Allen, S. R.** (2005). Complex spatter- and pumice-rich pyroclastic deposits from an andesitic caldera-forming eruption : the Siwi pyroclastic sequence, Tanna, Vanuatu. *Bull Volcanol*, **67**, 27–41. [6.2](#), [6.3](#)
- Allmann, B. P. and Shearer, P. M.** (2007). A high-frequency secondary event during the 2004 Parkfield earthquake. *Science (New York, N. Y.)*, **318**(5854), 1279–83. [5.2](#), [6.4.2](#)

- Artman, B., Podladtchikov, I., and Witten, B. (2010). Source location using time-reverse imaging. *Geophysical Prospecting*, **58**(5), 861–873. [5.2](#)
- Aster, R., Mah, S., Kyle, P., McIntosh, W., Dunbar, N., Johnson, J., and Ruiz, M. (2003). Very long period oscillations of Mount Erebus Volcano. *Journal of Geophysical Research*, **108**(B11), 2522. [1](#), [6.2](#), [6.4.2](#)
- Aster, R., Zandomenighi, D., Mah, S., Mcnamara, S., Henderson, D. B., Knox, H., and Jones, K. (2009). Moment tensor inversion of very long period seismic signals from Strombolian eruptions of Erebus Volcano. *Journal of Volcanology and Geothermal Research*, **177**(3), 635–647. [1](#)
- Bagdassarov, N., Dingwell, D., and Webb, S. (1994). Viscoelasticity of crystal- and bubble-bearing rhyolite melts. *Physics of the Earth and Planetary Interiors*, **83**(2), 83–99. [4.2](#)
- Bani, P. and Lardy, M. (2007). Sulphur dioxide emission rates from Yasur volcano, Vanuatu archipelago. *Geophysical Research Letters*, **34**, L20309, doi:10.1029/2007GL030411. [1.1](#), [1.2](#), [4.3](#), [6.2](#)
- Bani, P., Oppenheimer, C., Allard, P., Shinohara, H., Tsanev, V., Carn, S., Lardy, M., and Garaebiti, E. (2011). First estimate of volcanic SO<sub>2</sub> budget for Vanuatu island arc. *Journal of Volcanology and Geothermal Research*, **211**, 36–46. [1.1](#)
- Barsch, R. (2009). *Web-based technology for storage and processing of multi-component data in seismology First steps towards a new design*. Dissertation, LMU Munich. [6.3](#)
- Bean, C. J., Lokmer, I., and Brien, G. O. (2008). Influence of near-surface volcanic structure on long-period seismic signals and on moment tensor inversions : Simulated examples from Mount Etna. *Journal of Geophysical Research*, **113**(B08308), 1–19. [1](#), [6.2](#), [6.3](#), [6.3](#), [6.4.3](#), [6.4.3](#)
- Begét, J. E. (2000). Volcanic Tsunamis. *Encyclopedia of Volcanoes*, Seiten 1005–1013. [1](#)
- Behncke, B. and Neri, M. (2003). The July–August 2001 eruption of Mt. Etna (Sicily). *Bulletin of Volcanology*, **65**, 461–476. [1](#)
- Belousov, A. (1996). Deposits of the 30 March 1956 directed blast at Bezymianny volcano, Kamchatka, Russia. *Bulletin of Volcanology*, **57**, 649–662. [1](#)
- Beyreuther, M., Barsch, R., Krischer, L., Megies, T., Behr, Y., and Wassermann, J. (2010). ObsPy: A Python Toolbox for Seismology. *Seismological Research Letters*, **81**(3), 530–533. [5.6](#), [6.3](#)

- Blackburn, E., Wilson, L., and Sparks, R.** (1976). Mechanics and dynamics of Strombolian activity. *J. Geol. Soc. London*, **132**, 429–440. [4.2](#), [5.8](#), [6.2](#)
- Bohlen, T. and Saenger, E. H.** (2006). Accuracy of heterogeneous staggered-grid finite-difference modeling of Rayleigh waves. *Geophysics*, **71**(4), 109–115. [6.3](#)
- Bouhifd, M., Richet, P., Besson, P., Roskosz, M., and Ingrin, J.** (2004). Redox state, microstructure and viscosity of a partially crystallized basalt melt. *Earth and Planetary Science Letters*, **218**(1-2), 31–44. [4.2](#), [4.5](#)
- Bunge, H.-P., Hagelberg, C. R., and Travis, B. J.** (2003). Mantle circulation models with variational data assimilation: inferring past mantle flow and structure from plate motion histories and seismic tomography. *Geophysical Journal International*, **152**(2), 280–301. [5.2](#)
- Caricchi, L., Burlini, L., Ulmer, P., Gerya, T., Vassalli, M., and Papale, P.** (2007). Non-Newtonian rheology of crystal-bearing magmas and implications for magma ascent dynamics. *Earth and Planetary Science Letters*, **264**(3-4), 402–419. [4.2](#)
- Carignan, J., Hild, P., Mevelle, G., Morel, J., and Yeghicheyan, D.** (2001). Routine Analyses of Trace Elements in Geological Samples using Flow Injection and Low Pressure On-Line Liquid Chromatography Coupled to ICP-MS : A Study of Geochemical Reference Materials BR, DR-N, UB-N, AN-G and GH. *Geostandards Newsletter*, **25**, 187–198. [4.8.3](#)
- Carney, J. and Macfarlane, A.** (1979). *Geology of Tanna, Aneityum, Futuna and Aniwa*. New Hebrides Government, regional r edition. [1.1](#), [4.3](#), [6.2](#), [6.3](#)
- Cashman, K., Sturtevant, B., Papale, P., and Navon, O.** (2000). *Magmatic fragmentation*, in: *Encyclopedia of Volcanoes*. Sigurdsson, H., Academic Press, San Diego. [1.2](#)
- Cesca, S., Heimann, S., Stammler, K., and Dahm, T.** (2010). Automated procedure for point and kinematic source inversion at regional distances. *Journal of Geophysical Research*, **115**(B6), B06304. [5.2](#)
- Chakroun, N., Fink, M., and Wu, F.** (1995). Time reversal processing in ultrasonic nondestructive testing. *IEEE Transactions on Ultrasonics, Ferroelectrics and Frequency Control*, **42**(6), 1087–1098. [5.2](#), [6.4.2](#)
- Chaljub, E., Moczo, P., Tsuno, S., Bard, P.-Y., Kristek, J., Käser, M., Stupazzini, M., and Kristekova, M.** (2010). Quantitative Comparison of Four Numerical Predictions of 3{D} Ground Motion in the Grenoble Valley, France. *Bull. Seis. Soc. Am.*, **100**(4), 1427–1455. [6.3](#)

- Chapman, C. H. and Leaney, W. S.** (2012). A new moment-tensor decomposition for seismic events in anisotropic media. *Interpreting*, **188**, 343–370. [6.4.3](#), [6.18](#)
- Chen, J. K., Taylor, F. W., Edwards, R. L., Cheng, H., and Burr, G. S.** (1995). Recent Emerged Reef Terraces of the Yenkahe Resurgent Block, Tanna, Vanuatu: Implications for Volcanic, Landslide and Tsunami Hazards. *The Journal of Geology*, **103**(5), 577–590. [1.1](#), [4.3](#), [6.2](#), [6.3](#)
- Chouet, B.** (1994). Precursory swarms of long-period events at Redoubt Volcano (1989/1990), Alaska: Their origin and use as a forecasting tool. *Journal of Volcanology and Geothermal Research*, **62**(1-4), 95–135. [1](#), [6.2](#)
- Chouet, B.** (1996). Long-period volcano seismicity: its source and use in eruption forecasting. *Nature*, **380**, 309–316. [1](#), [6.2](#)
- Chouet, B.** (2003). Volcano Seismology. *Pure and Applied Geophysics*, **160**(3), 739–788. [3.9.2](#), [5.8](#), [6.2](#)
- Chouet, B., Dawson, P., Ohminato, T., Martini, M., Saccorotti, G., Giudicepietro, F., De Luca, G., Milana, G., and Scarpa, R.** (2003). Source mechanisms of explosions at Stromboli Volcano, Italy, determined from moment-tensor inversions of very-long-period data. *Journal of Geophysical Research*, **108**(B1, 2019), 1 – 25. [1](#), [3.7.1](#), [3.8](#), [4.2](#), [6.2](#), [6.4.2](#), [6.4.3](#), [7](#)
- Christensen, N.** (1996). Poisson ' s ratio and crustal seismology. *Journal of Geophysical Research*, **101**(B2), 3139–3156. [6.3](#)
- Cole, P. D., Fernandez, E., Duarte, E., and Duncan, A. M.** (2005). Explosive activity and generation mechanisms of pyroclastic flows at Arenal volcano, Costa Rica between 1987 and 2001. *Bulletin of Volcanology*, **67**(8), 695–716. [3.9.2](#), [4.3](#)
- Cordonnier, B., Hess, K.-U., Lavallée, Y., and Dingwell, D.** (2009). Rheological properties of dome lavas: Case study of Unzen volcano. *Earth and Planetary Science Letters*, **279**(3-4), 263–272. [4.2](#)
- Cordonnier, B., Schmalholz, S. M., Hess, K.-U., and Dingwell, D. B.** (2012). Viscous heating in silicate melts : An experimental and numerical comparison. *Journal of Geophysical Research*, **117**(B02203), 1–13. [4.2](#)
- Cotton, F. and Campillo, M.** (1995). Frequency domain inversion of strong motions: Application to the 1992 Landers earthquake. *Journal of Geophysical Research*, **100**(83), 3961–3975. [5.2](#)
- Dehn, J., Dean, K. G., and Engle, K.** (2002). Thermal precursors in satellite images of the 1999 eruption of Shishaldin Volcano. *Bulletin of Volcanology*, **64**, 525–534. [1](#)

- Derode, A., Roux, P., and Fink, M.** (1995). Robust Acoustic Time Reversal with High-Order Multiple Scattering. *Physical Review Letters*, **75**(23), 4206–4209. [5.2](#)
- Dingwell, D.** (1989). Shear viscosities of ferrosilicate liquids. *American Mineralogist*, **74**, 1038–1044. [4.8.7](#)
- Dingwell, D.** (1991). Redox viscometry of some Fe-bearing silicate melts. *American Mineralogist*, **76**, 1560–1562. [4.2](#)
- Dingwell, D.** (1996). Volcanic Dilemma—Flow or Blow? *Science*, **273**(5278), 1054–1055. [4.2](#)
- Dingwell, D.** (1998). Melt viscosity and diffusion under elevated pressures. *Reviews in Mineralogy and Geochemistry*, **37**, 397–424. [1](#), [4.2](#)
- Dingwell, D.** (2006). Transport Properties of Magmas: Diffusion and Rheology. *ELEMENTS*, **2**(5), 281 – 286. [3.9.2](#), [4.2](#)
- Dingwell, D.** (2007). *Diffusion, viscosity and flow of melts*. Elsevier, Amsterdam, mineral ph edition. [4.2](#)
- Dingwell, D. and Virgo, D.** (1987). The effect of oxidation state on the viscosity of melts in the system Na<sub>2</sub>O-FeO-Fe<sub>2</sub>O<sub>3</sub>-SiO<sub>2</sub>. *Geochimica et Cosmochimica Acta*, **51**(2), 195–205. [4.8.7](#)
- Dingwell, D., Hess, K.-U., and Knoche, R.** (1996). Granite and granitic pegmatite melts: Volumes and viscosities. *Transactions of the Royal Society of Edinburgh—Earth Sciences*, **87**, 65–72. [1](#)
- Dingwell, D., Hess, K.-U., and Romano, C.** (1998). Extremely fluid behavior of hydrous peralkaline rhyolites. *Earth and Planetary Science Letters*, **158**(1-2), 31–38. [4.2](#)
- Dreier, R., Widmer, R., Schick, R., and Zürn, W.** (1994). Stacking of broadband seismograms of shocks at Stromboli. *Acta Vulcanol.*, **5**, 165–172. [6.2](#)
- Dumbser, M. and Käser, M.** (2006). An Arbitrary High Order Discontinuous {G}alerkin Method for Elastic Waves on Unstructured Meshes {II}: The Three-Dimensional Case. *Geophys. J. Int.*, **167**(1), 319–336. [6.2](#), [6.3](#)
- Edelmann, G., Akal, T., Hodgkiss, W., and Kuperman, W.** (2002). An initial demonstration of underwater acoustic communication using time reversal. *IEEE Journal of Oceanic Engineering*, **27**(3), 602–609. [5.2](#)
- Fichtner, A.** (2010). Full seismic waveform modelling and inversion. *Springer, Heidelberg*. [5.2](#), [5.2](#)

- Fichtner, A. and Igel, H.** (2008). Efficient numerical surface wave propagation through the optimization of discrete crustal models—a technique based on non-linear dispersion curve matching (DCM). *Geophysical Journal International*, **173**(2), 519–533. [5.3](#)
- Fichtner, A., Bunge, H., and Igel, H.** (2006). The adjoint method in seismology I. Theory. *Physics of The Earth and Planetary Interiors*, **157**(1-2), 86–104. [5.2](#)
- Fichtner, A., Kennett, B. L. N., Igel, H., and Bunge, H.-P.** (2009a). Full seismic waveform tomography for upper-mantle structure in the Australasian region using adjoint methods. *Geophysical Journal International*, **179**(3), 1703–1725. [5.3](#)
- Fichtner, A., Igel, H., Bunge, H.-P., and Kennett, B.** (2009b). Simulation and Inversion of Seismic Wave Propagation on Continental Scales Based on a Spectral-Element Method. *Journal of Numerical Analysis, Industrial and Applied Mathematics*, **4**, 11–22. [5.3](#)
- Fink, M.** (1996). Time reversal in acoustics. *Contemporary Physics*, **37**(2), 95–109. [5.2](#)
- Fink, M.** (1997). Time reversed acoustics. *Physics Today*, **50**(3), 34–40. [5.2](#), [6.4.2](#)
- Fink, M. and Tanter, M.** (2010). Multiwave imaging and super resolution. *Physics Today*, **63**(2), 28–33. [5.2](#), [6.4.2](#)
- Fowler, A. C., Scheu, B., Lee, W. T., and McGuinness, M. J.** (2009). A theoretical model of the explosive fragmentation of vesicular magma. *Proceedings of the Royal Society A: Mathematical, Physical and Engineering Sciences*, **466**(2115), 731–752. [2.4](#)
- Gajewski, D. and Tessmer, E.** (2005). Reverse modelling for seismic event characterization. *Geophys. J. Int.*, **163**, 276–284 doi:10.1111/j.1365-246X.2005.02732.x. [5.2](#), [6.4.2](#)
- Gerst, A.** (2010). *The First Second of a Strombolian Volcanic Eruption*. Dissertation, University of Hamburg. [3.7.1](#), [3.8](#), [6.2](#), [7](#)
- Gerst, A., Hort, M., Kyle, P. R., and Vöge, M.** (2008). 4D velocity of Strombolian eruptions and man-made explosions derived from multiple Doppler radar instruments. *Journal of Volcanology and Geothermal Research*, **177**(3), 648–660. [1](#)
- Giordano, D., Romano, C., Papale, P., and Dingwell, D.** (2004). The viscosity of trachytes, and comparison with basalts, phonolites, and rhyolites. *Chemical Geology*, **213**(1-3), 49–61. [1](#)
- Giordano, D., Russell, J. K., and Dingwell, D.** (2008). Viscosity of magmatic liquids: A model. *Earth and Planetary Science Letters*, **271**(1-4), 123–134. [4.2](#)

- Giuli, G., Paris, E., Hess, K.-U., Dingwell, D., Cicconi, M. R., Eeckhout, S. G., Fehr, K. T., and Valenti, P. (2011). XAS determination of the Fe local environment and oxidation state in phonolite glasses. *American Mineralogist*, **96**(4), 631–636. [4.8.8](#)
- Gottsmann, J. and Dingwell, D. (2000). Supercooled diopside melt: confirmation of temperature-dependent expansivity using container-based dilatometry. *Contributions to Mineralogy and Petrology*, **139**(2), 127–135. [4.5](#)
- Govindaraju, K. (1995). 1995 working values with confidence limits for twenty-six CRPG, ANRT and IWG-GIT geostandards. *Geostandards Newsletter*, **19**, 1–32. [4.8.3](#)
- Graves, R. W. and Wald, D. J. (2001). 3D Seismic Resolution Analysis of Finite Fault Source Inversion Using 1D and 3D Green’s Functions, Part I: Strong Motions. *Journal of Geophysical Research*, **106**(B5), 8745 – 8766. [6.4.3](#)
- Harris, A. and Ripepe, M. (2007). Synergy of multiple geophysical approaches to unravel explosive eruption conduit and source dynamics A case study from Stromboli. *Chemie der Erde - Geochemistry*, **67**(1), 1–35. [1](#)
- Harris, A., Dehn, J., Patrick, M., Calvari, S., Ripepe, M., and Lodato, L. (2005). Lava effusion rates from hand-held thermal infrared imagery : an example from the June 2003 effusive activity at Stromboli. *Bulletin of Volcanology*, **68**, 107–117. [1](#)
- Hess, K.-U. and Dingwell, D. (1996). Viscosities of hydrous leucogranitic melts: A non-Arrhenian model. *American Mineralogist*, **81**, 1297–1300. [4.2](#)
- Hjörleifsdóttir, V. (2007). *Earthquake source characterization using 3D Numerical Modeling*. Dissertation, California Institute of Technology, Pasadena, California, USA. [5.2](#)
- Horwell, C. J. and Baxter, P. J. (2006). The respiratory health hazards of volcanic ash: a review for volcanic risk mitigation. *Bulletin of Volcanology*, **69**, 1–24. [1](#)
- Houghton, B. and Gonnermann, H. (2008). Basaltic explosive volcanism: Constraints from deposits and models. *Chemie der Erde - Geochemistry*, **68**(2), 117–140. [3.9.2](#)
- Hui, H. and Zhang, Y. (2007). Toward a general viscosity equation for natural anhydrous and hydrous silicate melts. *Geochimica et Cosmochimica Acta*, **71**(2), 403–416. [4.2](#)
- Hürlimann, M., Turon, E., and Marti, J. (1999). Large Landslides Triggered by Caldera Collapse Events in Tenerife, Canary Islands. *Phys. Chem. Earth (A)*, **24**(10), 921–924. [1](#)
- Ichihara, M., Rittel, D., and Sturtevant, B. (2002). Fragmentation of a porous viscoelastic material: Implications to magma fragmentation. *Journal of Geophysical Research - Solid Earth*, **107**(B10), 2229. [1](#), [1.2](#), [2.2](#), [2.6](#), [3.2](#), [3.6.1](#)

- Ishibashi, H.** (2009). Non-Newtonian behavior of plagioclase-bearing basaltic magma: Subliquidus viscosity measurement of the 1707 basalt of Fuji volcano, Japan. *Journal of Volcanology and Geothermal Research*, **181**(1-2), 78–88. [4.2](#)
- Ishii, M., Shearer, P. M., Houston, H., and Vidale, J. E.** (2005). Extent, duration and speed of the 2004 Sumatra-Andaman earthquake imaged by the Hi-Net array. *Nature*, **435**(7044), 933–6. [5.2](#)
- James, M. R., Lane, S. J., Chouet, B., and Gilbert, J. S.** (2004). Pressure changes associated with the ascent and bursting of gas slugs in liquid- called vertical and inclined conduits. *Journal of Volcanology and Geothermal Research*, **129**. [1](#), [5.8](#), [6.2](#)
- James, M. R., Lane, S. J., and Chouet, B.** (2006). Gas slug ascent through changes in conduit diameter: Laboratory insights into a volcano-seismic source process in low-viscosity magmas. *Journal of Geophysical Research*, **111**(B5), 1–25. [1](#), [6.2](#)
- James, M. R., Lane, S. J., and Corder, S. B.** (2008). Modelling the rapid near-surface expansion of gas slugs in low-viscosity magmas. *Geological Society, London, Special Publications*, **307**(1), 147–167. [4.2](#)
- Jaupart, C. and Vergnolle, S.** (1989). The generation and collapse of a foam layer at the roof of a basaltic magma chamber. *Journal of Fluid Mechanics*, **203**, 347–380. [5.8](#), [6.2](#)
- Jentzsch, G., Punongbayan, R. S., Schreiber, U., Seeber, G., Völksen, C., and Weise, A.** (2001). Mayon volcano , Philippines : change of monitoring strategy after microgravity and GPS measurements from 1992 to 1996. *Journal of Volcanology and Geothermal Research*, **109**, 219–234. [1](#)
- Johnson, J.** (2003). Interpretation and utility of infrasonic records from erupting volcanoes. *Journal of Volcanology and Geothermal Research*, **121**(1-2), 15–63. [5.8](#), [6.2](#)
- Kameda, M., Kuribara, H., and Ichihara, M.** (2005). Dominant time scale for brittle fragmentation of vesicular magma by decompression. *Geophysical Research Letters*, **35**(14). [2.6](#)
- Kameda, M., Kuribara, H., and Ichihara, M.** (2008). Dominant time scale for brittle fragmentation of vesicular magma by decompression. *Geophysical Research Letters*, **35**(14), 2–5. [1](#), [3.2](#), [3.6.1](#)
- Käser, M. and Dumbser, M.** (2006). An arbitrary high-order discontinuous Galerkin method for elastic waves on unstructured meshes - I. The two-dimensional isotropic case with external source terms. *Geophys. J. Int.*, **166**(2), 855–877, doi:10.1111/j.1365–246X.2006.03051.x. [5.5.1](#)

- Kawakatsu, H., Kaneshima, S., Matsubayashi, H., Ohminato, T., and Sudo, Y.** (2000). Aso94 : Aso seismic observation with broadband instruments. *Journal of Volcanology and Geothermal Research*, **101**, 129–154. [1](#), [6.2](#)
- Kennedy, B., Spieler, O., Scheu, B., Kueppers, U., Taddeucci, J., and Dingwell, D. B.** (2005). Conduit implosion during Vulcanian eruptions. *Geology*, **33**(7), 581–584. [1](#), [1.2](#), [2.2](#), [2.6](#), [3.2](#), [3.5.2](#)
- Kennett, B. L. N.** (1983). A new way to estimate seismic source parameters. *Nature*, **302**, 659–660. [5.2](#)
- Kieffer, S. W.** (1977). Sound Speed in Liquid-Gas Mixtures' Water-Air and Water-Steam. *Journal of Geophysical Research*, **82**(20), 2895–2904. [3.7.1](#)
- Kieffer, S. W. and Sturtevant, B.** (1984). Laboratory Studies of Volcanic Jets. *Journal of Geophysical Research*, **89**(B10), 8253–8268. [2.6](#)
- Kirchdörfer, M.** (1999). Analysis and quasistatic FE modeling of long period impulsive events associated with explosions at Stromboli volcano (Italy). *Annals of Geophysics*, **42**(3), 379–390. [6.2](#)
- Kling, G. W., Evans, W. C., Tanyileke, G., Kusakabe, M., Ohba, T., Yoshida, Y., and Hell, J. V.** (2005). Degassing Lakes Nyos and Monoun: Defusing certain disaster. *PNAS*, **102**, 14185–14190. [1](#)
- Kokelaar, B. P.** (2002). Setting, chronology and consequences of the eruption of Soufrière Hills Volcano, Montserrat (1995-1999). *DRUITT, T.H. and KOKELAAR, B.P.(eds) 2002. The eruption of Soufrière Hills Volcano, Montserrat, from 1995 to 1999. Geological Society, London, Memoirs*, **21**, 1–21. [1](#)
- Konstantinou, K. I.** (2002). Deterministic non-linear source processes of volcanic tremor signals accompanying the 1996 Vatnajökull eruption, central Iceland. *Geophysical Journal International*, **148**, 663–675. [1](#), [6.2](#)
- Koyaguchi, T., Scheu, B., Mitani, N., and Melnik, O.** (2008). A fragmentation criterion for highly viscous bubbly magmas estimated from shock tube experiments. *Journal of Volcanology and Geothermal Research*, **178**(1), 58–71. [1.2](#), [3.5.1](#)
- Kremers, S., Scheu, B., Cordonnier, B., Spieler, O., and Dingwell, D.** (2010). Influence of decompression rate on fragmentation processes: An experimental study. *Journal of Volcanology and Geothermal Research*, **193**(3-4), 182–188. [1.2](#), [3.2](#), [3.3](#), [3.5.2](#), [3.6.1](#)
- Kremers, S., Fichtner, A., Brietzke, G. B., Igel, H., Larmat, C., and Huang, L.** (2011). Exploring the potentials and limitations of the time-reversal imaging of finite seismic sources. *Solid Earth*, **2**, 95–105. [1.2](#), [6.4.2](#), [6.4.2](#)

- Kremers, S., Barsu, S., Scheu, B., and Dingwell, D. (2012a). Decompression rate controls on explosive volcanic eruptions (working title). *submitted to Bulletin of Volcanology*. 1.2
- Kremers, S., Hanson, J., Lavallée, Y., Hess, K.-U., Chevrel, O., Wassermann, J., and Dingwell, D. B. (2012b). Shallow magma-mingling-driven Strombolian eruptions at Mt. Yasur volcano, Vanuatu. *submitted to GRL*. 1.2, 3.1, 3.4.3, 3.7.1, 3.9.2, 6.2, 6.3, 6.5
- Kremers, S., Wassermann, J., Meier, K., Pelties, C., van Driel, M., Vasseur, J., and Hort, M. (2012c). The source of Strombolian bubble bursts at Mt. Yasur, Vanuatu. *submitted to Journal of Volcanology and Geothermal Research*. 1.2
- Kueppers, U., Scheu, B., Spieler, O., and Dingwell, D. B. (2006). Fragmentation efficiency of explosive volcanic eruptions: A study of experimentally generated pyroclasts. *Journal of Volcanology and Geothermal Research*, **153**, 125–135. 1, 1.2, 2.2
- Kueppers, U., Meier, K., Kremers, S., Scheu, B., Alatorre-Ibargüengoitia, M. A., Taddeucci, J., and Dingwell, D. (2012). Waakiki - combining laboratory experiments with field monitoring techniques. *in preparation*. 3.4
- Lacoss, R. T., Kelly, E. J., and Toksoz, M. N. (1969). Estimation of seismic noise structure using arrays. *Geophysics*, **34**(1), 21–36. 6.3
- Larmat, C., Montagner, J.-P., Fink, M., Capdeville, Y., Tourin, A., and Clévéde, E. (2006). Time-reversal imaging of seismic sources and application to the great Sumatra earthquake. *Geophysical Research Letters*, **33**(19), L19312. 5.2, 6.4.2
- Larmat, C., Tromp, J., Liu, Q., and Montagner, J.-P. (2008). Time reversal location of glacial earthquakes. *J. Geophys. Res.*, **113**(B09314). 6.4.2
- Larmat, C., Guyer, R., and Johnson, P. (2009). Tremor source location using time reversal: Selecting the appropriate imaging field. *Geophysical Research Letters*, **36**(22), L22304. 5.2, 6.4.2
- Lautze, N. and Houghton, B. (2005). Physical mingling of magma and complex eruption dynamics in the shallow conduit at Stromboli volcano, Italy. *Geology*, **33**(5), 425. 1, 3.9.2, 4.2, 4.4
- Lautze, N. and Houghton, B. (2006). Linking variable explosion style and magma textures during 2002 at Stromboli volcano, Italy. *Bulletin of Volcanology*, **69**(4), 445–460. 1, 3.9.2, 4.2
- Lautze, N. and Houghton, B. (2008). Single explosions at Stromboli in 2002: Use of clast microtextures to map physical diversity across a fragmentation zone. *Journal of Volcanology and Geothermal Research*, **170**(3-4), 262–268. 3.9.2, 4.2

- Lavallée, Y., Hess, K.-U., Cordonnier, B., and Dingwell, D. B. (2007). Non-Newtonian rheological law for highly crystalline dome lavas. *Geology*, **35**(9), 843–846. [1](#), [4.2](#)
- Lavallée, Y., Varley, N. R., Alatorre-Ibargüengoitia, M. A., Hess, K.-U., Kueppers, U., Mueller, S., Richard, D., Scheu, B., Spieler, O., and Dingwell, D. B. (2011). Magmatic architecture of dome-building eruptions at Volcán de Colima, Mexico. *Bulletin of Volcanology*, Seiten 249–260. [3.7.1](#)
- Lavigne, F., Thouret, J. C., Voight, B., Suwa, H., and Sumaryono, A. (2000). Lahars at Merapi volcano, Central Java : an overview. *Journal of Volcanology and Geothermal Research*, **100**, 423–456. [1](#)
- Legrand, D., Kaneshima, S., and Kawakatsu, H. (2000). Moment tensor analysis of near-field broadband waveforms observed at Aso Volcano, Japan. *Journal of Volcanology and Geothermal Research*, **101**, 155–169. [7](#)
- Lejeune, A.-M. and Richet, P. (1995). Rheology of crystal-bearing silicate melts: An experimental study at high viscosities. *Journal of Geophysical Research*, **100**(B3), 4215. [4.2](#)
- Lejeune, A.-M., Bottinga, Y., Trull, T., and Richet, P. (1999). Rheology of bubble-bearing magmas. *Earth and Planetary Science Letters*, **166**(1-2), 71–84. [4.2](#)
- Liebske, C., Behrens, H., Holtz, F., and Lange, R. A. (2003). The influence of pressure and composition on the viscosity of andesitic melts. *Geochimica et cosmochimica acta*, **67**(3), 473–485. [4.2](#), [4.5](#)
- Llewellyn, E. and Manga, M. (2005). Bubble suspension rheology and implications for conduit flow. *Journal of Volcanology and Geothermal Research*, **143**(1-3), 205–217. [1](#), [4.2](#)
- Lokmer, I., Bean, C. J., Saccorotti, G., and Patanè, D. (2007). Moment-tensor inversion of LP events recorded on Etna in 2004 using constraints obtained from wave simulation tests. *Geophysical Research Letters*, **34**(22), 1–6. [6.2](#)
- Lokmer, I., O'Brien, G. S., Stich, D., and Bean, C. J. (2009). Time reversal imaging of synthetic volcanic tremor sources. *Geophysical Research Letters*, **36**(12), L12308. [4.8.8](#), [6.4.2](#), [6.4.3](#), [6.5](#), [7](#)
- Mader, H. M. (1998). Conduit flow and fragmentation. *Geological Society, London, Special Publications*, **145**(1), 51–71. [1.2](#)
- Mader, H. M., Manga, M., and Koyaguchi, T. (2004). The role of laboratory experiments in volcanology. *Journal of Volcanology and Geothermal Research*, **129**, 1–5. [2.2](#)

- Mai, P., Burjanek, J., Delouis, B., Festa, G., Francois-Holden, C., Monelli, D., Uchide, T., and Zahradnik, J. (2007). Earthquake Source Inversion Blindtest: Initial Results and Further Developments. *AGU Fall Meeting San Francisco*. 5.2, 5.3, 5.6
- Manga, M., Castro, J., Cashman, K. V., and Loewenberg, M. (1998). Rheology of bubble-bearing magmas. *Journal of Volcanology and Geothermal Research*, 87(1-4), 15–28. 4.2
- Marti, J., Soriano, C., and Dingwell, D. B. (1999). Tube pumices as strain markers of the ductile-brittle transition during magma fragmentation. *Nature*, 402, 650–653. 2.5.2
- Matoza, R., Garcés, M., Chouet, B., D’Auria, L., Hedlin, M., De GrootHedlin, C., and Waite, G. (2009). The source of infrasound associated with longperiod events at Mount St. Helens. *Journal of Geophysical Research*, 114(B4). 1
- McMechan, G. A. (1982). Determination of source parameters by wavefield extrapolation. *Geophys. J. R. Astr. Soc.*, 71, 613–628. 5.2
- McMechan, G. A., Luetgert, J. H., and Mooney, W. D. (1985). Imaging of earthquake sources in Long Valley Caldera, California, 1983. *Bull. Seismol. Soc. Am.*, 75(4), 1005–1020. 5.2
- McNutt, S. (2005). Volcanic seismology. *Annu. Rev. Earth Planet. Sci.*, 32, 461–91. 6.2
- McNutt, S., Rymer, H., and Stix, J. (2000). *Synthesis of volcano monitoring in Encyclopedia of Volcanoes*. Academic Press, San Diego. 1
- Megies, T., Beyreuther, M., Barsch, R., Krischer, L., and Wassermann, J. (2011). ObsPy What can it do for data centers and observatories? *Annals of Geophysics*, 54(1), 47–58. 6.3
- Meier, K., Garaebiti, E., Gerst, A., Harrison, M., Hort, M. K., Kremers, S., Wassermann, J. M., and Weiss, B. (2009). Preliminary insights into an integrated geophysical approach for a better understanding of Strombolian activity at Yasur volcano, Vanuatu. *AGU Fall Meeting*. 1.1, 3.7.1, 6.3, 6.3, 6.4.1, 7
- Meier, K., Hort, M., Tessmer, E., and Wassermann, J. (2012). Infrasound Wave Propagation in the Presence of Small Volcanic Clouds. *submitted to Journal of Geophysical Research*. 6.4.1, 7
- Melnik, O. (2000). Dynamics of two-phase conduit flow of high-viscosity gas-saturated magma: large variations of sustained explosive eruption intensity. *Bulletin of Volcanology*, 62(3), 153–170. 2.2

- Melnik, O., Barmin, A. A., and Sparks, R. S. J. (2005). Dynamics of magma flow inside volcanic conduits with bubble overpressure buildup and gas loss through permeable magma. *Journal of Volcanology and Geothermal Research*, **143**, 53–68. [2.1](#)
- Metrich, N., Bertagnini, A., and Di Muro, A. (2009). Conditions of Magma Storage, Degassing and Ascent at Stromboli: New Insights into the Volcano Plumbing System with Inferences on the Eruptive Dynamics. *Journal of Petrology*, **51**(3), 603–626. [4.2](#)
- Métrich, N., Allard, P., Aiuppa, A., Bani, P., Bertagnini, A., Shinohara, H., Parello, F., Muro, A. D. I., Garaebiti, E., Belhadj, O., and Massare, D. (2011). Magma and Volatile Supply to Post-collapse Volcanism and Block Resurgence in Siwi Caldera (Tanna Island, Vanuatu Arc). *Petrology*, **52**(6), 1077 – 1105. [1.1](#), [6.2](#), [6.3](#)
- Mourtada-Bonnefoi, C. and Mader, H. M. (2004). Experimental observations of the effect of crystals and pre-existing bubbles on the dynamics and fragmentation of vesiculating flows. *Journal of Volcanology and Geothermal Research*, **129**(1-3), 83–97. [1](#), [1.2](#), [2.2](#), [3.2](#), [3.6.1](#)
- Mueller, S. (2007). *Permeability and porosity as constraints on the explosive eruption of magma: Laboratory experiments and field observations*. Dissertation, LMU Muenchen, Muenchen, Germany. [3.1](#), [3.4.2](#)
- Mueller, S., Melnik, O., Spieler, O., Scheu, B., and Dingwell, D. (2005). Permeability and degassing of dome lavas undergoing rapid decompression: An experimental determination. *Bull Volcanol*, **67**, 526–538. [1](#)
- Mueller, S., Scheu, B., Spieler, O., and Dingwell, D. B. (2008). Permeability control on magma fragmentation. *Geology*, **36**, 399–402. [1](#), [2.4](#), [3.2](#), [3.5.1](#), [3.2](#), [3.5.1](#)
- Mykkeltveit, S., Astebol, K., Doornbos, D. J., and Husebye, E. S. (1983). SEISMIC ARRAY CONFIGURATION OPTIMIZATION. *Bulletin of the Seismological Society of America*, **73**(1), 173–186. [6.3](#)
- Mysen, B. O., Virgo, D., and Seifert, F. A. (1984). Redox equilibria of iron in alkaline earth silicate melts; relationships between melt structure, oxygen fugacity, temperature and properties of iron-bearing silicate liquids. *American Mineralogist*, **69**, 834–847. [4.2](#)
- Nairn, I. A., Scott, B. J., and Giggenbach, W. F. (1988). Yasur volcanic investigations, Vanuatu. *New Zealand Geol. Survey*, Seiten 1 – 74. [6.3](#)
- Namiki, A. and Manga, M. (2005). Response of a bubble bearing viscoelastic fluid to rapid decompression: Implications for explosive volcanic eruptions. *Earth and Planetary Science Letters*, **236**, 269–284. [1](#), [2.6](#), [3.2](#), [3.6.1](#)

- Namiki, A. and Manga, M. (2006). Influence of decompression rate on the expansion velocity and expansion style of bubbly fluids. *Journal of Geophysical Research*, **111**(B11). 1, 3.2, 3.7.1
- Neuberg, J., Lockett, R., Ripepe, M., and Braun, T. (1994). Highlights from a seismic broadband array on Stromboli. *Geophys. Res. Letters.*, **21**(9), 749–752. 1, 6.2
- Neuberg, J., Lockett, R., Baptie, B., and Olsen, K. (2000). Models of tremor and low-frequency earthquake swarms on Montserrat. *Journal of Volcanology and Geothermal Research*, **101**, 83–104. 6.2
- Neuberg, J. W., Tuffen, H., Collier, L., Green, D., Powell, T., and Dingwell, D. (2006). The trigger mechanism of low-frequency earthquakes on Montserrat. *Journal of Volcanology and Geothermal Research*, **153**(1-2), 37–50. 6.2
- Nicolas, R. (2009). JMicroVision: Image Analysis Toolbox for Measuring and Quantifying Components of High-Definition Images. 4.8.2
- O’Brien, G. S. and Bean, C. J. (2008). Seismicity on volcanoes generated by gas slug ascent. *Geophysical Research Letters*, **35**(16), 1–5. 1, 6.2, 6.4.2, 6.4.3
- O’Brien, G. S., Lokmer, I., Barros, L. D., Bean, C. J., Saccorotti, G., Metaxian, J., and Patane, D. (2010). Time reverse location of seismic long-period events recorded on Mt Etna. *Geophysical Journal International*. 4.8.8, 6.4.2, 7
- O’Brien, G. S., Lokmer, I., De Barros, L., Bean, C. J., Saccorotti, G., Metaxian, J.-P., and Patane, D. (2011). Time reverse location of seismic long-period events recorded on Mt Etna. *Geophysical Journal International*, **184**(1), 452–462. 1, 5.2, 6.2, 6.4.2
- Ohminato, T., Chouet, B., Dawson, P., and Kedar, S. (1998). Waveform inversion of very long period impulsive signals associated with magmatic injection beneath Kilauea Volcano Hawaii. *Journal of Geophysical Research*, **103**(B10), 23.839–23.862. 6.4.3, 6.4.3
- Oppenheimer, C., Bani, P., Calkins, J., Burton, M., and Sawyer, G. (2006). Rapid FTIR sensing of volcanic gases released by Strombolian explosions at Yasur volcano, Vanuatu. *Applied Physics B*, **85**(2-3), 453–460. 1.1, 3.7.1, 4.2, 4.3, 6.2, 6.5
- Papale, P. (1999). Strain-induced magma fragmentation in explosive eruptions. *Nature*, **397**, 425–428. 3.2
- Parsiegla, N. and Wegler, U. (2008). Modelling of seismic energy transport at volcanoes with real topography and complex propagation medium. *Journal of Volcanology and Geothermal Research*, **171**, 229–236. 6.3

- Parvulescu, A. and Clay, C. S. (1965). Reproducibility of signal transmissions in the ocean. *Radio Electron. Eng.*, **29**(4), 223–228. 5.2
- Pelties, C., Käser, M., Hermann, V., and Castro, C. E. (2010). Regular versus irregular meshing for complicated models and their effect on synthetic seismograms. *Geophys. J. Int.*, **183**(2), 1031–1051. 6.3
- Perrier, L., Métaixian, J.-P., Battaglia, J., and Garaebiti, E. (2011). Estimation of the near-surface velocity structure of the Yasur-Yenkahe volcanic complex, Vanuatu. *Journal of Volcanology and Geothermal Research*. 1.1, 6.2, 6.3, 6.3, 6.3, 6.2
- Phillips, J. C., Lane, S. J., Lejeune, A.-M., and Hilton, M. (1995). Gum rosin-acetone system as an analogue to the degassing behaviour of hydrated magmas. *Bulletin of Volcanology*, **57**, 263–268. 1.2, 2.2
- Piatanesi, A., Cirella, A., Spudich, P., and Cocco, M. (2007). A global search inversion for earthquake kinematic rupture history: Application to the 2000 western Tottori, Japan earthquake. *Journal of Geophysical Research*, **112**(B7), B07314. 5.6
- Pichon, A. L., Antier, K., and Drob, D. (2006). Multi-year Validation of the NRL-G2S Wind Fields using Infrasound from Yasur. *InfraMatics*, **16**, 1–10. 1.1
- Ramesh, K. T. (2008). *Springer Handbook of Experimental Solid Mechanics*. Springer. 3.5.1
- Rietbrock, A. and Scherbaum, F. (1994). Acoustic imaging of earthquake sources from the Chalfant Valley, 1986, aftershock series. *Geophysical Journal International*, **119**(1), 260–268. 5.2
- Ripepe, M. (1996). Evidence for gas influence on volcanic seismic signals recorded at Stromboli. *jvgr*, **70**, 221–233. 6.2
- Ripepe, M. and Gordeev, E. (1999). Gas bubble dynamics model for shallow volcanic tremor at Stromboli. *Journal of Geophysical Research*, **104**(B5), 10.639 – 10.654. 1, 6.2
- Ripepe, M., Poggi, P., Braun, T., and Gordeev, E. (1996). Infrasonic waves and volcanic tremor at Stromboli. *Geophysical Research Letters*, **23**(2), 181–184. 1
- Ripperger, J., Igel, H., and Wasserman, J. (2003). Seismic wave simulation in the presence of real volcano topography. *Journal of Volcanology and Geothermal Research*, **128**, 31–44. 6.3
- Robertsson, J. O. A. (1996). A numerical free-surface condition for elastic/viscoelastic finite-difference modeling in the presence of topography. *Geophysics*, **96**(4B), S11–S27. 6.3

- Robin, C., Eissen, J.-P., and Monzier, M.** (1994). Ignimbrites of basaltic andesite and andesite compositions from Tanna, New Hebrides Arc. *Bulletin of Volcanology*, **56**, 10–22. [1.1](#), [4.3](#), [6.2](#), [6.3](#)
- Sahagian, D. and Proussevitch, A. A.** (1998). 3D particle size distributions from 2D observations: stereology for natural applications. *Journal of Volcanology and Geothermal Research*, **84**(3-4), 173–196. [4.3](#), [4.7](#), [4.8.2](#)
- Sato, H.** (2005). Viscosity measurement of subliquidus magmas: 1707 basalt of Fuji volcano. *Journal of Mineralogical and Petrological Sciences*, **100**(4), 133–142. [4.2](#)
- Scharff, L., Hort, M., Varley, N. R., and Herzog, M.** (2011). Installation of a Permanent Doppler Radar Monitoring System at Colima Volcano, Mexico, and its use for Eruption Cloud Modelling. *AGU Fall Meeting*, Seiten V33A–2611. [3.7.1](#), [7](#)
- Scheu, B.** (2005). *Understanding silicic volcanism: Constraints from elasticity and failure of vesicular magma*. Dissertation, LMU Muenchen, Muenchen, Germany. [2.9](#), [2.6](#), [2.6](#), [3.5.2](#), [3.5.2](#)
- Scheu, B., Spieler, O., and Dingwell, D. B.** (2006). Dynamics of explosive volcanism at Unzen volcano: an experimental contribution. *Bull Volcanol*, **69**, 175–187. [1](#), [2.2](#), [2.4](#), [2.6](#), [3.5.2](#), [3.7](#)
- Scheu, B., Kueppers, U., Mueller, S., Spieler, O., and Dingwell, D. B.** (2008). Experimental volcanology on eruptive products of Unzen volcano. *Journal of Volcanology and Geothermal Research*, **175**(1-2), 110–119. [1](#), [1.2](#), [2.2](#), [2.6](#), [2.6](#), [3.2](#), [7](#)
- Schipper, C. I., White, J. D., and Houghton, B. F.** (2011). Textural, geochemical, and volatile evidence for a Strombolian-like eruption sequence at L’ihi Seamount, Hawai’i. *Journal of Volcanology and Geothermal Research*, **207**(1-2), 16–32. [1](#), [4.2](#)
- Schwarzkopf, L. M., Schmincke, H.-U., and Cronin, S. J.** (2005). A conceptual model for block-and-ash flow basal avalanche transport and deposition based on deposit architecture of 1998 and 1994 Merapi flows. *Journal of Volcanology and Geothermal Research*, **139**, 117–134. [1](#)
- Semmane, F.** (2005). The 2000 Tottori earthquake: A shallow earthquake with no surface rupture and slip properties controlled by depth. *Journal of Geophysical Research*, **110**(B3), B03306. [5.3](#), [5.6](#), [5.11](#), [5.6](#), [5.12](#), [5.13](#)
- Seyfried, R.** (1997). *Magmatische Fragmentierung und vulkanische Fontänen: Theoretische Analyse und experimentelle Simulation der strömungsmechanischen Prozesse*. Dissertation, GEOMAR Forschungszentrum, Christian-Albrechts-Universität zu Kiel, Kiel. [5.8](#), [6.2](#)

- Seyfried, R. and Freundt, A.** (2000). Analog experiments on conduit flow, eruption behavior, and tremor of basaltic volcanic eruptions. *J. Geophys. Res.*, **105**, 23727–23740. [6.2](#)
- Siegel, S.** (2010). Influence of temperature on the fragmentation efficiency of magma: Case study of Lipari pumice. [3.1](#), [3.4.1](#)
- Sigurdsson, H.** (2000). *Introduction In: Encyclopedia of Volcanoes*. Academic Press, London. [1](#)
- Simkin, T., Siebert, L., McClelland, L., Bridge, D., Newhall, C., and Latter, J.** (1981). *Volcanoes of the World: a regional directory, gazetteer, and chronology of volcanism during the last 10,000 years*. Hutchinson Ross Pub Co, Stroudsburg, PA. [1.1](#), [3.7.1](#), [4.2](#), [6.2](#)
- Sparks, R. S. J. and Young, S. R.** (2002). Setting, chronology and consequences of the eruption of Soufrière Hills Volcano, Montserrat (1995-1999): overview over scientific results. *DRUITT, T.H. and KOKELAAR, B.P.(eds) 2002. The eruption of Soufrière Hills Volcano, Montserrat, from 1995 to 1999. Geological Society, London, Memoirs*, **21**, 45–69. [1](#)
- Spieler, O.** (2001). *Die Fragmentierung hochviskoser Magmen. Experimenteller Aufbau und Analysetechniken*. Dissertation, LMU Muenchen, Muenchen, Germany. [2.2](#)
- Spieler, O.** (2004). Magma fragmentation speed: an experimental determination. *Journal of Volcanology and Geothermal Research*, **129**(1-3), 109–123. [1.2](#)
- Spieler, O., Alidibirov, M., and Dingwell, D.** (2003). Grain-size characteristics of experimental pyroclasts of 1980 Mount St. Helens cryptodome dacite: effects of pressure drop and temperature. *Bull - Volcanol*, **65**, 90–104. [1](#), [2.2](#), [3.2](#)
- Spieler, O., Kennedy, B., Kueppers, U., Dingwell, D., Scheu, B., and Taddeucci, J.** (2004). The fragmentation threshold of pyroclastic rocks. *Earth and Planetary Science Letters*, **226**, 139–148. [1](#), [2.2](#), [2.4](#), [2.4](#), [2.11](#), [2.6](#), [2.7](#), [3.2](#), [3.3.1](#), [3.5.2](#), [7](#)
- Steiner, B., Saenger, E. H., and Schmalholz, S. M.** (2008). Time-reverse modeling of microtremors: Application to hydrocarbon reservoir localization. *Geophys. Res. Lett.*, **35**, L03307. [5.2](#), [6.4.2](#)
- Sun, N.-Z.** (1994). Inverse problems in ground water modelling. *Kluwer Academic Publishers*. [5.2](#)
- Sutin, A. M., TenCate, J. A., and Johnson, P. A.** (2004). Single-channel time reversal in elastic solids. *The Journal of the Acoustical Society of America*, **116**(5), 2779. [5.2](#), [6.4.2](#)

- Taddeucci, J., Spieler, O., Kennedy, B., Pompilio, M., Dingwell, D., and Scarlato, P.** (2004). Experimental and analytical modeling of basaltic ash explosions at Mount Etna, Italy, 2001. *Journal of Geophysical Research - Solid Earth*, **109**, B08203 AGU 24 2004. [1.2](#), [2.2](#)
- Taddeucci, J., Spieler, O., Ichihara, M., Dingwell, D., and Scarlato, P.** (2006). Flow and fracturing of viscoelastic media under diffusion-driven bubble growth: An analogue experiment for eruptive volcanic conduits. *Earth and Planetary Science Letters*, **243**(3-4), 771–785. [4.2](#)
- Talagrand, O. and Courtier, P.** (2007). Variational Assimilation of Meteorological Observations With the Adjoint Vorticity Equation. I: Theory. *Quarterly Journal of the Royal Meteorological Society*, **113**(478), 1311–1328. [5.2](#)
- Tarantola, A.** (1988). Theoretical background for the inversion of seismic waveforms including elasticity and attenuation. *Pure and Applied Geophysics PAGEOPH*, **128**(1-2), 365–399. [5.2](#)
- Tarantola, A.** (2005). *Inverse Problem Theory and Methods for Model Parameter Estimation*. Society for Industrial and Applied Mathematics, Philadelphia. [6.4.3](#), [6.19](#)
- Tinti, S., Maramai, A., Armigliato, A., Graziani, L., Manucci, A., Pagnoni, G., and Zaniboni, F.** (2006). Observations of physical effects from tsunamis of December 30, 2002 at Stromboli volcano, southern Italy. *Bulletin of Volcanology*, **68**, 450–461. [1](#)
- Toramaru, A.** (2006). BND (bubble number density) decompression rate meter for explosive volcanic eruptions. *Journal of Volcanology and Geothermal Research*, **154**(3-4), 303–316. [3.2](#), [3.7.1](#), [3.7.1](#), [3.8](#), [7](#)
- Tromp, J., Tape, C., and Liu, Q.** (2004). Seismic tomography, adjoint methods, time reversal and banana-doughnut kernels. *Geophysical Journal International*, **160**(1), 195–216. [5.2](#), [5.2](#)
- van Driel, M., Wassermann, J., Pelties, C., Schiemenz, A., and Igel, H.** (2012). Tilt Effects on Moment Tensor Inversion in the Nearfield of Active Volcanoes. *in prep*. [6.2](#), [6.4.3](#), [7](#)
- Varley, N., Arámbula-Mendoza, R., Reyes-Dávila, G., Sanderson, R., and Stevenson, J.** (2010). Generation of Vulcanian activity and long-period seismicity at Volcán de Colima, Mexico. *Journal of Volcanology and Geothermal Research*, **198**(1-2), 45–56. [3.7.1](#)
- Vergnolle, S.** (1996). Strombolian explosions 1 . A large bubble breaking at the surface of a lava are only slightly damped explosions. *Journal of Geophysical Research*, **101**. [4.2](#), [5.8](#), [6.2](#)

- Vergnolle, S. and Jaupart, C. (1990). Strombolian explosions 1. A large bubble breaking at the surface of a lava column as a source of sound. *J. Geophys. Res.*, **95**, 2793–2809. [1](#), [5.8](#), [6.2](#)
- Vergnolle, S., Boichu, M., and Caplan-Auerbach, J. (2004). Acoustic measurements of the 1999 basaltic eruption of Shishaldin volcano, Alaska 1. Origin of strombolian activity. *javgr*, **137**, 109–134. [6.2](#)
- Vidal, V., Géminard, J.-C., Divoux, T., and Melo, F. (2006). Acoustic signal associated with the bursting of a soap film which initially closes an overpressurized cavity. *The European Physical Journal B*, **54**(3), 321–339. [3.7.1](#), [6.4.1](#), [6.4.1](#), [6.5](#), [7](#)
- Voight, B. (1990). The 1985 Nevado del Ruiz volcano catastrophe: anatomy and retrospection. *Journal of Volcanology and Geothermal Research*, **44**, 349–386. [1](#)
- Walker, G. P. L. (1973). Explosive volcanic eruptions a new classification scheme. *Geologische Rundschau*, **62**(2), 431–446. [3.9.2](#)
- Wassermann, J. (1997). Locating the Sources of Volcanic Explosions and Volcanic Tremor at Stromboli Volcano (Italy) Using Beam-Forming on Diffraction Hyperboloids. *Physics of the Earth and Planetary Interiors*, **10**, 271–281. [1](#), [4.2](#), [6.2](#)
- Westrich, H. R., Stockman, H. W., and Eichelberger, J. C. (1988). Degassing of Rhyolitic Magma During Ascent and Emplacement. *Journal of Geophysical Research*, **93**(B6), 6503–6511. [4.5](#)
- Zobin, V., Luhr, J., Taran, Y., Bretón, M., Cortés, A., De La Cruz-Reyna, S., Domnguez, T., Galindo, I., Gavilanes, J., Muñz, J., Navarro, C., Ramirez, J., Reyes, G., Ursúa, M., Velasco, J., Alatorre, E., and Santiago, H. (2002). Overview of the 19972000 activity of Volcán de Colima, México. *Journal of Volcanology and Geothermal Research*, **117**(1-2), 1–19. [3.7.1](#)



## Acknowledgements

I would like to thank Prof. Heiner Igel and Prof. Donald B. Dingwell for giving me the opportunity to do a doctorate at the LMU Munich. Special thanks for "keeping me alive" in long times of unclear funding. Thanks to Prof. Heiner Igel for the opportunity to spend several months at the Los Alamos National Laboratories and for letting me win from time to time in countless pool billiard games. Invaluable thanks go to Bettina Scheu for the long discussions, the scientific guidance, her interest in details of the work and the uncounted coffees. Great thanks go to Joachim Wassermann for an unforgettable fieldtrip to Vanuatu and the extremely interesting and challenging project arising therefrom. I would like to thank my longtime colleagues Julia Linder, Tobias Megies, Christian Pelties, Moritz Beyreuther and Annika Ferk all for very different reasons but mainly for being good friends and very supportive in the last years. Thanks you for the million coffee breaks that were used to discuss strictly scientific topics. I want to thank my longtime roommate Michael Winklhofer for uncounted Monday morning discussions on the things that are really important in life: Football and Formula 1. I would like to thank Uli Kueppers for last minute proof-reading and being the fun person he is. Thanks go to all my co-authors and the people that helped me preparing what is presented herein. I want to thank my parents and sisters for their love and support throughout the whole time at the university. Thanks go to Conny for backing me up in good and bad times. Thanks go to the team of the observatory in Frstenfeldbruck, namely Sven, Werner and Martin. It appreciated working with you. I would like to thank the technical staff at LMU for their daily support, especially Jens Oeser. Without the new monitor i would have never made it...

Thanks are also expressed to all the people who feel forgotten in these very last-minute acknowledgements.